PLASTICS WELDING MANUAL

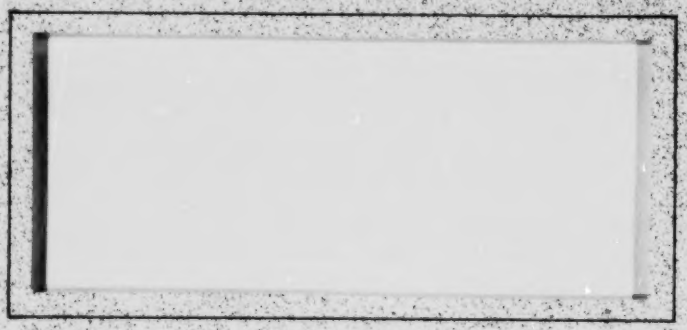

Welding Institute of Canada
Institut de Soudage du Canada

WELDING INSTITUTE OF CANADA
INSTITUT DE SOUDAGE DU CANADA

WELD OVERLAY DISBONDING

Welding Institute of Canada Report RC262/4/88

~~Confidential~~ to

Department of Energy, Mines and Resources,
and Supply and Services Canada
Reference 15SQ.23440-5-9057
OSQ 85-00093

Approved by:

Dr. K.G. Leewis
Director of Technology

MICROMEDIA

Prepared by: R.B. Lazor
K.G. Leewis

August, 1988

ive pp

HEAD OFFICE / SIEGE SOCIAL: 391 Burnhamthorpe Road East, Oakville, Ont. L6J 6C9 - Ph: (416) 845-9881
CENTRE DU QUEBEC / QUEBEC CENTRE: 2399 rue de la Province, Longueuil, Que. J4G 1G3 - Ph: (514) 651-5086

TABLE OF CONTENTS

		Page
	List of Tables	(ii)
	List of Figures	(iv)
1.	Introduction	1
	1.1 Approaches to Reduce Disbonding	3
	1.1.1 Welding Process Selection	3
	1.1.2 Welding Conditions	3
	1.1.3 Post Weld Heat Treatment	4
	1.1.4 Residual Stress	5
	1.1.5 Hydrogen Concentration	6
	1.1.6 Fracture Toughness	7
	1.2 Summary of Techniques to Reduce Disbonding	7
2.	Experimental Procedures	8
	2.1 Materials	8
	2.2 Welding Procedures	9
	2.3 Post Weld Heat Treatment	11
	2.4 Preparation of Disbonding Coupons	11
	2.5 Autoclave Tests	12
	2.6 Ultrasonic Examination	13
3.	Results	13
	3.1 Side Bend Tests	13
	3.2 Metallographic Examination	14
	3.2.1 Dilution Measurements	14
	3.2.2 Chemical Analysis of Overlay	14
	3.2.3 Ferrite Measurements	15
	3.2.4 Hardness Measurements	15
	3.2.5 Microstructural Observations	17
	3.3 Metallographic Examination after Autoclave Tests	18
	3.4 CANMET Samples	19
4.	Discussion of Results	19
	4.1 Side Bend Tests	19
	4.2 Dilution	20
	4.3 Ferrite Measurements	21
	4.4 Microstructural Analysis	21
	4.5 Autoclave Tests	22
	4.6 Ultrasonic Inspection of Autoclave Samples	22
5.	Conclusions	23
6.	Recommendations	24
7.	References	25
8.	Appendix A - Autoclave Test Procedures	
	B - Summary of Manual U/T Results	
	C - Summary of Automated U/T Results	

LIST OF TABLES

		Page
1.	Hydrogen Modelling Matrix (18)	28
2.	Critical Stress Intensity Factor of Hydrogenated Reactor Wall Materials	29
3.	Chemical Compositions of Baseplate and Strip Electrode	30
4.	Welding Conditions	30
5.	Dilution Measurements of Overlay Samples	31
6.	Penetration and Overlay Reinforcement Measurements	31
7.	Chemical Analysis of Overlay Deposits	32
8.	Weld Overlay Ferrite Numbers	33
9.	Microhardness Traverses (50 g) Across Fusion Line	33
10.	Summary of Quantitative Analysis of Type II Fusion Boundary Grains	34
11.	Autoclave Disbonding Summary	35

LIST OF ILLUSTRATIONS

		Page
1.	Schematic representation of microstructures for various growth modes.	38
2.	Disbonding results related to welding current, travel speed and microstructure	40
3.	Effect of PWHT condition on hydrogen induced disbonding.	41
4.	Change of the distance of carbon migration and ductility of weld bond as a function of time and temperature.	42
5.	Effect of interlayer overlay weld on hydrogen induced disbonding.	43
6.	Changes of chemical compositions in the transition zone and chemical compositions of each sample.	43
7.	Variation in surface strain due to slicing. Location of strain gauge, centre of bead. As welded condition.	44
8.	Distribution of the residual stresses in through-thickness direction across the overlay welds.	44
9.	Hydrogen induced disbonding test results.	45
10.	Hydrogen distribution across the fusion line for a 10 micron wide interface.	45
11.	Peak hydrogen concentration profile for typical autoclave test cooled at -28°C/h.	46
12.	Effects of cooling rate, base metal and overlay thickness on hydrogen concentration.	47
13.	Effect of shutdown pressure on hydrogen concentration.	47
14.	Effects of shutdown temperature on hydrogen concentration.	48
15.	Correlation of peak hydrogen concentration obtained from computer model and % disbonding from autoclave tests.	48
16.	Grounding arrangements observed during welding: a) ground attached to either end of plate; b) welding away from the ground (c) ground attached to positioner table; (d) welding towards ground.	49
17.	Summary of weld overlay deposition with respect to the principal rolling direction of the 2.26 Cr - 1 Mo baseplate.	50
18.	a) General view of autoclave specimen, b) Autoclave coupon before being surfaced along the sides with 316 SMAW electrodes	50
19.	Pseudo-C-scan plot of disbonded areas from mechanized ultrasonic scanning of sample D2A5	51
20.	Example of cracking in sample B1A1 after 180 degree bend test.	51

LIST OF ILLUSTRATIONS (Cont'd)

Page

21. a) Above, section through the centre of bend sample B1B4 showing that the crack coincided with the corner where adjacent beads overlapped; (b) below, part-through cracks near the support points of B1B4 initiated near the fusion boundary and ran preferentially into the overlay. 52

22. Detail near the crack tip of Figure 21a showing that the cracks run parallel to the fusion line within the HAZ of the Cr-Mo baseplate. 53

23. Cross-section through a strip clad specimen showing the relative contributions of electrode (F) and baseplate (Fo) to the deposit chemistry. 53

24. Sections through the overlay deposits show the 750 A overlay to be more uniform in terms of penetration than the 1500 A overlay. 54

25. Example of 50 g microhardness traverse across the fusion boundary of sample E1A, Micro L3. 55

26. Microhardness profile across the carbide layer using a 50 g load. 56

27. Hardness traverses across the fusion boundary of specimens A1.2A (750 A) and A2.2A (1500 A) using a 50 g diamond pyramid indenter. 57

28. Fusion line between the overlay and baseplate showing tempered martensite in the narrow austenite zone and carbide precipitation in the HAZ. 58

29. Fusion boundary area of overlay A1.1 showing Type II boundaries tempered martensite, carbide precipitation in the HAZ, and prior austenite grain boundaries in HAZ extending into the overlay. 58

30. Microstructure of 750 A overlay deposit E1. 59

31. Microstructure of 1500 A overlay deposit D2. 59

32. Overlay sample B1B shows that sigma phase has replaced some of the ferrite within the interdendritic spaces. The sigma phase appears yellow when viewed directly. 60

33. Summary of disbonding results after autoclave exposure. 61

34. Cracks running along the Type II grain boundaries of specimen A1.1 after autoclave testing. 62

35. Cracks in the transition region of specimen A1.1 after autoclave testing. 62

LIST OF ILLUSTRATIONS (Cont'd)

		Page
36.	Cracks in the carbon-rich layers of specimen A1.1 after autoclave testing.	63
37.	Examples of cracking associated with 180° bend tests of clad samples from (18).	63
38.	Ferrite number versus dilution (calculated from Ni content) for all overlays.	64
39.	Disbonding percentage versus cooling rate for autoclave specimens.	65
40.	Manual ultrasonic versus automated ultrasonic C-scan inspection results from autoclave test specimens.	66

WELD OVERLAY DISBONDING

DSS File No. 15SQ.23440-5-9057

Welding Institute of Canada Report RC262/3/88

1.0 Introduction

Reactor vessels used for high temperature hydro-treatment of heavy oils or tar sands (bitumen) typically operate at 400 to 450°C and pressures of 10 to 20 MPa. These pressure vessels are fabricated from low alloy 2 1/4Cr-1Mo steels overlaid on the inner surface with stainless steel. The formation of stable carbides and intermetallic compounds in the low alloy steel improve both the resistance to creep damage and hydrogen attack by decarburization. The stainless clad layer resists corrosion due to H_2S in the process stream.

After steady-state conditions have been attained in the hydrogenation process, there is an equilibrium distribution of hydrogen in the vessel wall, with the Cr-Mo steel typically absorbing about 5 ppm hydrogen (1). These vessels are frequently shut down due to the nature of the refining operations, for periodic inspection, or due to an emergency situation. As the vessel cools, the differences between the diffusion coefficients of the ferrite (Cr-Mo steel) and austenite (stainless steel overlay) produces a build-up of hydrogen along the fusion line. At the same time, the different thermal expansions of the overlay and the Cr-Mo steel produce thermally-induced strains along the fusion boundary. The combination of a high hydrogen content and high strains along the interface have been attributed to disbonding between the overlay and the low alloy steel. Experience has shown that disbonding is more prevalent at the faster cooling rates. While such vessels are usually brought off-line under controlled schedules to allow hydrogen permeation out of the shell, emergency shutdowns cannot be avoided and hence, disbonding occurs near the fusion line.

The fact that disbonding occurs along the boundary between the overlay and the baseplate suggests that the microstructure in this area is also a contributing factor. The microstructures in this transition region are influenced by:

a) The chemical compositions of the base metal and the overlay material, and the relative dilution between the two.

b) Differences in the thermal expansion of the 2 1/4 Cr-Mo baseplate and the 309 stainless overlay.

c) Heat treatments following the cladding operation.

The postweld heat treatments (PWHT) specified in the ASME Boiler and Pressure Vessel Code, Section VIII Division 2, are intended to reduce the thermal stresses induced during welding. PWHT has been known to cause carbide precipitation along grain boundaries and within the martensitic layer at the interface, segregation of impurities to grain boundaries in the overlay, and diffusion of carbon from the baseplate into the overlay.

Much of the experience and literature related to the fabrication of clad pressure vessels and to the problem of disbonding, was found overseas. The work addressed in this project was funded by CANMET of Energy, Mines and Resources to develop Canadian fabrication expertise and benefit upgrading and refining operations. The approach developed a collaborative program involving CANMET, fabricators, consumable suppliers, petrochemical plant operators and designers, universities, and research institutes.

The overall objective was to examine weld overlay procedures that minimize the occurrence of hydrogen induced disbonding in reactor vessels. The secondary objective of this program was to examine the variability in overlay deposits between fabricators.

1.1 Approaches to Reduce Disbonding

1.1.1 Welding Process Selection

The arc welding process selection is important in influencing the type of microstructure along the fusion line and thus its susceptibility to disbonding. In comparing four ASME qualified overlay welding procedures, Sims and Bruck (2) reported that Type II boundaries were rarely observed using SMAW. Parallel grains were confined to bead edges with a series arc overlay procedure, and both strip and six wire overlay procedures produced random Type II boundaries which were not necessarily coincident with bead edges. These observations, therefore, suggest an important direct relation between heat input and Type II boundaries.

Similar observations have been reported by Sakai and his co-workers (3) using SMAW, SAW, and ESW procedures. As the cooling rate decreases in order, respectively, for these three processes, the amount of Type II boundaries increases and so does the incidence of disbonding. The authors indicate that Type II boundaries are produced by planar growth from the grains in the CrMo HAZ following the accepted theories on solidification. Savage (4) shows how the solidification structure is influenced by the region of constitutional supercooling (Figure 1), which in turn, is determined by the temperature gradient, growth rate, and solute concentration. Solute impurities such as sulphur and phosphorous can be swept to these grain boundaries, leading to embrittlement.

1.1.2 Welding Conditions

The influence of welding conditions on the resistance to disbonding was studied by Ohnishi and others (5). They found that drastic changes to strip overlay welding conditions were necessary to improve the disbonding test results. This was due to a change from a mixed austenite/ferrite structure to one of austenite/martensite in the overlay (see Figure 2), and a reduction in the degree of the coarse-grained Type II zone near the fusion line.

Specimens which exhibited the lowest disbonding percentages tended to be those which had the higher Ni equivalents, and lower ferrite (6).

High speed (HS) submerged arc overlay welding was examined as a means to reduce disbonding (7). It was found that the HS overlay had a faster cooling rate in the boundary region, resulting in the inhibition of Type II boundaries and replacement with a finer grain structure which would reduce the concentration of impurities at grain boundaries. The base metal HAZ for the HS process also had a finer grain size due to the faster cooling rates compared to conventional SAW and ESW procedures.

The significance of the welding speed, rather than composition, in promoting overlays with fewer Type II boundaries was demonstrated by Fuji and his co-workers (8). They showed that the presence of Type II grains could be reduced for an austenite/40 percent martensite overlay by increasing travel speed, while maintaining the same nominal heat input, composition, and microstructures.

1.1.3 Post Weld Heat Treatment

The influence of PWHT on the disbonding phenomenon is clearly shown in Figure 3, which plots the peak hydrogen concentration against the Larson-Miller parameter (9). The critical hydrogen level to produce disbonding drops linearly as the P value increases. The authors attributed the greater incidence of disbonding to the extent of the carbide precipitate in the overlay and particularly to the precipitation of carbides at grain boundaries and within grains. The width of the band can be predicted using the results of Christoffel and Curran (10). The results for a 2.25Cr-1Mo/Type 347 combination are shown in Figure 4. Cracks appear in the overlay adjacent to the migration zone (11). To prevent this, Hattori and his co-workers applied interlayers of low carbon, low carbon plus niobium, and low carbon plus niobium and vanadium to the baseplate before the stainless overlay and subsequent autoclave tests. The results in Figure 5 indicate that the best properties are obtained by adding strong carbide forming elements. The improved resistance to disbonding was due to a fine dispersion of carbides which functioned as trap sites for hydrogen.

Grain boundary carbide precipitation can also be controlled by using niobium. Chromium-rich carbides are not observed when a stabilized overlay is used (12). It is assumed that the niobium carbides are finely dispersed,

thus hydrogen is trapped uniformly throughout the matrix, rather than at the Type II grain boundaries.

Longer PWHT times and higher temperatures induce higher hardness of the tempered martensite layer in the overlay, immediately adjacent to the fusion line, due to the diffusion of carbon from the baseplate (13).

A typical change in chemical composition across the transition region is shown in Figure 6 (14). The Cr and Ni contents exhibit a compositional gradient with carbon peaking at the interface. This change in the carbon profile with decarburization of the base metal develops during PWHT. Strong carbide formers such as Nb were beneficial in keeping the peak carbon value low.

1.1.4 Residual Stress

The through thickness strain distribution in overlaid plates measured by Kume and others (15) (Figure 7) showed high biaxial tensile strains in the overlay and in the baseplate adjacent to the fusion line, and high compressive strains at the overlay interface. The Poisson effect associated with the tensile strains in the overlay produces a tensile stress across the fusion boundary which contributes to the disbonding phenomenon. These stresses are reduced somewhat during PWHT but are not zero because of the strains which develop during cooling due to the differences in thermal contraction between the austenitic overlay and the ferritic baseplate. Measurements of residual stress normal to the interface, using a hole drilling method, have shown that these stresses are in the order of 137 MPa (16). A quick calculation showed that 0.2% strain was reached by only a 525°K change in temperature for 309 overlay on 1020 plate. Welding could see three times the yield.

Overlay weld metals with a duplex structure of austenite/martensite have been shown to be more resistant to disbonding (5). This improvement is due to a lowering of the residual stress across the interface for the duplex structure (see Figure 8) as a direct consequence of the martensitic transformation in the overlay (17).

1.1.5 Hydrogen Concentration

Disbonding test results for 7 mm thick cladding have shown that disbonding occurs when the hydrogen concentration at the interface exceeds 100 ppm (Figure 9). The hydrogen values had been calculated using a finite difference method assuming a one-dimensional model, similar to the analysis reported by Chakravarti and Malik (18). This value of 220 ppm is representative of a layer at the interface approximately 10 microns wide. Using a similar approach, Hattori and others (9) report that disbonding will occur when the hydrogen concentration level exceeds 150 ppm at a point 50 microns from the interface. Both of these profiles are consistent with Figure 10, but these two are much lower than the 300 ppm peak hydrogen concentration reported by Morishige et al (19), and the 420 ppm peak value obtained by Fujii et al (13).

Disbonding can be prevented if the hydrogen is allowed to diffuse away from the interface before room temperature is attained (19). This requires holding the temperature above 100°C long enough to reduce the peak hydrogen levels below the critical value. Tests are usually conducted in air, but degassing can also be realized with a vacuum. It is not always possible to heat vessels and ensure hydrogen removal, thus other contributing factors to the disbonding phenomenon are important.

In order to provide a link between the autoclave test results and actual pressure vessel operation, AMCA International undertook modelling of the hydrogen distribution using an existing PMRL computer program. The objectives of this exercise were to predict the incidence of disbonding taking into account changes in boundary conditions such as cooling rates, weld overlay and base metal thicknesses, and operating temperatures and pressures (18).

Eighteen combinations of temperature, pressure, cooling rate and thickness were chosen, as listed in Table 1. The first four runs were identical to the autoclave conditions, while the remainder were representative of field conditions. The output of each computer run was summarized as shown in Figure 11. The solid line represents the hydrogen distribution during steady state conditions, while the dotted line indicates the peak hydrogen concentration at the fusion line during cooling.

The effects of cooling rate and the relative thicknesses of base metal and weld metal on the peak hydrogen concentration were summarized in Figure 12. The hydrogen at the interface increased as the cooling rate increased. The base metal thickness had little influence on the hydrogen for the double-sided diffusion model. Increasing the operating hydrogen pressure increased the peak hydrogen concentration (Figure 13). The influence of operating temperature is dependent upon the type of model used (Figure 14). For single-sided entry, the hydrogen concentration decreases with increasing temperature, while the peak value increases with higher temperatures for the double-sided model. The peak hydrogen values for the autoclave tests versus cooling rates for each of the weld procedures is predicted in Figure 15. This figure also predicts the actual percentage of disbonding from the autoclave samples as a function of peak hydrogen concentration.

1.1.6 Fracture Toughness

Once initiated, cracks propagate through the brittle martensite zone because of the lower critical stress intensity factors, (20), Table 2. This reduction in fracture toughness was due mainly to $M_{23}C_6$ carbides which precipitated at the edges of the delta ferrite and along the Type II boundaries (11). These precipitates form extensively as sheets at relatively short exposure times at high temperature. Heat input had little influence on the amount of carbide precipitated (21).

1.2 Summary of Techniques to Reduce Disbonding

The preceding paragraphs highlight the various approaches which have been used to prevent hydrogen-induced disbonding. There is the possibility of changing the welding conditions so as to restrict the thermal cycling of the baseplate. Solid state transformations can be used to reduce the stress at the interface, and alloying can enhance the stability of the carbide precipitates and the resistance to hydrogen embrittlement. Welding parameters which result in rapid cooling rates in the HAZ are preferred to promote dendritic solidification, replacing initial planar Type II growth from the coarse-grained plate HAZ. Controlling the grain growth in the baseplate with titanium and boron promotes rapid transition towards dendritic solidification,

reducing the extent of Type II boundaries. Alloying with niobium reduced disbonding by increasing the stability of the carbides, thus preventing carbon precipitation along Type II boundaries during PWHT. The fine dispersion of carbides was beneficial during cooling since they provide numerous traps for hydrogen. Finally, the transformation to martensite reduces the residual stress and hence the susceptibility to disbonding along the fusion line.

2.0 Experimental Procedures

Weld overlay specimens were prepared by five fabricators with the same baseplate, overlay material, and nominal welding procedures. All coupons were produced with a single layer of 309L stainless steel overlay on Cr-Mo baseplate.

In actual practice, a two layer procedure would be used. A sixth overlay specimen was prepared by CANMET with a low carbon buttering layer between the baseplate and overlay material.

The behaviour of disbonding coupons produced from this plate is discussed separately from the remainder of the results. A full report describing the testing of these coupons was prepared by CANMET (27).

2.1 Materials

A 63 mm thick 2 1/4 Cr - 1 Mo baseplate (SA387, Grade 22, Class 2) supplied in the quenched and tempered condition was overlaid by submerged arc welding using a 60 x 0.5 mm thick E309L stainless steel strip electrode and a neutral non-compensating flux. The chemical compositions of the baseplate and the electrode are listed in Table 3.

The Cr-Mo plate has a J-factor:

$$J = (Si + Mn)\,(P + Sn) \times 10^4 = 105$$

which is well below the recommended maximum of 200 (22), indicating that it has been made to resist temper-embrittlement. The other impurities which

promote temper embrittlement, As and Sb, were below their respective suggested maximums of 0.020 and 0.004 (1).

The surface scale was removed by grit-blasting, and light grinding. Each of the fabricators examined the plates ultrasonically (C-Scan) for delamination. There were no reported problems with the 2 1/4 Cr-1Mo plate.

The first layer 309L, restricts carbon diffusion from the base plate and the second layer of 308 or 347, provides the corrosion resistant surface and also tempers the 309L coating (23). To encourage disbonding in this program, however, only the first layer was deposited, not two layers as would be done with the complete procedure.

2.2 Welding Procedures

The following strip cladding procedures, both at the same nominal heat input of 9 kJ/mm, were employed:

Procedure	Current, amps	Voltage, volts	Travel Speed, mm/min
1	750	27 to 28	140
2	1500	27 to 28	280

Electrical Stick-Out : 35 mm
Polarity : DC, electrode positive
Preheat : 149°C (300°F)
Electrode Angle : 90° to the plane of welding
Overlap : 5 mm

a) The strip to be cut at an angle of 20° to facilitate arc starting.
b) The flux baked for a minimum of two hours at 260°C, and then placed in holding ovens at 45°C.
c) The flux was not to be recycled.

The literature suggested that the overlay produced with the lower current, slower travel speed would be more susceptible to disbonding (20).

There were some variations in the weld overlay specimens prepared by the five fabricating shops. These specimens were identified as A, B, C, D and E as outlined in Table 4. Table 4 summarizes the major welding parameters and

highlights disparities. For procedure 1; the maximum interpass temperature varied from 163°C to 316°C; fabricator E used a much shorter electrical stick-out than the others (25 mm compared to 32-37 mm); and fabricators D and E used a lead angle of 2 degrees. Due to power source limitations, one of the fabricators was not able to prepare a procedure 2 overlay, while two of the remaining four had to reduce the current. Of these two, fabricator C maintained a nominal 9 kJ/mm heat input by reducing the travel speed, while fabricator E did not change the travel speed and thus ended up with a slightly lower nominal heat input of 8.7 kJ/mm.

The number and type of ground connections was not specified and consequently, several configurations were used, but there were two ground connections in each instance. Referring to Figure 16, two fabricators utilized arrangement (a), while (b), (c), and (d) were used by each of the remaining shops.

Preheat and interpass temperatures were monitored using temperature-indicating crayons. The common practice was to check the temperature at several positions on the plate surface, but one of the procedure records noted that the temperature was measured on top of a completed bead.

The overlay deposits were to have been deposited parallel to the principal rolling direction. However, as shown in Figure 17, six overlays were completed perpendicular to, and three were completed parallel to, the rolling direction.

Each of the fabricators subjected the clad plates to a post weld hydrogen removal heat treatment at 607°C for 30 minutes.

The overlay surfaces were examined for surface cracks using liquid penetrant. All were acceptable. Likewise, ultrasonic inspection of the overlay coupons did not reveal any fusion line defects or underbead cracks. Inspection was conducted using a 2.2 MHz, 19 mm diameter probe on the underside of the overlay coupon, using a 3.2 mm diameter, flat-bottomed hole as a reference reflector.

2.3 Postweld Heat Treatment

The overlay coupons were postweld heat treated through CANMET, in accordance with ASME Section III, Division 1 requirements, in a single furnace batch. The stress relief cycle was as follows:

a) room temperature to 300°C, heating rate of 140°C/h;
b) 300°C to 690°C, heating rate of 60°C/h;
c) hold at temperature of 690°C for 24 h;
d) cooling rate of 56°C/h from 690° to 300°C; and
e) cooling rate of 150°C/h below 300°C.

The hold time of 24 hours at 690°C represents the maximum tempering parameter during actual fabrication of heavy-walled pressure vessels of 2 1/4 Cr - 1 Mo steel. The plates were heated uniformly from room temperature in the furnace to reduce the risk of developing transient tensile thermal stresses, and thus, reduce the likelihood of reheat cracking. The peak temperature of 690°C was within the 675 to 760°C range specified for the P-No.5 Cr-Mo baseplate in ASME Section III, Division I. While this temperature relieves the stresses in the baseplate, carbide precipitation along the fusion interface and sigma-phase development was unavoidable in the weld overlay. If left in the as-welded condition, 2 1/4Cr-1Mo steels are likely to experience hydrogen damage at temperatures about 100°C below those given on a Nelson curve (24).

2.4 Preparation of Disbonding Coupons

Disbonding coupons were machined from the overlaid plates. These were centred on the overlap between beads (Figure 18). The Cr-Mo baseplates on the sides of the autoclave coupons were surfaced by SMAW, with an austenite deposit, then turned to a final diameter of 100 mm.

The overlaid plates were ultrasonically examined after stress relief, using 5 MHz, 12.5 mm diameter probes from the underside of the coupons. Three of the plates, C1, C2, and D2, provided reflector indications greater than the 3.2 mm diameter, flat-bottomed reference reflector. The numbers (1 or 2) after the letter designating the fabricator, indicates the welding procedure used on the specific test plate. Plate C1 had a continuous snake-shaped reflector across the first four overlay passes. Plate C2 had thirteen 25 mm diameter reflectors which were randomly located throughout the coupon. Plate

D2 had a single 25 mm diameter reflector towards one side of the plate. Sections through the ultrasonic indications on these plates did not reveal any defects, however, these regions were avoided during subsequent preparation of bend test specimens and autoclave coupons.

2.5 Autoclave Tests

The main objective of the autoclave tests was to develop a procedure which would produce repeatable disbonding. Two laboratories were approached to conduct the autoclave tests allowing a cross-comparison. Both conditions of hydrogen charging, and the cooling rates after exposure, were the key parameters.

After reviewing the literature with the participating laboratories, the following procedure was specified:

1) Attach thermocouples to the surface of specimens.
2) Seal specimens into autoclave and introduce hydrogen gas into chamber at 60 kg/cm^2. When the autoclave reaches the test temperature of 450°C, the gas pressure should be 155 kg/cm^2.
3) Heat the autoclave at a rate of 170°C/h.
4) Hold at 450°C and 155 kg/cm^2 for 48 h.
5) Release hydrogen pressure.
6) Cool specimens to room temperature at the following rates: 28° + 5, 56° + 5, 111° + 8 and 222°C + 10°C/h. Introduce helium or nitrogen into the autoclave to accelerate cooling.

Up to three specimens were put into the autoclave at any one time for hydrogen charging. The conditions during hydrogen charging (155 kg/mm^2, 450°C) are typical of operating conditions of hydro-desulphurizing reactors, and are identical to autoclave test conditions reported by others (3,6,7,14,20, 26).

A final group of autoclave experiments replaced the hydrogen atmosphere with nitrogen. These tests were to determine whether only thermal expansion differences between the overlay and the baseplate would be sufficient to promote disbonding. Test results for the three fastest cooling rates on samples prepared from both high and low heat input procedures showed that hydrogen was necessary to cause disbonding.

2.6 Ultrasonic Examination

Ultrasonic examination of the samples after autoclave exposure was conducted so as to identify a 2 mm diameter indication at the fusion boundary. These tests were performed at least three days after the samples had been removed from the autoclave. Around the edge of all samples there was a 10 mm ring of overlay which did not disbond. Over the central area of the coupons, bonded and disbonded areas were marked and the percentage of disbonding was determined for each sample.

All samples were examined using both B Scan and C Scan ultrasonic procedures. The manual procedures were conducted at WIC primarily to identify which conditions would produce disbonding so that conditions for future tests could be specified. The manual inspections ran concurrently with the autoclave tests.

As a verification of the manual ultrasonic procedure and technique used to detect disbonding, several metallographic sections were prepared to include the expected boundary between sound and disbonded regions. Within the experimental variation of marking the disbonded areas, this examination confirmed the suitability of the ultrasonic procedure.

The samples were sent to CANMET after autoclave testing for mechanized ultrasonic examination for pseudo-C-scan plots in an immersion tank (Figure 19). The boundaries of the disbonded areas were outlined in each plot, measured on a Quantimet, and expressed as a percentage of the total surface area. The automated technique for locating disbonding and the manual results were in good agreement.

3.0 Results

3.1 Side Bend Tests

Two side bend tests were prepared from each overlay in an orientation perpendicular to the welding direction. The centre of the bend tests were located at the overlap between adjacent beads, as per operator qualification, specified by ASME Section IX, QW-311(a). Only procedure B1 bend test

specimens exhibited any cracking (Figure 20). Two additional bend specimens produced similar cracks which ran completely through the sample (Figure 21a) and part-through cracks near the support points (Figure 21b). Figure 21 suggested that the cracks initiated at the bond line and propagated into the overlay. Note that the cracks also ran parallel to the fusion boundary within the heat-affected zone of the baseplate, as shown in Figure 22.

3.2 Metallographic Examination

3.2.1 Dilution Measurements

The dilution can be graphically determined from a cross-section of the deposit as shown in Figure 23. The areas F and F_O, measured from X5 magnification cross-sections of each deposit using a digitizing tablet, are summarized in Table 5. The dilution measurements for the 750 A procedure range from 12 to 24 percent, and averaged 18 percent. For the high current overlay, the dilutions range from 22 to 35 percent, with an average of 28 percent. The dilutions measured for the individual samples are also listed in Table 5.

The penetration profiles for the 750 A overlays were quite uniform with no marked tendency for one segment of the bead to have a deeper penetration. The 1500 A overlays had the deepest penetration at the centre of each bead. The photographs in Figure 24 show the differences in penetration characteristics between the two procedures.

The depth of the overlay penetration and the height of the reinforcement were measured at 15 mm intervals across at least two beads and this data is summarized in Table 6. They show that the 1500 A procedure gave both deeper penetration and greater reinforcement than the 750 A procedure. The largest variations in the average values were observed for the penetration of the 1500 A overlay.

3.2.2 Chemical Analysis of the Overlay

The composition of the overlay deposit was determined by wet analysis as per ASME Section IX, QW 462.5. A minimum qualified thickness of 3.35 mm was

the distance from the original baseplate surface to the lowest point of the overlay surface. A 0.5 mm thick layer was removed between 3.35 and 2.85 mm from the original interface for chemical analysis. The gradient of Cr, Ni, Mo, and Mn contents, from the baseplate to the overlay, usually occurs across the fusion line, and is in the order of 0.1 mm (28) wide. The chemical analysis was representative of the cladding (Table 7). The higher concentrations of Mn, Ni and Cr confirmed that the 750 A overlays had a lower amount of dilution.

3.2.3 Ferrite Measurements

The ferrite content of each overlay was determined magnetically with both a Magne-Gage and a Forster Meter. The Magne-Gage was calibrated utilizing weld metal secondary standards (McKay Standard Set No. 017A) of 3.1, 5.4, 9.4, 12.6, and 17.2, and brass for zero ferrite. Forster Meter readings on the same samples averaged approximately twenty percent less. Overlay samples for ferrite measurement were cut 2.5 mm thick, such that the measuring surface was 3.1 mm from the fusion boundary.

The weld overlay ferrite contents are listed in Table 8. As expected the Forster Meter readings are lower than those for the Magne-Gage. The Magne-Gage ferrite numbers for the 750 A procedure range from 2.7 to 4.4 FN, while the 1500 A procedure resulted in FN values from 5.0 to 8.6.

3.2.4 Hardness Measurements

After PWHT, microhardness traverses were made across the fusion boundary at the centre of the overlay using a Vickers diamond pyramid indenter with a 50 g load. The example in Figure 25 shows that the diagonal length of the indentation was typically 15 microns; Note that the tempered martensite layer (carbide zone) was just over 60 microns wide. As a check to confirm that an indentation located at the centre of the fusion boundary provided a representative hardness, a traverse was conducted at 20 micron intervals across a typical carbide region. A specimen (A2.2A) with a sufficiently large carbide zone, was chosen to facilitate the several hardness indentations necessary to model the variation of hardness across these regions. The results presented in Figure 26 show that the high hardness does in fact occur across the martensite layer, and the hardness decreases gradually at the

boundaries. Furthermore, the hardness closest to the austenitic deposit was higher than that measured adjacent to the Cr-Mo baseplate.

The remainder of the hardness traverse results are summarized in Table 9 and typical variations in hardness across the fusion boundary are illustrated in Figure 27. The layer of tempered martensite at each of the traverse locations was typically between 40 and 60 microns wide. The peak hardness occurred at the single indentation at the centre of this region. The hardness values immediately adjacent to this area were significantly less. Remote from the fusion boundary, the average baseplate hardness was 200 DPH. Approaching the boundary from the baseplate side, there is a slight decrease in hardness, in the order of 20 to 40 DPH, then the hardness peaks in the narrow tempered martensite layer at the fusion line. The hardness in these regions was over 400 DPH, except for weld B1, which measured 346 DPH. On the overlay side, the average hardness away from the fusion line was dependent on the welding procedure. The (750 A) welds resulted in overlay hardnesses which were comparable to those in the baseplate, while the (1500 A) procedure produced higher hardnesses in the overlay.

Two hardness profiles were observed when approaching the fusion line from the overlay side. In one case there is a decrease in hardness within 0.1 mm from the boundary (A1.2A in Figure 27), while in the other, an increase towards the boundary and a softer region immediately adjacent to the carbide layer (A2.2A in Figure 27) is observed. The hardness peak for the latter sample coincides with an intrusion of Cr-Mo into the overlay. This is a darker etching region and appears to be predominantly martensitic.

The change in hardness across the fusion line was an indication of the extent of carbon redistribution during PWHT, and the susceptibility to disbonding (1). It is assumed that carbon which diffuses from the base metal into the austenitic weld metal during PWHT, forms carbides along the grain boundaries, thereby promoting grain boundary embrittlement. This embrittlement, and susceptibility to disbonding, are exacerbated by high PWHT temperatures and/or long cooling times.

3.2.5 Microstructural Observations

The fusion line between the overlay and the baseplate is shown in Figure 28. The austenitic 309L overlay exhibits a columnar dendritic solidification pattern with delta ferrite within the interdendritic spaces. Adjacent to the fusion line, within 0.5 mm, there is a narrow region which contains virtually no delta ferrite. Within this zone, on the overlay side of the boundary, there is a dark etching band of tempered martensite. This band is relatively narrow, extending over most of the interface, but occasionally the tempered martensite extends across the entire austenite zone. The austenite grain boundaries at the interface show that the overlay initially solidified as a planar interface which then progressed into a dendritic solidification mode. The austenite grain boundaries at the interface appear to be continuous with the prior austenite grains in the HAZ of the base plate. The planar austenite grain boundaries in the overlay have been termed Type II boundaries. Figure 28 also shows that carbides precipitate preferentially on the prior austenite grain boundaries in the base plate HAZ, which was a bainitic microstructure.

Carbide precipitation in the base plate HAZ and the continuity of the austenite grain boundaries across the fusion line are shown in another 750 A overlay in Figure 29. The tempered martensite "feathers" extended from the fusion line into the overlay. The planar austenite grains in the overlay and corresponding Type II boundaries were not totally continuous. In some regions, the dendritic austenite/ferrite structure extended directly from the Cr-Mo baseplate. Since these Type II grain boundaries apparently promoted disbonding, the presence of such grains was quantified,(Table 10) and can be seen to range from 9 percent in C2 to 91 percent in B1. The lower percentages of Type II boundaries were associated with the 1500 A overlays.

The 309L overlay deposits are shown in Figure 30 (750 A overlay) and Figure 31 (1500 A overlay). Overall, deposits from both procedures exhibit similar volume fractions of ferrite and austenite, and comparable inclusion sizes. There appeared to be a qualitative difference in the continuity of the interdendritic ferrite. The ferrite in the 750 A overlay (Figure 30) appeared to be more continuous and prominent than that for the 1500 A overlay (Figure 31).

The extent of sigma phase formation in the overlay due to PWHT was evaluated by electro-polishing. The potassium hydroxide reagent stains chi and sigma phases yellow to reddish brown, ferrite appears grey to bluish-grey, carbides are barely touched, and austenite remains unetched or stained. Figure 32 showed interdendritic sigma phase in sample B1B. The 1500A procedure samples exhibited less sigma phase than procedure 1 (750 A) samples.

The individual ultrasonic results are presented in Appendices B and C and are summarized in Table 11 and Figure 33. Apart from the sample numbers and the UT disbonding results, the test lab identification and hold time at temperature are also included in Table 11. A comparison of results between lab A and E did not indicate any differences in disbonding, even though lab A samples tended to have been held at temperature longer than those from lab E by as much as 10 hours.

The results plotted in Figure 33 show that the disbonding percentage decreases at the slower cooling rates, but even at 56 and 28°C/h, there is still extensive disbonding. It is also apparent from the figure that there is no real difference between the two welding procedures in their disbonding performance.

3.3 Metallographic Examination After Autoclave Tests

The cracks in the disbonded specimens were all observed in the interface region. In most instances, the cracks propagated along the Type II grain boundaries in the overlay, as in Figure 34. There were examples along the same section that also showed intergranular cracks within the tempered martensite layer along the fusion boundary. In all cases the cracks were intergranular, as in Figures 35 and 36. These observations indicate that Type II boundaries and the grain boundaries within the tempered martensite region are susceptible to disbonding during reactor cooling.

In order to ascertain which characteristics were associated with crack initiation, five autoclave samples with from 3 to 47 percent disbonding were sectioned and metallographically examined. Each sample was wide enough so as to include bonded and disbonded areas. In all instances crack initiation was observed only along the Type II grain boundaries, and the disbonding

did not extend beyond the limits of the Type II boundaries. The cracks in the specimens with 41 and 47 percent disbonding coincided primarily with Type II boundaries, while there was also some cracking along the fusion boundary.

During the ultrasonic examination, some of the autoclave samples produced indications at two distinct depths from the Cr-Mo surface. This suggested that there could be additional cracking in the carbon steel baseplate away from the fusion line. Subsequent metallographic examination of these areas showed that all cracks were along either the Type II boundaries or in the carbon-enriched stainless zone. Variations in penetration of the overlay (Table 6) were the cause for what appeared to be reflections at different positions from the surface due to a change in the speed of sound.

3.5 CANMET Samples

The F series overlay samples were prepared by CANMET using a low carbon buttering layer of 2.25 Cr-1Mo steel on top of the existing base metal. The 309L was then deposited on the buttered layer. The purpose of the experiment was to reduce the available carbon for diffusion from the base metal into the 309L and thus reduce the possiblity of alloy carbide formation at Type II planar boundaries in the 309L. The grain boundary carbides are considered to be initiation sites for cracking in the 309L leading to disbonding. The autoclave test results were significant in that F1A1 (222°C/h cooling rate) exhibited less disbonding compared to other samples made by procedure 1 and subject to the 222°C/h cooling. Sample F1A3 (56°C/h) showed only slight disbonding compared to other samples cooled at 56°C/h.

4.0 Discussion of Results

4.1 Side Bend Tests

The ductility of the bond between the overlay and baseplate and the integrity of the weld deposit were determined using 180 degree side bend tests. Randomly distributed ruptures in the overlay, each about 6 mm long, were microfissures caused by insufficient ferrite in the deposit (less than 2 percent). Cracks at the interface, extending parallel to the fusion line and partly into the cladding, indicated excessive martensite. A single crack at the centre of the bead that extends to the neutral axis and to the interface on the surface,

was generally associated with sigma phase. These three crack types are shown schematically in Figure 37a, b and c respectively. Of these, Figure 37b is most representative of the type of cracking exhibited in the B1 overlay samples, and thus one would expect to observe unique features along the B1 fusion line.

Cracking in the first layer of the overlay has been attributed usually to a wide carbon infusion zone (in excess of 120 microns) along the fusion boundary (11, 13), with the cracks running parallel to the fusion line within this layer. The cracks in the B1 overlay, however, were different in that the cracks parallel to the fusion boundary were contained within the heat-affected zone of the Cr-Mo baseplate, approximately 100 microns from the fusion line. The microstructure in this region (Figure 22) was heavily deformed with localized yielding between the crack and the fusion boundary.

There are several unique features in the B1 deposit which could help to explain the behaviour of the bend samples. First, the hardness in the tempered martensite layer was at least 60 DPH lower than the other results. Secondly, the composition of the overlay was closest to that of the E309L electrode, and the Schaeffler diagram predicted only a 7 percent dilution. Furthermore, the B1 reinforcement was as much as 0.5 mm greater than the remaining 750 A deposits. This 15 percent increase in height is directly related to the strip feed speed, 16.1 mm/s for B1 compared to 13.6 mm/s for E1, which is just over 15 percent greater. Therefore, more of the available arc energy was used to melt the strip, resulting in lower penetration and dilution, and a higher reinforcement.

4.2 Dilution

The base metal dilution is primarily influenced by the current and welding speed, and to a lesser extent by the electrical stick-out and voltage (28).

The dimensions of the overlay deposits Table 6 and the measured dilutions Table 5 were related to the individual welding parameters based in Table 4. Of the welds deposited at 750 A, only the increased strip feed speed for deposit B1 and the shorter arc length of E1 noticeably altered the overlay characteristics amongst the five fabricators. In the B1 deposit, this produced a higher reinforcement and consequent lower dilution, even though

similar to welds C and E. Comparing welds D and E, the shorter electrode extension of weld E gave a penetration of 0.79 mm versus 0.55 mm for the D deposit.

The 1500 A overlays were unique in each instance, with only fabricator A matching the recommended procedure. Fabricator C had to reduce the current because of equipment limitations, but this was partly compensated by reducing the travel speed to maintain the same nominal heat input. The E2 overlay was also deposited at a reduced current but without any change in travel speed. Consequently, there was a lower penetration observed for this deposit. The lowest penetration of the 1500 A procedures was observed on the D2 weld where the electrode was inclined two degrees forward.

4.3 Ferrite Measurements

The ferrite content of an austenitic deposit was specified for corrosion resistance while avoiding solidification cracking. This infers, there must be some means of predicting and measuring ferrite content. The Schaeffler and Delong diagrams are useful for predicting the approximate chemistry of the deposit, but actual measurements are preferred using magnetic techniques.

The results have already shown that the procedure 2 welds had greater penetration and dilution than the 750 A deposits. The greater dilution would be expected to reduce the ferrite content in the overlay as predicted from the Schaeffler diagram and the deposit chemistries (Table 7). The measurements in Table 8, however, indicate a higher ferrite content for 1500 A deposits. The ferrite in the 750 A overlays appeared similar to the 1500 A welds (Figure 31). In the latter case, the ferrite network is presumably more continuous. This continuity of ferrite may enhance the magnetic permeability and thus the higher ferrite numbers. This increase in ferrite number with dilution for the two procedures is shown in Figure 38.

4.4 Microstructural Analysis

The most notable features from the metallographic examinations were observed along the fusion line. These included Type II grain boundaries, the tempered martensite layer, and precipitation within both the coarse-grained base metal HAZ and the austenitic deposit.

The sections were examined to determine whether there was some correlation between the thickness of the tempered martensite layers and the Type II grain width. The tempered martensite layer varied greatly in its thickness from 10 to 140 microns, as did the Type II grain width, 10 to 60 microns. No definite correlation could be made between these features. Zones of uniform penetration tended to have the narrower martensite layers. The presence of Type II grains did, however, coincide quite often with large prior austenite grains in the coarse-grained HAZ of the baseplate probably as a consequence of epitaxial growth during weld pool solidification.

4.5 Autoclave Tests

The primary objectives of these tests were to ensure that the disbonding which occurred was identical to that found in the reactor vessels in the field.

The autoclave induced cracks depicted in Figures 34, 35 and 36 were representative of those from actual reactors (20). For the most part, they followed the Type II grain boundaries which ran parallel to the fusion line. In other instances, the cracks would also run through the tempered martensite layer. Cracks in this layer would usually be observed only when there were no Type II boundaries across the same section.

The cooling rates chosen for the autoclave tests were expected to cover the range from complete disbonding at the fastest cooling rates to no cracking at the slowest cooling rate. It is clear from Figure 39 that over 50 percent disbonding was obtained even at the conditions which from practical experience would indicate that cracking should not occur.

4.6 Ultrasonic Inspection of Autoclave Samples

An apparent problem which came to light during the ultrasonic examination of the autoclave samples was the reliability of the manual inspection. The manual procedure was dependent on the familiarity of the operators with the objectives of the exercise, expertise, and attitudes. To improve the reliability, C-scan plots were employed. The computer was not influenced by the surroundings as a technician might.

A comparison of the two inspection techniques was plotted in Figure 40. A reasonably good correlation 1:1 was observed. The area in question, however, was along the 100 percent disbonding line for the manual results, which yielded only 30 to 70 percent disbonding on the automated report. There appears to be some tendency among ultrasonic technicians to exaggerate the actual percentage of disbonding, especially when there is a relatively large degree of cracking. Below 40 percent disbonded area, the manual versus automated results were also unacceptable. Therefore, a manual procedure did not give confidence in identifying whether or not disbonding occurs. Automated techniques would be preferable.

5.0 Conclusions

The experimental results and observations support the following:

1. All five fabricators produced clad deposits which were relatively similar despite small variations in welding parameters.

2. An autoclave test procedure was developed and shown to produce disbonding similar to that observed in service.

3. The presence of hydrogen in the autoclave atmosphere was necessary to produce disbonding.

4. Lower carbon in the baseplate reduced carbon diffusion and the risk of those microstructures associated with disbonding.

5. Strong carbide forming elements also help to reduce the susceptibility to disbonding.

6. There was virtually no difference in the disbonding resistance of the 750A and 1500A overlay procedures.

7. The high heat input, 9kJ/mm, from the SAW cladding procedure had the following thermally induced disadvantages:
   a) slow solidification rates resulting in a Type II grain structure
   b) slow solidification rates assisting the microsegregation of carbon and substitutional elements
   c) slow cooling rates which assisted carbon diffusion into the cladding and fusion boundary
   d) high dilution of the fusion boundary leading to martensitic structures
   e) intensified residual stress fields from the large weld and plate HAZ volumes.

6.0 Recommendation

That a GMAW or FCAW temper bead technique at 2 to 3 kJ/mm replace the SAW procedure. Disbonding will be minimized through a faster cooling rate followed by a tempering thermocycle. This procedure:

1. minimizes poor solidification microstructures.
2. minimizes segregation.
3. minimizes interstitial and substitutional diffusion.
4. reduces the amount of dilution minimizing adverse fusion line microstructures.
5. reduces the weld and plate HAZ volumes that give rise to residual stress.
6. tempers the previous pass normalizing the microstructure and annealing residual stress.

One series of overlays should be produced with the twin wire GMAW technique as a follow on. A friction welded surface would provide additional experimental control.

7.0 References

1. Y. Murakami, J. Watanabe, and S. Mima, "Heavy Section Cr-Mo Steels for Hydrogenation Services", presented at 17th CIM Annual Conference of Metallurgists, Montreal, August 27-31, 1978, The Japan Steel Works, Ltd.

2. J. Sims and G.J. Bruck," Factors Influencing the Performance of Stainless Steel Overlays in High Temperature Hydrogen Service", ibid.

3. T. Sakai, K. Asami, M. Katsumata, H. Takada, and O. Tanaka, "Hydrogen Induced Disbonding of Weld Overlay in Pressure Vessels and its Prevention", Current Solutions to Hydrogen Problems in Steels, Proceedings of the First International Conference, ASM, Washington, D.C., Nov. 1982, p340.

4. W.F. Savage "Solidification, Segregation, and Weld Imperfections", Welding in the World, Vol 18(5/6), 1980, p89.

5. K. Ohnishi, A. Fuji, R. Chiba, T. Adachi, K. Naito, and H. Okada, "Effect of Strip Overlay Welding Conditions on Resistance to Hydrogen-Induced Disbonding - Study on a Stainless Steel Overlay Welding Process for Superior Resistance to Disbonding (Report 1)", Transactions of the Japan Welding Society, Vol 5(2), October 1984, p49.

6. G.M. Pressouyre, J.M. Chaillet, and G. Valette, "Parameters Affecting the Hydrogen Disbonding of Austenitic Stainless Cladded Steel", ibid.

7. "Improvement of Disbonding Susceptibility by High Speed Overlay Welding with Strip Electrode", Welding Technical Report No. 541, Kobe Steel, Ltd., Welding Division.

8. A Fuji, E. Kudo, T. Takahashi, "Metallographic Characteristics of Stainless Steel Overlay Weld With Resistance to Hydrogen Induced Disbonding", Transactions of JWS, Vol 17(2), 1986, p43.

9. T. Hattori, T. Fujita, K. Kinoshita, A. Ebata, H. Tsukamoto and M. Ando "Hydrogen Induced Disbonding of Stainless Steel Overlay Weld and its Preventive Measures", Nippon Kokan Technical Report, Overseas No. 47(1986).

10. R.J. Christoffel and R.M. Curran, "Carbon Migration in Welded Joints at Elevated Temperatures", Welding Journal, Vol 35(9), 1956, p457-s.

11. M. Inagaki, T. Fujimura, and T. Kodaira, "Studies of Overlaid Cladding in a Nuclear Reactor Vessel", IIW Doc. IX-843-73 or XI-283-73.

12. M. Eriksson, cited in reference 2.

13. T. Fujii, T. Hazama, H. Nakajima, and R. Horita, "A Safety Analysis on Overlay Disbonding of Pressure Vessels for Hydrogen Service". Current Solutions to Hydrogen Problems in Steels, Proceedings of the First International Conference, ASM, Washington, D.C., Nov. 1982, p361.

14. K. Kinoshita, H. Itoh, and A. Ebata, "Characteristics for Hydrogen Diffusion of Transition Zone Metals Between Stainless Steel Weld Overlay and Cr-Mo Steel Base Metal", ibid, p369.

15. R. Kume, H. Okabayashi and T. Naiki "Internal Stresses in Thick Plates Weld-Overlaid with Austenitic Stainless Steel (Report 1), Transactions of the Japan Welding Society, Vol 5(1), April 1974, p32.

16. J. Watanabe, K. Ohnishi, R. Chiba, K. Naito, H. Okada, and A.G. Ingram, "Hydrogen-Induced Disbonding of Stainless Weld Overlay Found in Desulfurizing Reactor", Conf. Performance of Pressure Vessels with Clad and Overlaid Stainless Steel Linings, Denver, June 1981, ASME Publication MPC-16.

17. A. Fuji, E. Kudo, T. Takahashi, and K. Mano, "Mechanical Properties of Stainless Steel Overlay Weld with Resistance to Hydrogen-Induced Disbonding", Transactions of the Japan Welding Society, Vol 17(1), April 1986, p27.

18. A.P. Chakravarti and L. Malik, Modelling Hydrogen Distribution in Weld Overlay System, Report 7-186-0631F, AMCA International, November 1986.

19. N. Morishige, R. Kume, and H. Okabayashi, "Influence of Low Temperature Hydrogen Degassing on Hydrogen-Induced Disbonding of Cladding", Transactions of the Japan Welding Society, Vol 16(1), April 1985, p12.

20. H. Okada, K. Naito, J. Watanabe, K. Ohnishi, and R. Chiba, "Hydrogen-Induced Disbonding of Stainless Weld Overlay in Hydrodesulphurizing Reactor", Current Solutions to Hydrogen Problems in Steels, Proceedings of the First International Conference, ASM, Washington, D.C., Nov. 1982, p331.

21. F.Matsuda, H. Nakagawa, S. Tsuruta and Y. Yoshida, "Disbonding Between 2 1/4 Cr-1Mo Steel and Overlaid Austenitic Stainless Steel by Means of Electrolytic Hydrogen Charging Technique". Transactions of JWRI, Vol. 13(2), 1984, p91.

22. A.J. Breen, "Low Alloy Steels in Oil Refinery Service, Part 1 - Materials Selection", Metal Construction, Vol 16 (11), November 1984, p671.

23. A. Bernstein, A. Backman, M. Areskoug, and S. Forsberg, "Surfacing with Stainless Steel Strip Electrodes", Welding Journal, Vol 54, September 1975, p647.

24. D. Yamazaki, and others, cited as ref (3) by Y. Murakami, (1).

25. D. Popovits and T. Subu, "Graphical Determination of the Dilution at Submerged Arc-Strip Cladding", IIW Doc IX-1287-83.

26. R. Blondeau, G.M. Pressouyre, A. Cheviet, J.A. Berthet, J.M. Duranseaud, "Contribution to a Solution to the Disbonding Problem in 2 1/4 Cr - 1 Mo Heavy Wall Reactors, Conf Current Solutions to Hydrogen Problems in Steel, ASM, Washington, D.C., November 1982.

27. J. McGrath et al "Weld Overlay Disbonding" Metal Technologies Laboratory Report MTL 88-26 (Int)/EMR 19-4-88.

28. R.S. Chandel and R.F. Orr, "Submerged Arc Strip Overlay Welding of 2.25Cr-1Mo Steel", Welding in Energy-Related Projects (Toronto, Ontario: Pergamon Press, 1984), p311.

29. Stainless Welding Engineering, Stoody Company, Industry, California, 1977, p42.

30. ASTM E562-83

31. J.F. Clayton, "Carbide Distribution in Weld Overlay Interface", FAMEX Engineering, Brampton, November 1986.

32. R.S. Chandel and R.F. Orr, Effect of Process Variables on the Bead Geometry of the Submerged-Arc Strip-Overlay Welds, Physical Metallurgy Research Laboratories, Report MRP/PMRL 83-45 (OP-J), Ottawa, June 1983.

33. N.T. Dick, "Pressure Vessel Cladding Techniques", Welding Research Related to Power Plants (London, UK: Central Electricity Generating Board, 1972), p490.

TABLE 1

Hydrogen Modelling (18)

Assumptions used to Generate Figure 11

Computer Modelling

Run	Steady State Temperature °C	Overlay Thickness mm	Hydrogen Pressure kg/cm^2	Cooling Rate °C/h	Baseplate Thickness mm	Peak Hydrogen Concentration ppm	
						Single	Double
1	450	5	155	-28	62	149	243
2	450	5	155	-56	62	168	257
3	450	5	155	-111	62	185	270
4	450	5	155	-222	62	201	285
5	450	10	155	-28	200	200	62
6	450	10	155	-56	200	215	67
7	450	10	155	-111	200	231	73
8	450	10	155	-222	200	247	79
9	450	10	155	-28	300	225	61
10	450	10	155	-222	300	274	78
11	450	5	155	-28	200	231	141
12	450	5	155	-222	200	287	184
13	500	10	155	-28	200	176	79
14	500	10	155	-222	200	209	96
15	450	10	175.77	-28	200	213	66
16	450	10	175.77	-222	200	263	84
17	500	10	175.77	-28	200	187	84
18	500	10	175.77	-222	200	223	103

TABLE 2

Critical Stress Intensity Factor

of Hydrogenated Reactor Wall Materials

Material	Exposure Condition	Absorbed Hydrogen Content	Critical Stress Intensity Factor	Reference
Weld overlay (Type 347)	425°C (797°F)		109.3 kg-mm3/2 (33.9 MPA /m)	(3)
Weld overlay (Type 308)	140 kg/cm2He 137 MPa He)		152.3 kg-mm3/2 (47.2 MPa /m)	(3)
Transition Zone	450°C (842°F) 150kg/cm2He (1147 MPa He	3.1 ppm in base metal	15-20 kg-mm3/2 (47-62 MPa /m)	
2.25Cr-1Mo 0B=113 kg/mm2 (1,1082 MPa)	454°C 850°F 175 kg/cm2 H_2 (172 MPa He)	4-5 ppm	75.8 kg-mm3/2 (23.5 MPa /m)	(4)
2.25 Cr-1Mo 0A=70kg/mm2 (686.5 MPa)			283.4 kg-mm3/2 (87.8 MPa /m)	(4)

NOTE: These critical stress intensity factor values were obtained by the bolt load K_{IH} test, from (20).

TABLE 3

Chemical Compositions of Baseplate and Strip Electrode

Material	Chemical Composition, wt %										
	C	Mn	Si	S	P	Ni	Cr	Mo	Cu	Ti	Ta
2.25 Cr - 1 Mo	0.135	0.565	0.24	0.003	0.005	0.16	2.27	1.0	0.11	0.004	-
E309 L	0.016	1.77	0.42	0.003	0.010	13.15	23.55	0.03	0.37	0.07	0.01
	Co	Sn	Al	Nb	V	Zr	B	As	Sb		
2.25 Cr -1 Mo	0.01	0.008	0.025	0.02	0.007	-	0.0003	0.015	0.002		

TABLE 4

Welding Conditions

	Fabricator				
	A	B	C	D	E
Procedure 1					
Current, A	750±25	750±25	750±60	750	750
Voltage, V	27-28	27.5	28	28	27-28
Travel Speed, mm/min	140	140	140	140	140
Preheat, °C	148	148	148	150	148
Interpass, °C	163	232	177	200	316 max.
PWHT, °C/min	607/30	607/30	607/30		607/30
E.S.O., mm	35	35	32	33-37	25
WFS, mm/s	-	16.1	-	-	13.6
Angle	90°	90°	90°	2°	2°
Procedure 2					
Current, A	1500±25		1400±60	1500±50	1450
Voltage, V	27-28		28	28	27-28
Travel Speed, mm/min	280		260	280	280
Preheat, °C	148		148	150	148
Interpass, °C	163		177	200	316
PWHT, °C/min	607/30		607/30		607/30
E.S.O., mm	35		32	33-37	25
WFS, mm/s	-		-	-	31.3
Angle	90°		90°	2°	2°

TABLE 5

Dilution Measurements of Overlay Samples

Plate	Sample Length mm	Average Dilution percent	Dilution in Micro-specimen, percent	
A1.2 (750A)	122	24	29	24
B1	135	16	18	18
C1	144	18	12	16
D1	103	12	15	15
E1	146	19	10	26
A2.2 (1500A)	122	35	37	27
C2	99	31	38	24
D2	132	22	14	21
E2	126	25	29	34

TABLE 6

Penetration and Overlay Reinforcement Measurements

Plate	Penetration			Reinforcement		
	mean	standard deviation	variance	mean	standard deviation	variance
A1.2	1.158	0.388	0.134	3.686	0.409	0.149
B1	0.816	0.263	0.060	4.22	0.304	0.081
C1	0.771	0.230	0.046	3.824	0.420	0.154
D1	0.553	0.405	0.144	3.850	0.327	0.093
E1	0.787	0.334	0.105	3.717	0.309	0.090
Averages	0.82	0.32	0.10	3.86	0.35	0.11
A2.2	1.878	0.691	0.424	3.838	0.303	0.082
C2	1.671	0.770	0.527	4.082	0.225	0.045
D2	1.059	0.712	0.443	4.359	0.747	0.489
E2	1.359	0.497	0.212	4.211	0.399	0.136
Averages	1.49	0.67	0.40	4.12	0.42	0.19

NB: A,B,C,D,E, are the different fabricators in table 4

TABLE 7

Chemical Analysis of Overlay Deposits

Specimen	Chemical Composition, wt %								
	C	Mn	Si	Ni	Cr	Mo	Cu	Ni_{eq}(a)	Cr_{eq}(b)
(750 A)									
A1.1	0.076	1.43	0.78	9.81	19.3	0.24	0.07	12.81	20.71
B1	0.065	1.49	0.90	11.7	21.2	0.15	0.05	14.40	22.70
C1	0.054	1.44	0.80	9.70	20.0	0.22	0.06	12.04	21.42
D1	0.066	1.44	0.89	9.97	19.9	0.34	0.05	12.67	21.58
E1	0.044	1.41	0.86	10.20	20.3	0.29	0.05	12.23	21.88
(1500 A)									
A2.1	0.074	1.31	0.65	8.66	17.1	0.34	0.08	11.54	18.42
C2	0.089	1.32	0.73	8.37	17.7	0.34	0.06	11.70	19.14
D2	0.066	1.32	0.67	8.65	17.5	0.20	0.06	11.29	18.71
E2	0.054	1.34	0.68	9.14	18.3	0.23	0.06	11.43	19.55

(a) Ni_{eq} = %Ni + 30 %C + 0.5 %Mn

(b) Cr_{eq} = %Cr + %Mo + 1.5%Si + 0.5%Nb

NB: A,B,C,D,E, are the different fabricators in table 4

TABLE 8

Weld Overlay Ferrite Numbers

Plate	Magne-Gage	Forster Meter
A1.2 (750 A)	4.2	2.7
B1	2.7	1.8
C1	4.4	3.1
D1	3.5	2.3
E1	2.5	1.9
A2.2 (1500 A)	6.3	3.7
C2	8.6	5.0
D2	7.8	4.0
E2	5.0	3.7

TABLE 9

Microhardness Traverses (50 g) Across Fusion Lines

	Distance From Fusion Boundary mm	Plate								
		A1.2	B1	C1	D1	E1	A2.2	C2	D2	E2
	3.0	193	185	206	206	227	223	221	223	210
	2.0	195	195	199	210	208	229	232	221	218
	1.0	198	168	192	213	223	224	250	232	224
	0.5	210	202	191	196	199	212	250	234	213
overlay	0.4	215	186	197	204	210	203	261	224	221
	0.3	241	186	191	208	205	211	287	210	229
	0.2	250	191	207	199	205	210	220	229	218
	0.15	266	193	199	213	207	215	220	228	233
	0.10	242	217	224	224	212	220	245	227	249
	0.05	224	217	241	220	229	233	233	240	229
boundary		426	346	420	435	412	473	409	407	426
	0.05	177	164	164	174	173	177	181	182	187
	0.10	174	164	148	178	179	183	188	179	190
	0.15	176	174	172	172	191	188	184	177	187
baseplate	0.20	177	184	178	184	183	187	192	179	190
	0.3	187	179	187	194	189	192	188	187	198
	0.4	190	183	194	199	197	202	186	191	202
	0.5	197	186	200	203	206	190	197	185	202
	1.0	193	196	192	203	210	191	207	193	201
	2.0	198	200	188	212	203	202	201	197	220
	3.0	203	197	195	205	200	222	205	200	197

NB: A,B,C,D,E, are the different fabricators in table 4

TABLE 10

Summary of Quantitative Analysis
of Type II Fusion Boundary Grains

Specimen		Percentage of Type II Grains
A1.2A	(750 A)	66
B1A		91
C1A		47
D1A		26
E1A		63
A2.2A	(1500 A)	54
C2A		9
D2A		15
E2A		39

NB: A,B,C,D,E, are the different fabricators in table 4

TABLE 11

Autoclave Disbonding Summary

Overlay Coupon	Specimen Number	Test Lab	Hold Time h	Cooling Rate °C/h	Disbonded Area Manual %	Disbonded Area Mechanized %
A1	A1.1A1	E	48	222	92	61
	A1.1A2	E	48	111	95	75
	A1.2A5	A	50 to 58	111	90	59
	A1.1A3	E	48	56	62	60
	A1.2A6	A	50 to 58	56	100	-
	A1.2A4	E	48	28	17	33
A2	A2.1A1	A	76*	222	42	75
	A2.1A2	A	50 to 58	111	42	32
	A2.2A5	E	48	111	47	36
	A2.1A3	A	50 to 58	56	32	27
	A2.2A4	A	50 to 58	28	100	51
B1	B1A1	E	48	222	95	62
	B1A2	E	48	111	67	58
	B1A5	A	50 to 58	111	100	48
	B1A4	E	48	56	61	42
	B1A6	A	50 to 58	56	100	58
	B1A3	E	40	28/56	30	56
C1	C1A1	E	48*	222	95	74
	C1A5	A	76	222	75	81
	C1A2	E	48	111	63	67
	C1A6	A	63	111	100	65
	C1A4	E	48	56	60	64
	C1A3	E	40	28/56	46	70
	C1A7N2	A	50 to 58	222	0	0
	C1A8N2	A	50 to 58	111	5	0
	C1A9N2	A	50 to 58	56	5	0

TABLE 11
(continued)
Autoclave Disbonding Summary

Overlay Coupon	Specimen Number	Test Lab	Hold Time h	Cooling Rate °C/h	Disbonded Area Manual %	Disbonded Area Mechanized %
C2	C2A1	A	76*	222	95	93
	C2A5	E	48	222	95	54
	C2A2	A	63	111	100	64
	C2A3	A	50 to 58	56	100	54
	C2A4	A	50 to 58	28	100	60
D1	D1A1	E	48	222	94	47
	D1A5	A	50 to 58*	222	67	78
	D1A2	E	48	111	77	62
	D1A6	A	63	111	100	41
	D1A3	E	48	56	23	30
	D1A4	E	48	28	3	5
D2	D2A1	A	50 to 58*	222	69	92
	D2A2	A	50 to 58	111	100	49
	D2A3	A	50 to 58	56	100	37
	D2A5	E	40	28/56	4	27
	D2A4	A	50 to58	28	(30)?	10
E1	E1A1	E	48	222	86	60
	E1A2	E	48	111	90	58
	E1A5	A	50 to 58	111	95	68
	E1A3	E	48	56	74	63
	E1A4	E	48	28	3	10
	E1A6	A	50 to 58	28	(100)?	33

TABLE 11

(continued)

Autoclave Disbonding Summary

Overlay Coupon	Specimen Number	Test Lab	Hold Time h	Cooling Rate °C/h	Disbonded Area	
					Manual %	Mechanized%
E2	E2A1	A	50 to 58*	222	41	46
	E2A2	A	50 to 58	111	95	49
	E2A3	A	50 to 58	56	100	46
	E2A5	E	48	56	39	38
	E2A4	A	50 to 58	28	(50)?	16
	E2A6N2	A	50 to 58	222	0	0
	E2A7N2	A	50 to 58	111	0	0
	E2A8N2	A	50 to 58	56	0	0
F1	F1A1	A	50 to 58	222	100	35
	F1A2	A	50 to 58	111	(80)?	69
	F1A3	A	50 to 58	56	(10)?	2

* Slow cool

Lab A was University of Alberta

Lab E was ESSO Petroleum

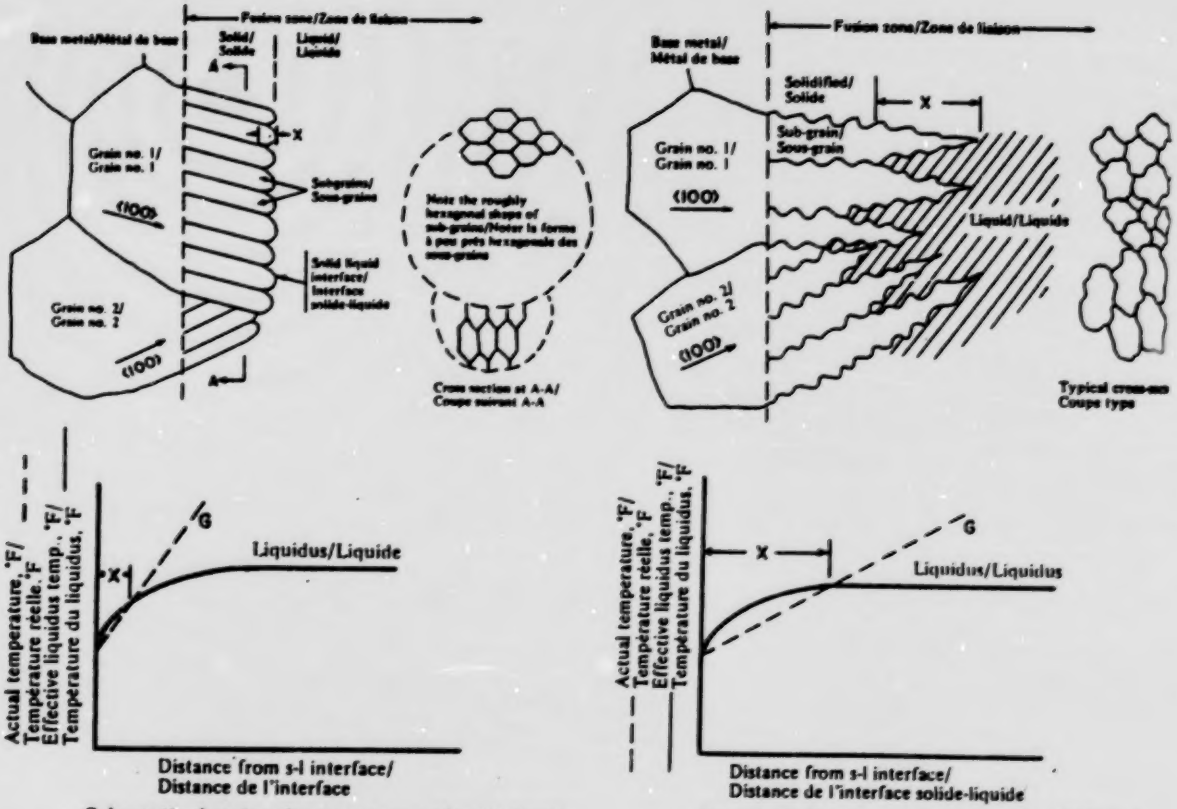

Schematic showing the appearance of solid-liquid interface during cellular growth mode of solidification/ Diagramme schématique illustrant l'aspect de l'interface solide/liquide dans le mode de croissance cellulaire au cours de la solidification.

Schematic showing appearance of solid-liquid interface during cellular-dendritic mode/Diagramme schématique illustrant l'aspect de l'interface solide/liquit dans le mode de croissance cellulaire dendritique.

Figure 1. Schematic representation of microstructures for various growth modes, ref (4).

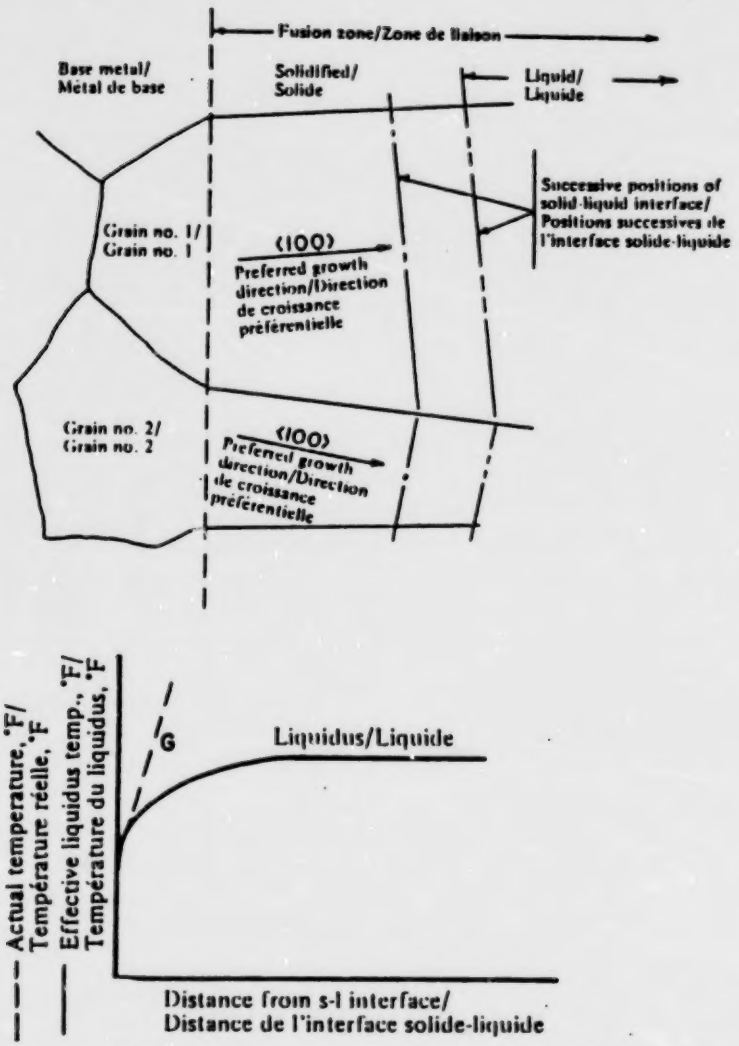

Schematic showing the appearance of solid-liquid interface during planar growth mode of solidification/

Figure 1 (continued). Schematic representation of microstructures for various growth modes, ref (4).

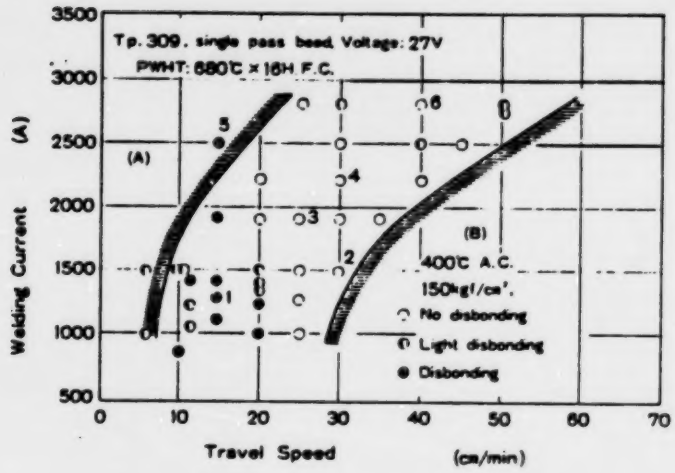

(a) Effects of welding current and travel speed on disbonding test results, from (5).

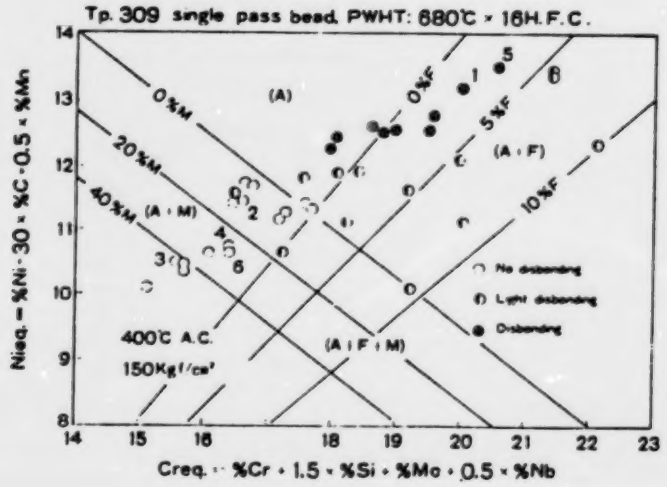

(b) Effect of microstructure on disbonding test results, from (5).

Figure 2. Disbonding results related to welding current, travel speed and microstructure.

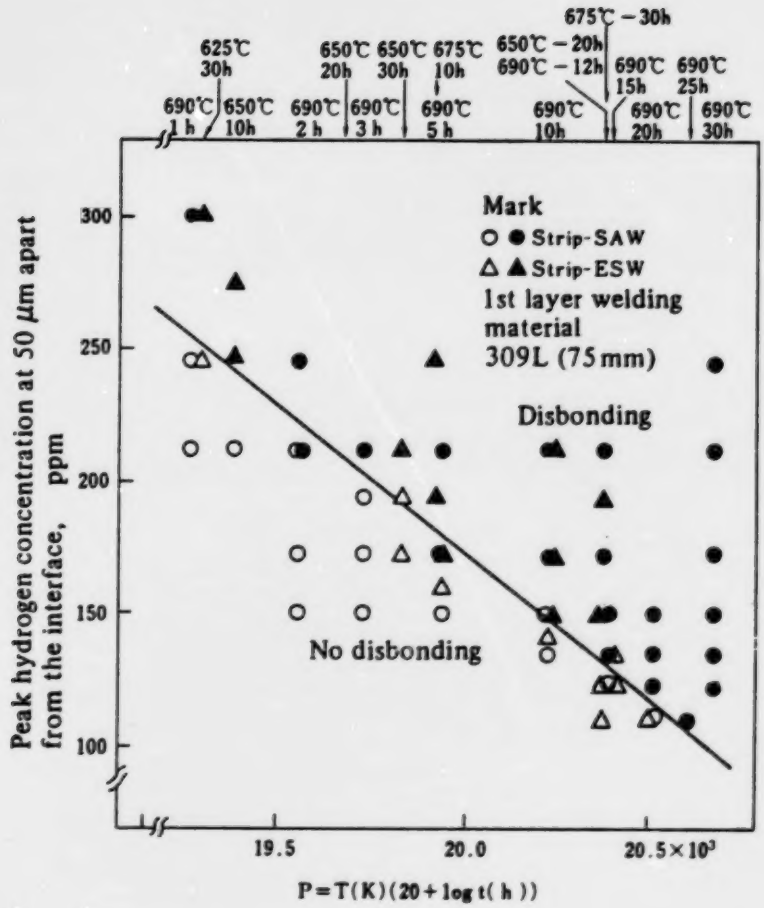

Figure 3. Effect of PWHT condition on hydrogen induced disbonding, from (9).

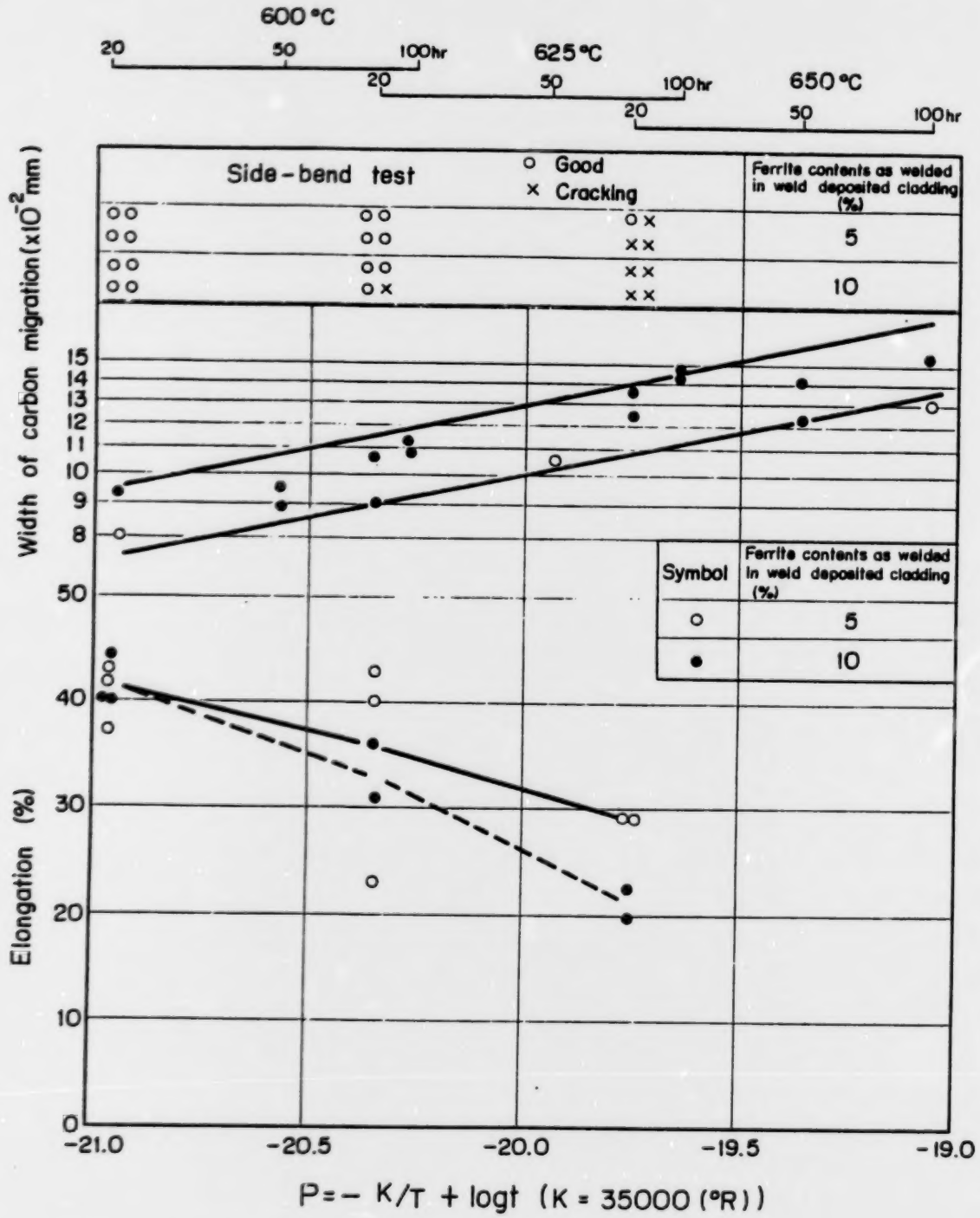

Figure 4. Change of the distance of carbon migration and ductility of weld bond as a function of time and temperature (from 11).

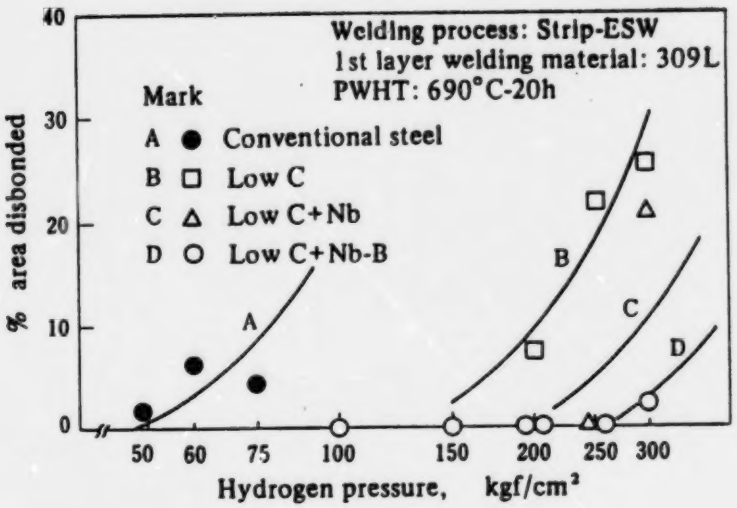

Figure 5. Effect of interlayer overlay weld on hydrogen induced disbonding, from (9).

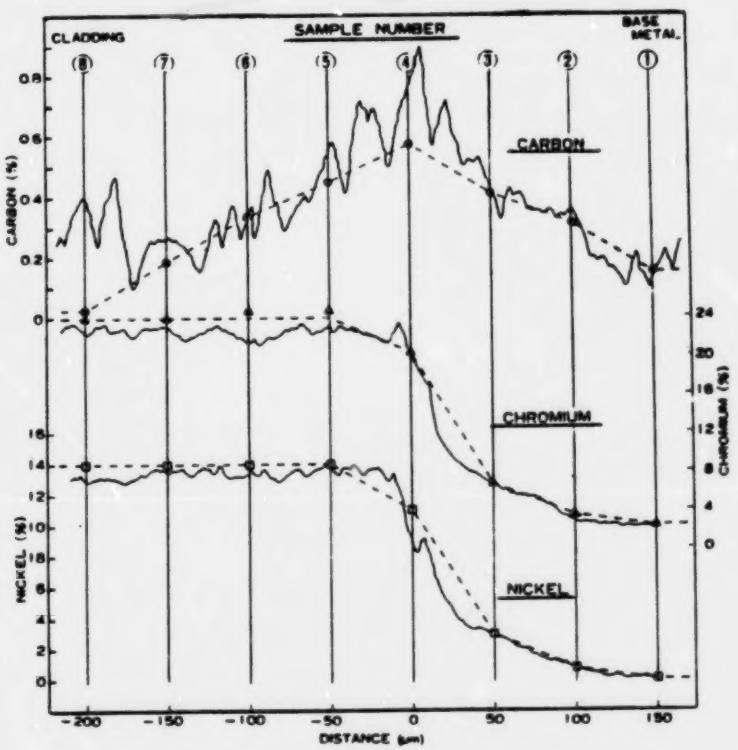

Figure 6. Changes of chemical compositions in the transition zone and chemical compositions of each sample, from (14).

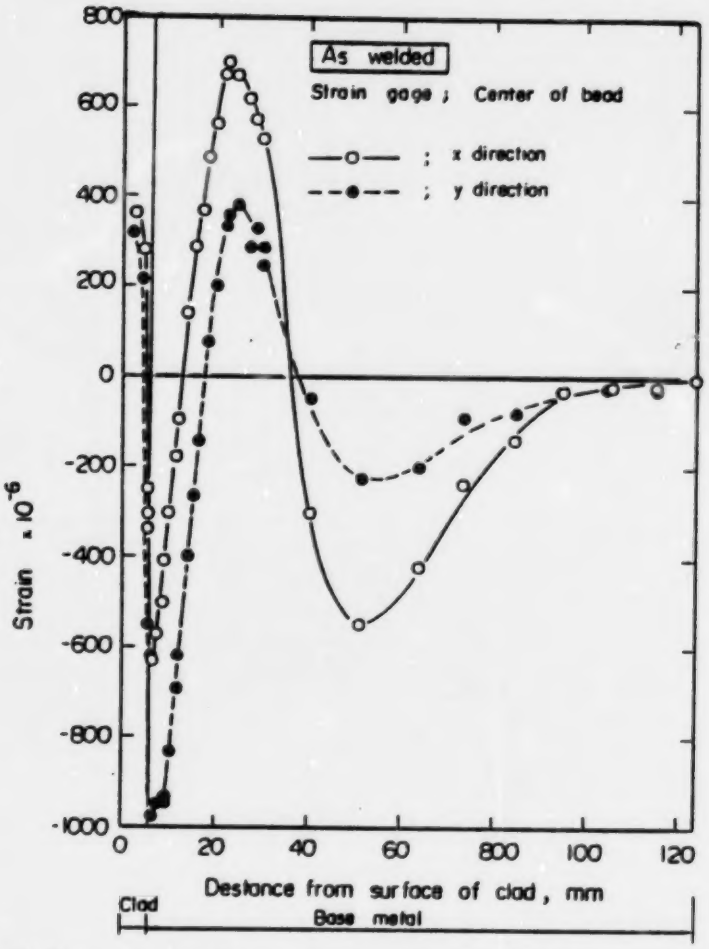

Figure 7. Variation in surface strain due to slicing. Location of strain gauge, centre of bead. As welded, from (15).

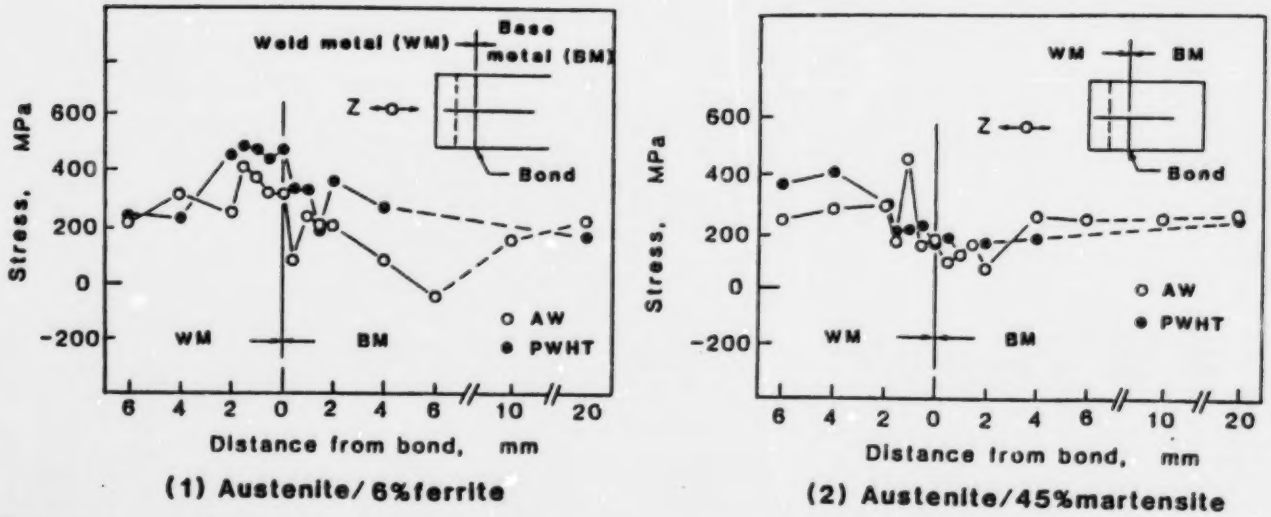

Figure 8. Distribution of the residual stresses in through-thickness direction across the overlay welds, from (17).

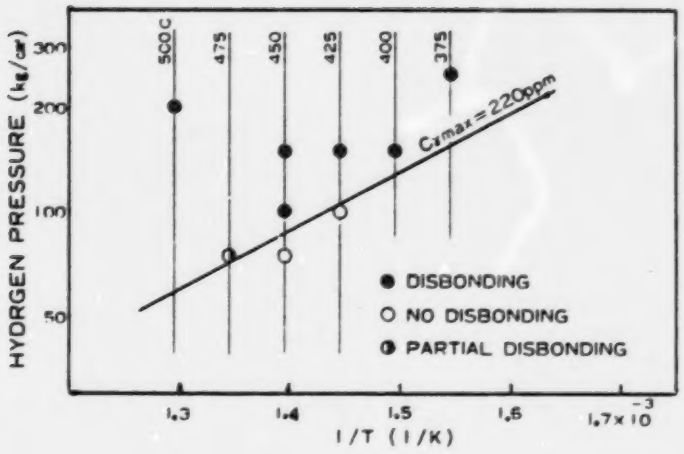

Figure 9. Hydrogen induced disbonding test results, from (14).

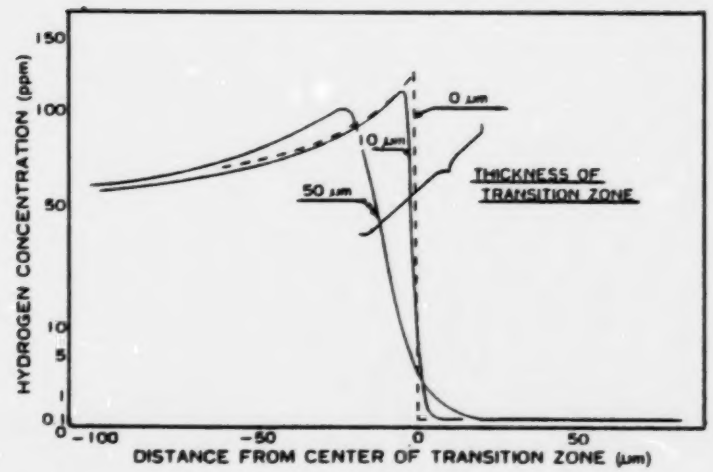

Figure 10. Hydrogen distribution across the fusion line for a 10 micron wide interface, from (14).

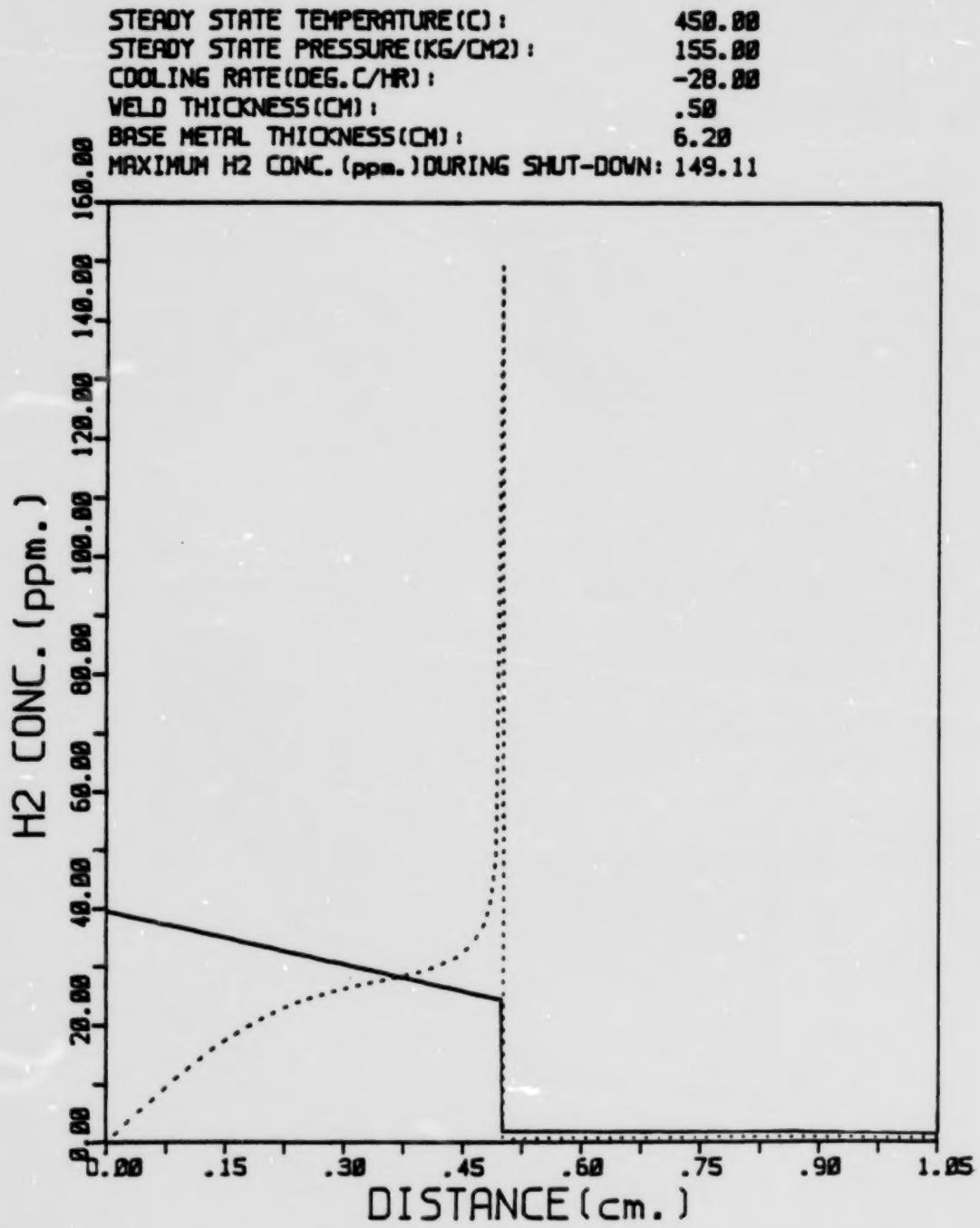

Figure 11. Peak hydrogen concentration profile for typical autoclave test cooled at -28°C/h, from (18).

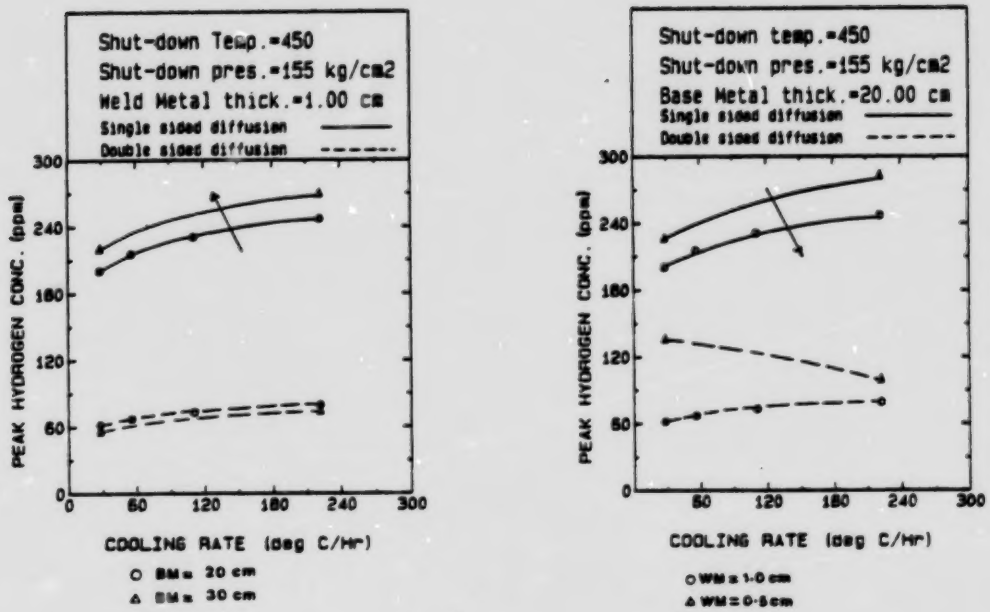

Figure 12. Effects of cooling rate, base metal and overlay thickness on hydrogen concentration, from (18).

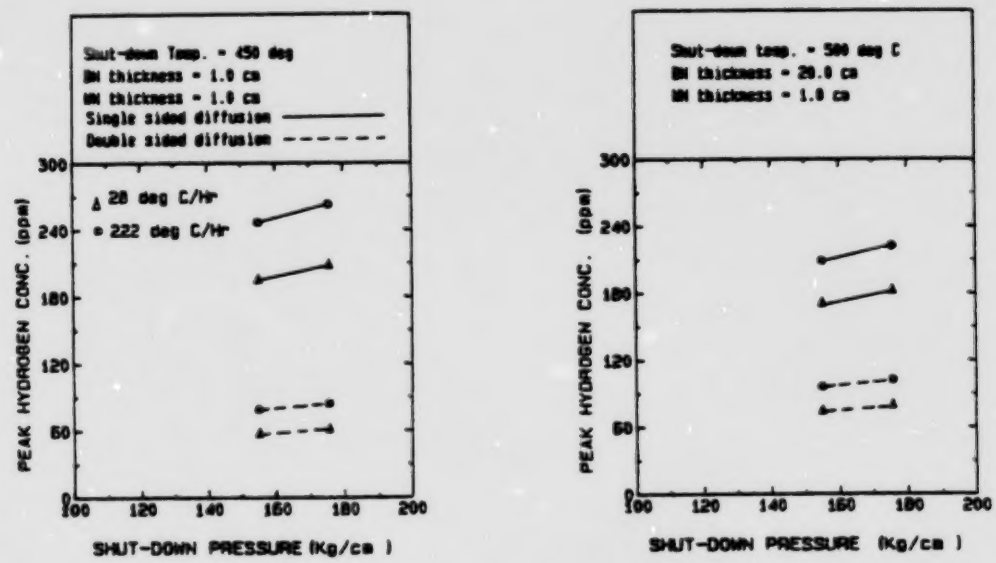

Figure 13. Effect of shutdown pressure on hydrogen concentration, from (18).

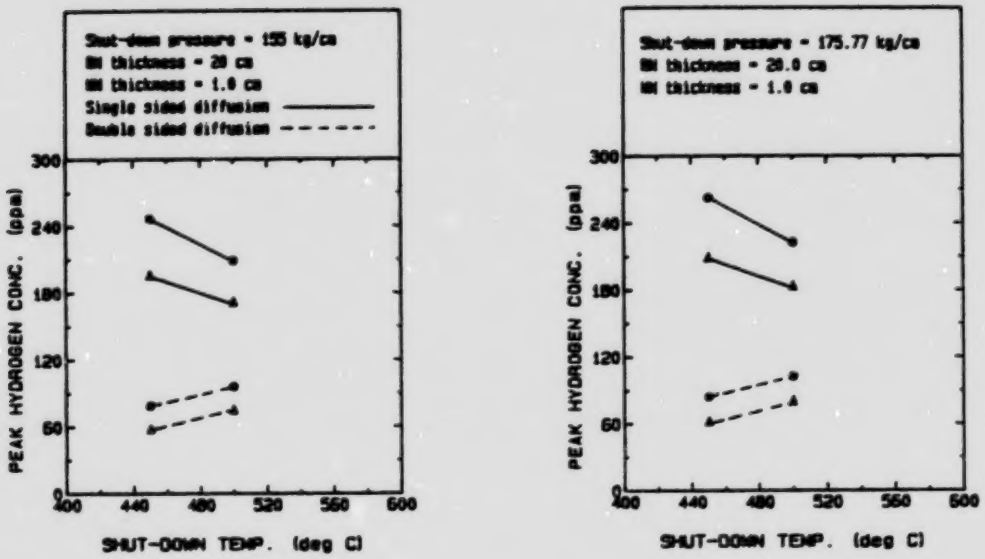

Figure 14. Effects of shutdown temperature on hydrogen concentration, from (18).

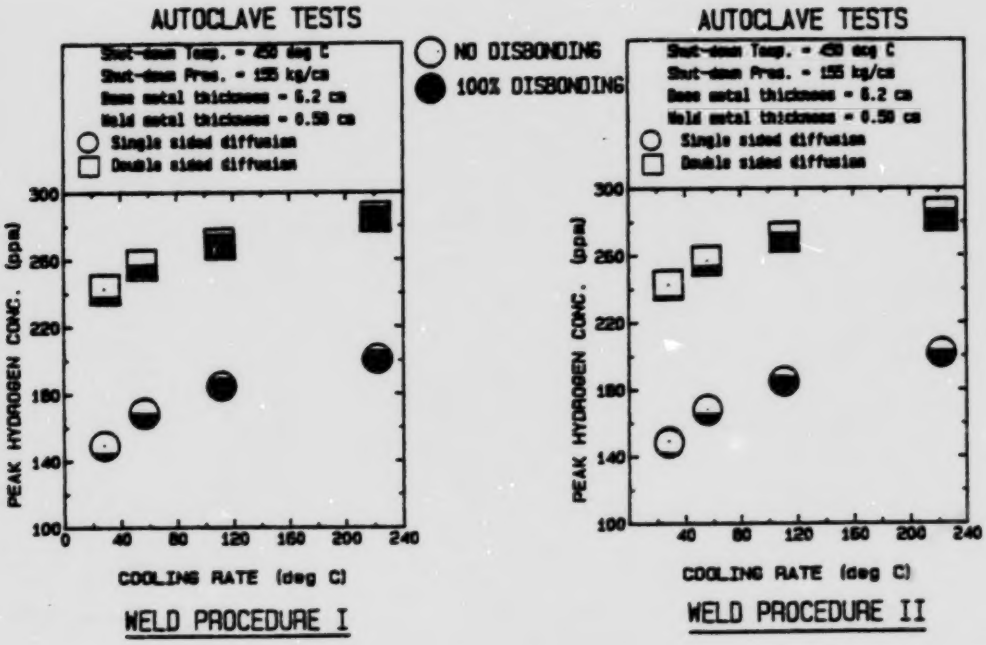

Figure 15. Correlation of peak hydrogen concentration obtained from computer model and % disbonding from autoclave tests, from (18).

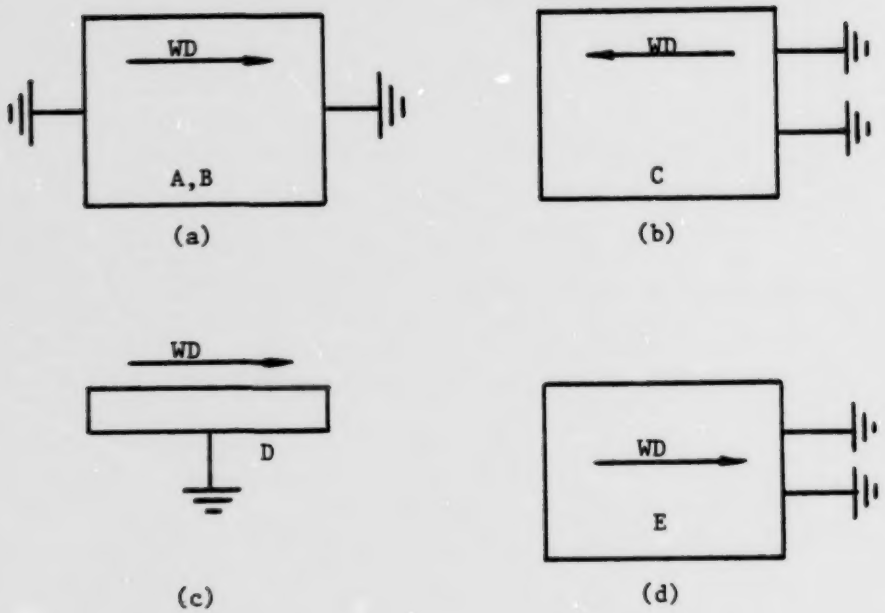

WD = Welding Direction

Figure 16. Grounding arrangements observed during welding: (a) ground attached to either end of plate; (b) welding away from the ground; (c) ground attached to positioner table; (d) welding towards ground.

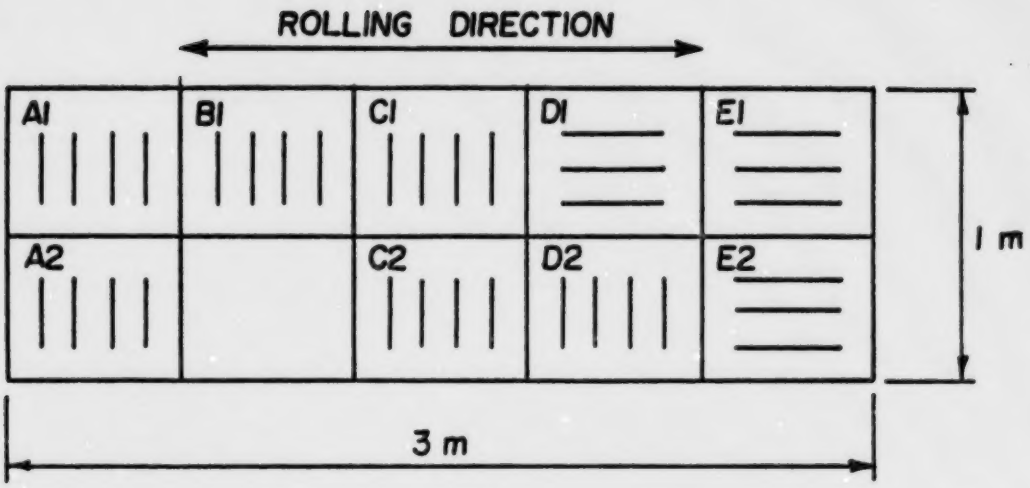

Figure 17. Summary of weld overlay deposition with respect to the principal rolling direction of the 2.25 Cr-1Mo baseplate.

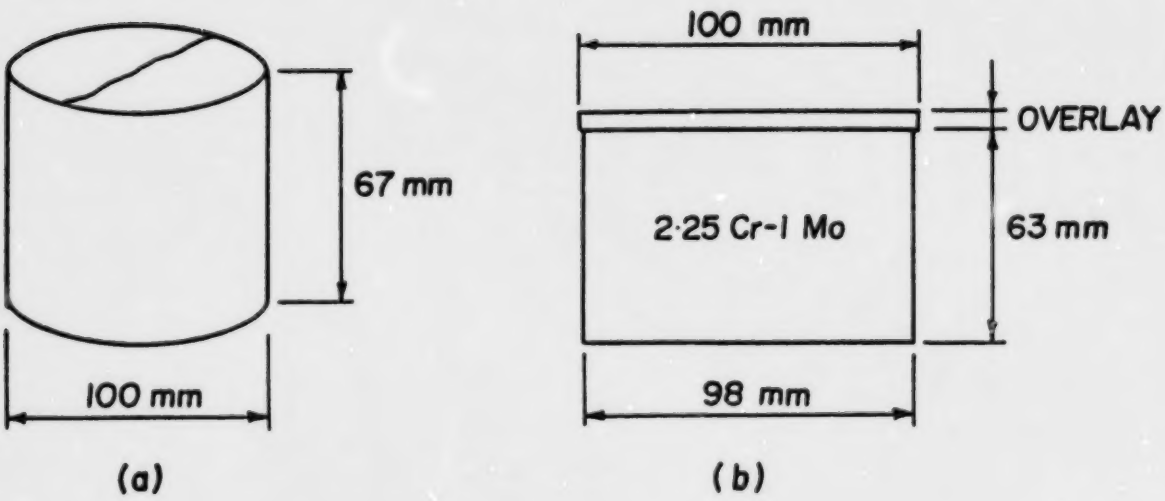

Figure 18. a) General view of autoclave specimen; (b) autoclave coupon before being surfaced along the sides with 316 SMAW electrodes.

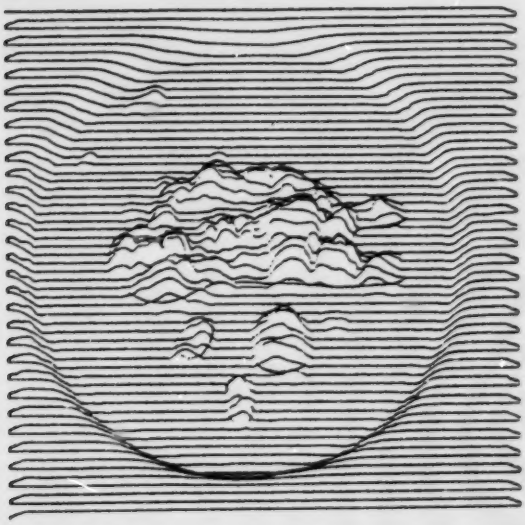

Figure 19. Pseudo-C-scan plot of disbonded areas from mechanized ultrasonic scanning of sample D2A5.

Figure 20. Example of cracking in sample B1A1 after 180 degree bend test. Neg. CF39.

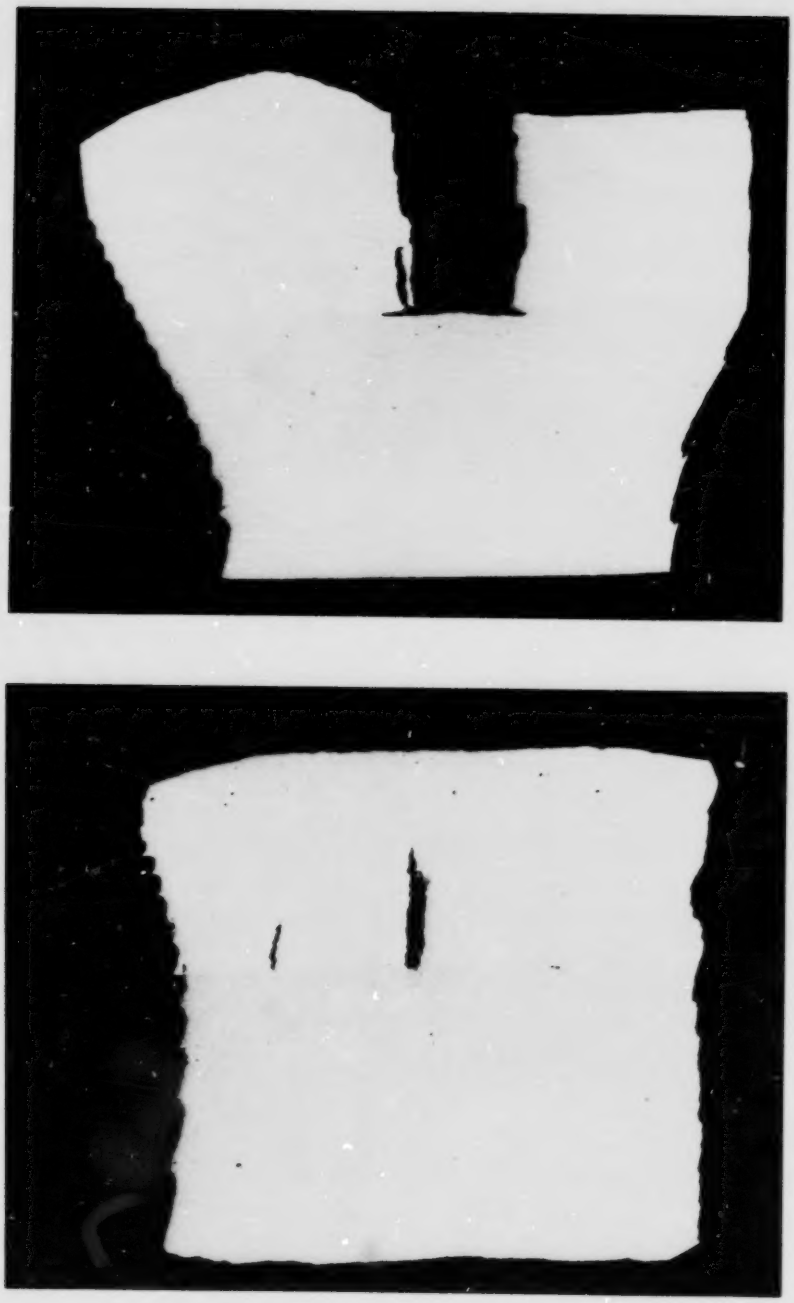

Figure 21. (a) Above, section through the centre of bend sample B1B4 showing that the crack coincided with the corner where adjacent bends overlapped (Neg. 913C, X7 mag.); (b) below, part-through cracks near the support points of B1B4 initiated near the fusion boundary and ran preferentially into the overlay (Neg. 914C, X7 mag.).

Figure 22. Detail near the crack tip of Figure 21a showing that the cracks run parallel to the fusion line within the HAZ of the Cr-Mo baseplate, Micro P34, Neg. 916C, X100 Mag.

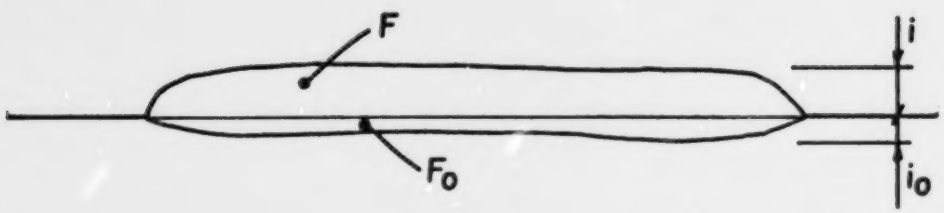

$$\text{DILUTION} = F_o / (F + F_o)$$

Figure 23. Cross-section through a strip clad specimen showing the relative contributions of electrode (F) and baseplate (Fo) to the deposit chemistry, from (25).

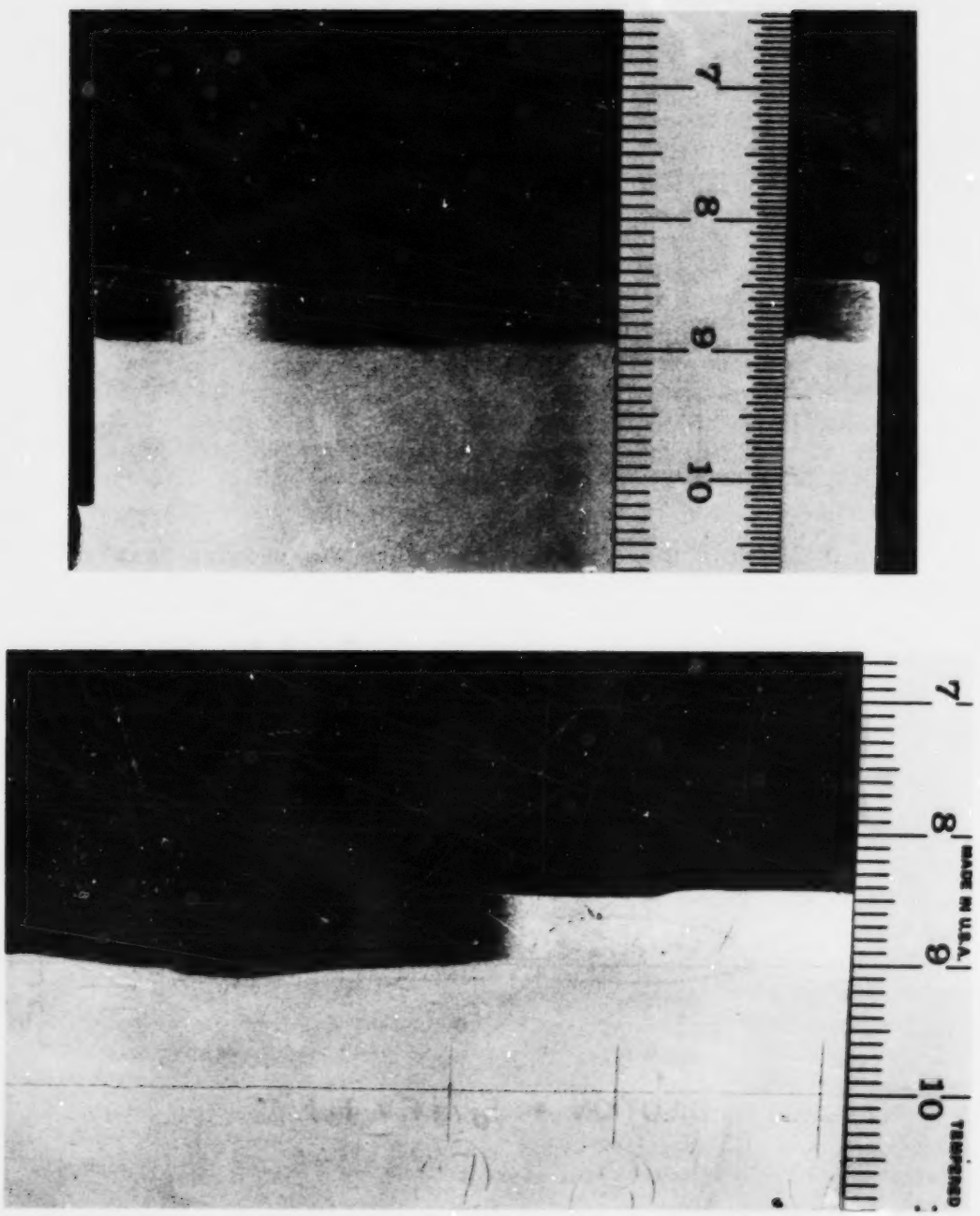

Figure 24. Sections through the overlay deposits show the 750 A overlay above to be more uniform in terms of penetration than the 1500 A overlay below (Neg CF 39).

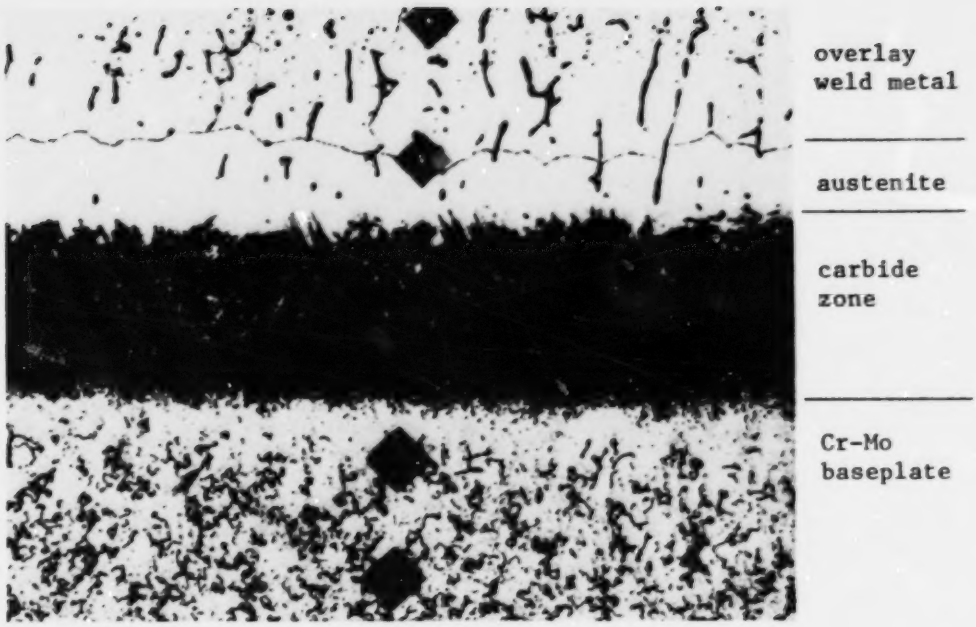

Figure 25. Example of 50 g microhardness traverse across the fusion boundary of sample E1A, Micro L3, X400 Mag., Neg. 915C.

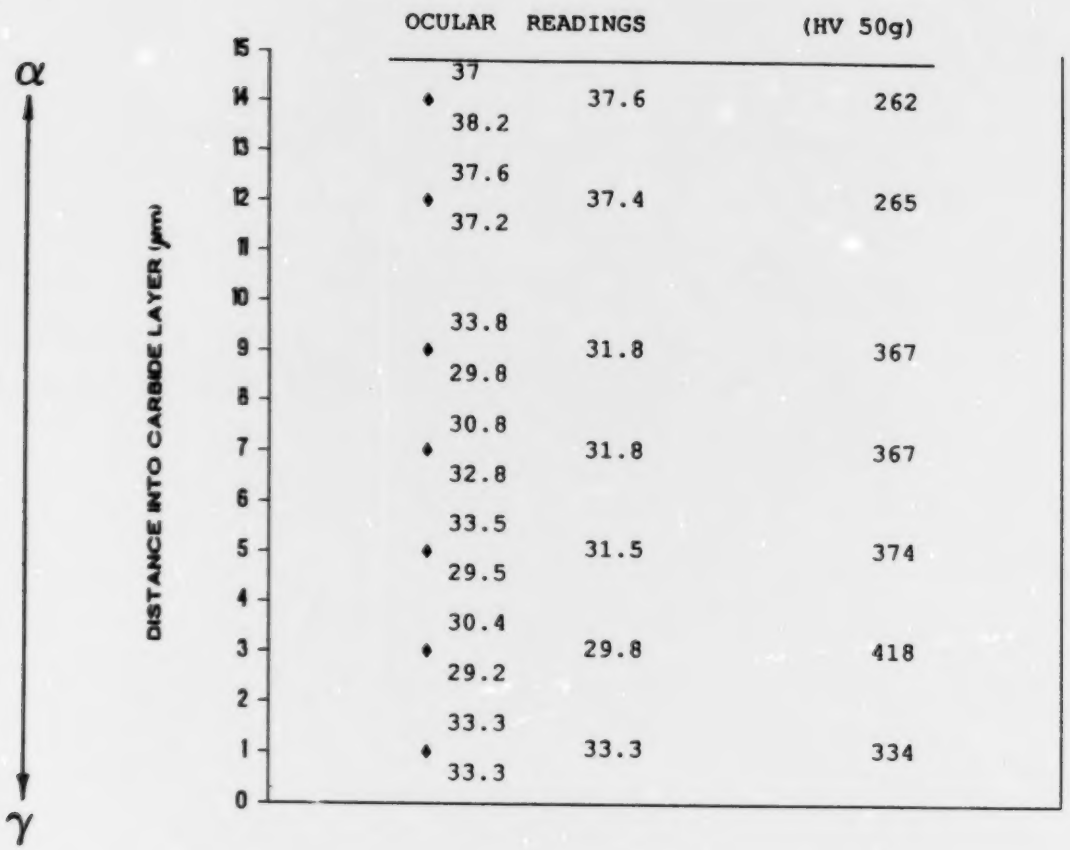

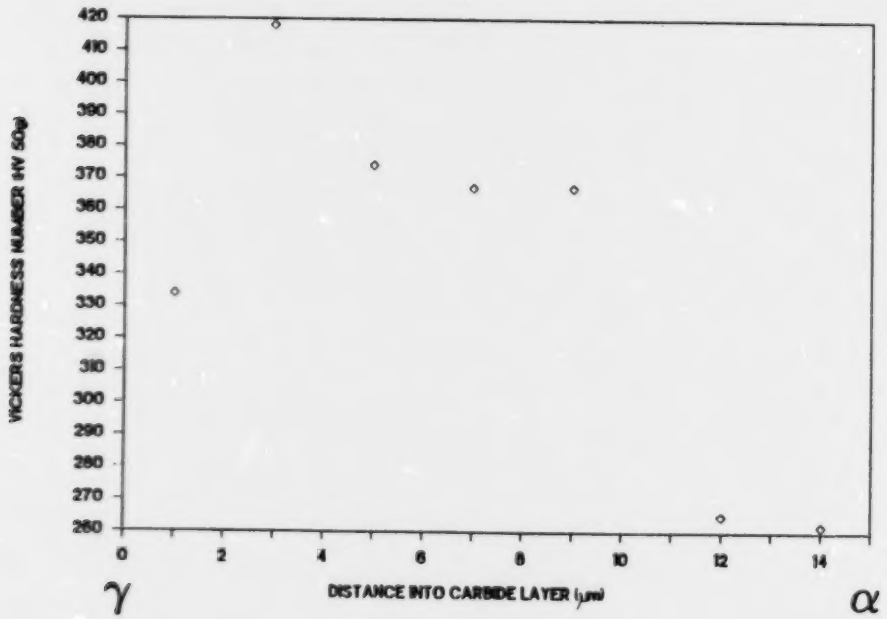

Figure 26. Microhardness profile across the carbide layer using a 50 g load. (Sample A2.2A)

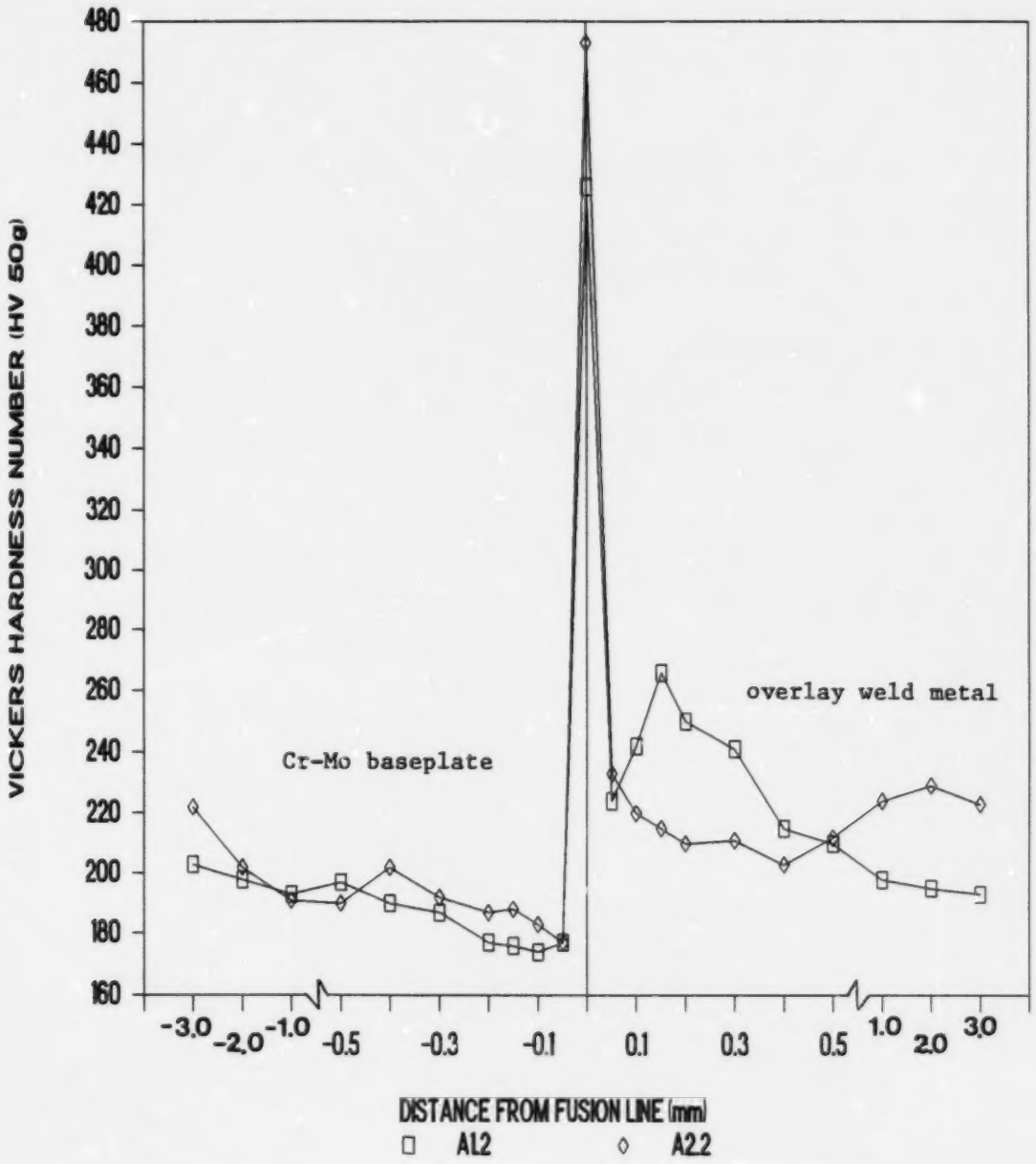

Figure 27. Hardness traverses across the fusion boundary of specimens A1.2A (750A) and A2.2A (1500 A) using a 50 g diamond pyramid indenter.

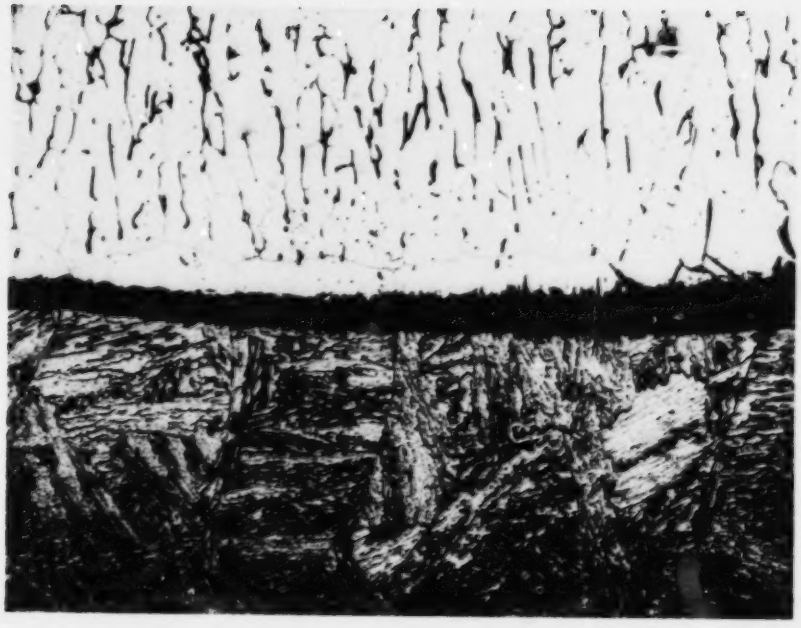

Figure 28. Fusion line between the overlay and baseplate showing tempered martensite in the narrow austenite zone and carbide precipitation in the HAZ, Neg. 941C, X200 Mag.

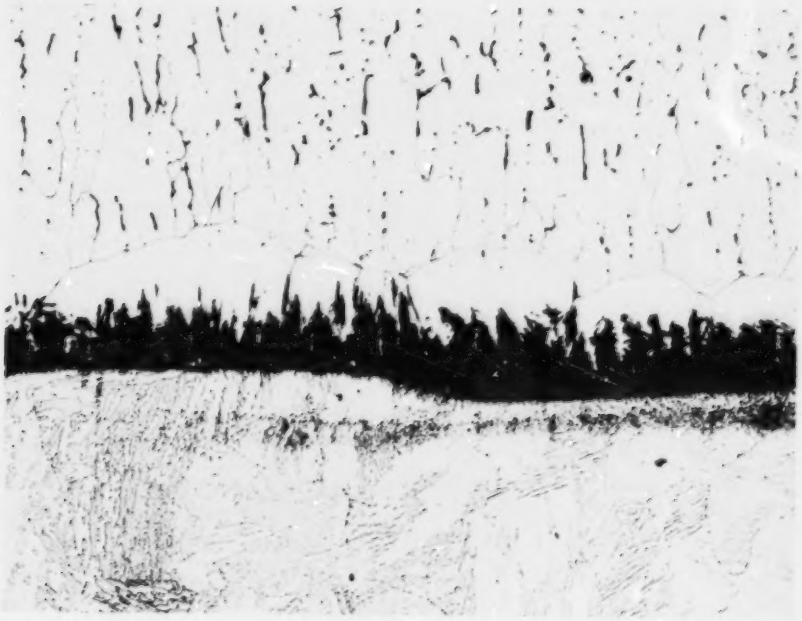

Figure 29. Fusion boundary area of overlay A1.1 showing Type II boundaries, tempered martensite, carbide precipitation in the HAZ, and prior austenite grain boundaries in HAZ extending into the overlay, Neg. 495C, X250 Mag.

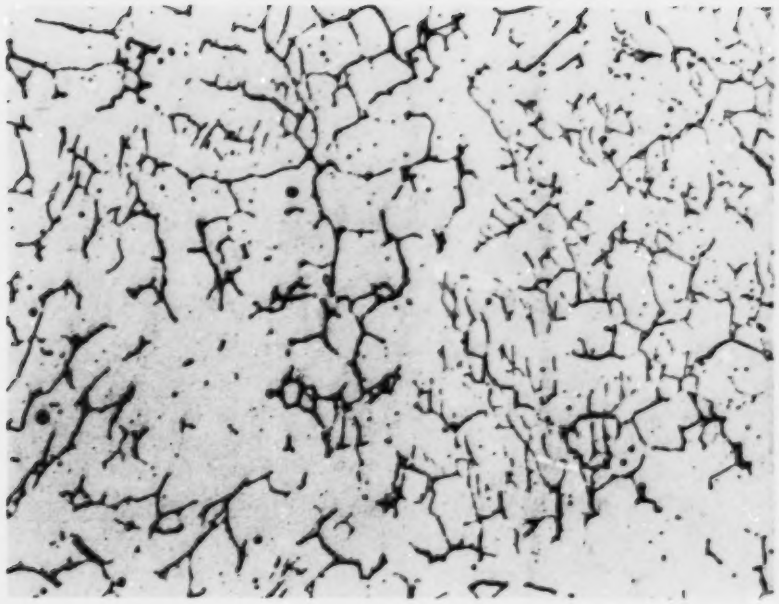

Figure 30. Microstructure of 750 A overlay deposit E1, X500 Mag., Neg. 491C.

Figure 31. Microstructure of 1500 A overlay deposit D2, X500 Mag., Neg 490C.

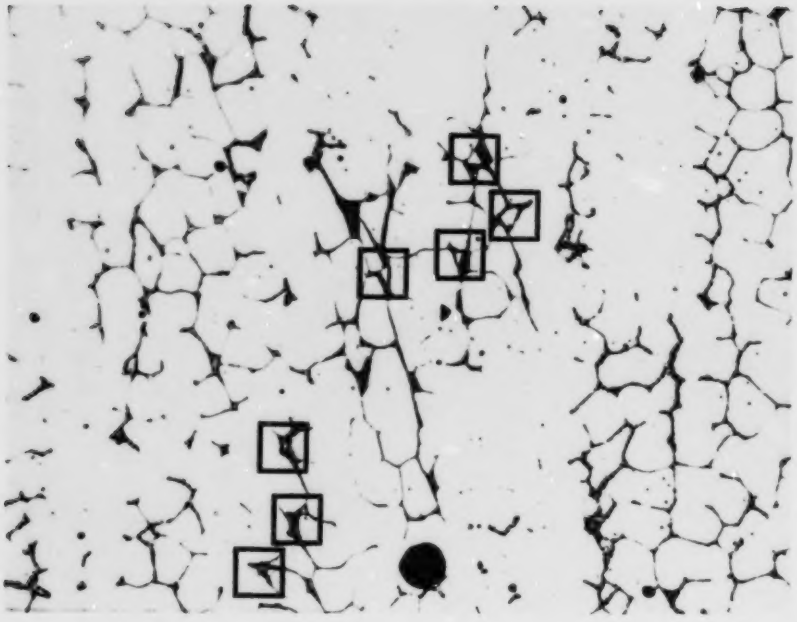

Figure 32. Overlay sample B1B shows that sigma phase has replaced some of the ferrite within the interdentritic spaces. The sigma phase (circled in figure) appears yellow when viewed directly, Neg. 918C, X500 Mag.

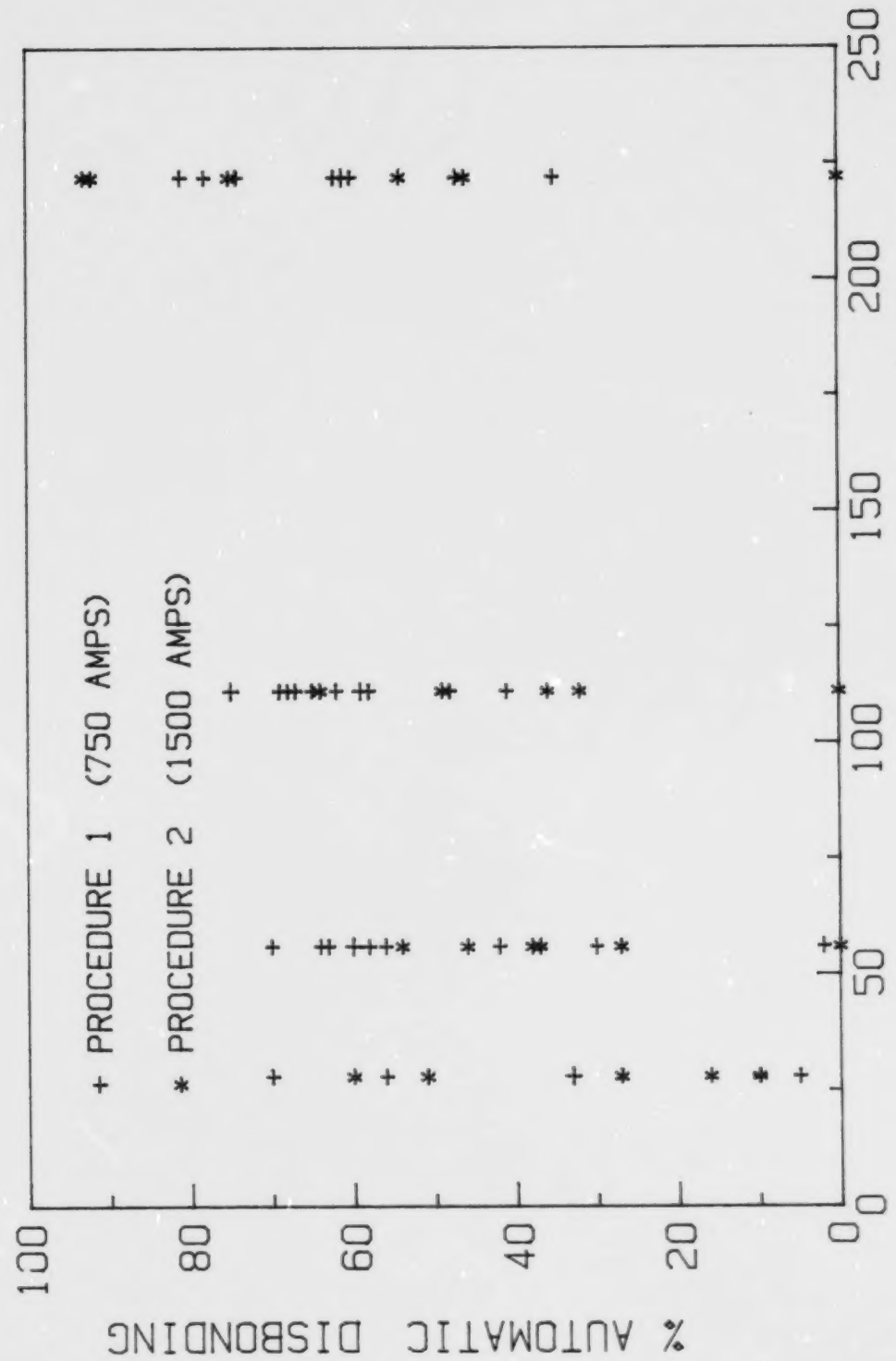

Figure 33. Summary of disbonding results after autoclave exposure.

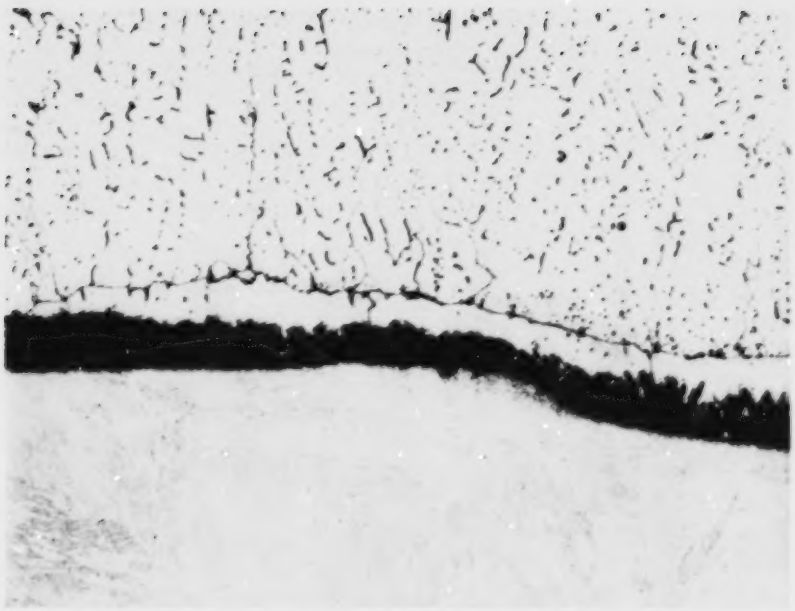

Figure 34. Cracks running along the Type II grain boundaries of specimen A1.1 after autoclave testing, Neg. 494C, X200 Mag.

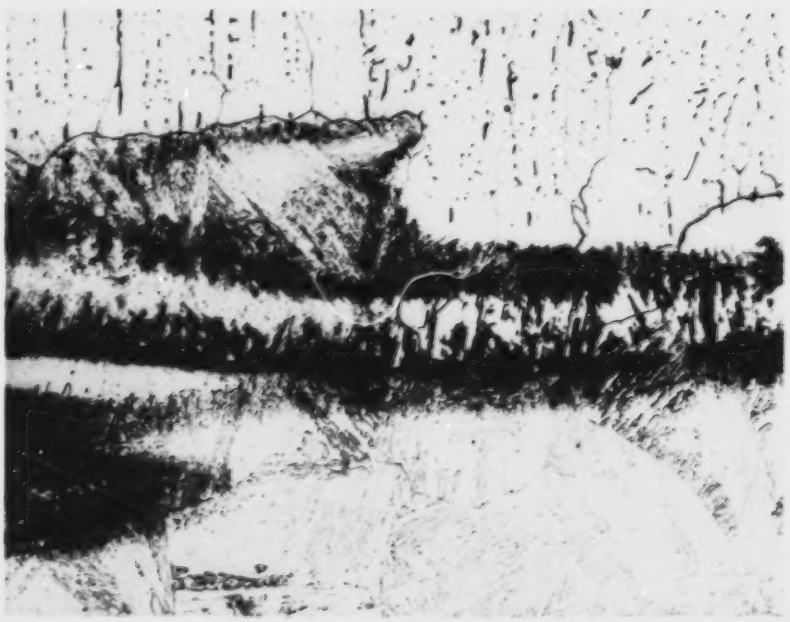

Figure 35. Cracks in the transition region of specimen A1.1 after autoclave testing, Neg. 492C, X200 Mag.

Figure 36. Cracks in the carbon-rich layers of specimen A1.1 after autoclave testing, X200 Mag., Neg. 493C.

Figure 37. Examples of cracking associated with 180°C bend tests of clad samples from (18).

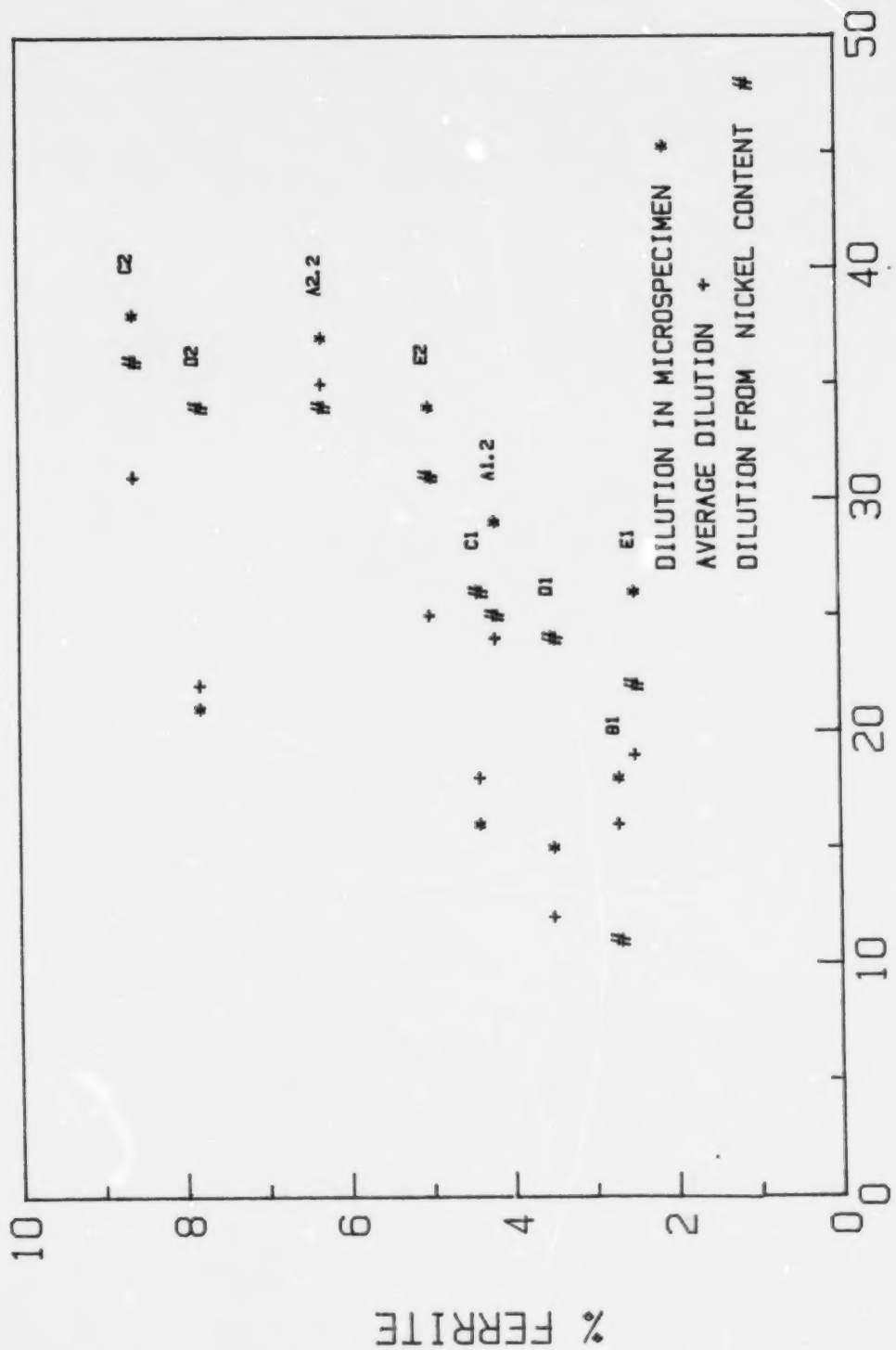

Figure 38. Ferrite number versus dilution (calculated from Ni content) for all overlays.

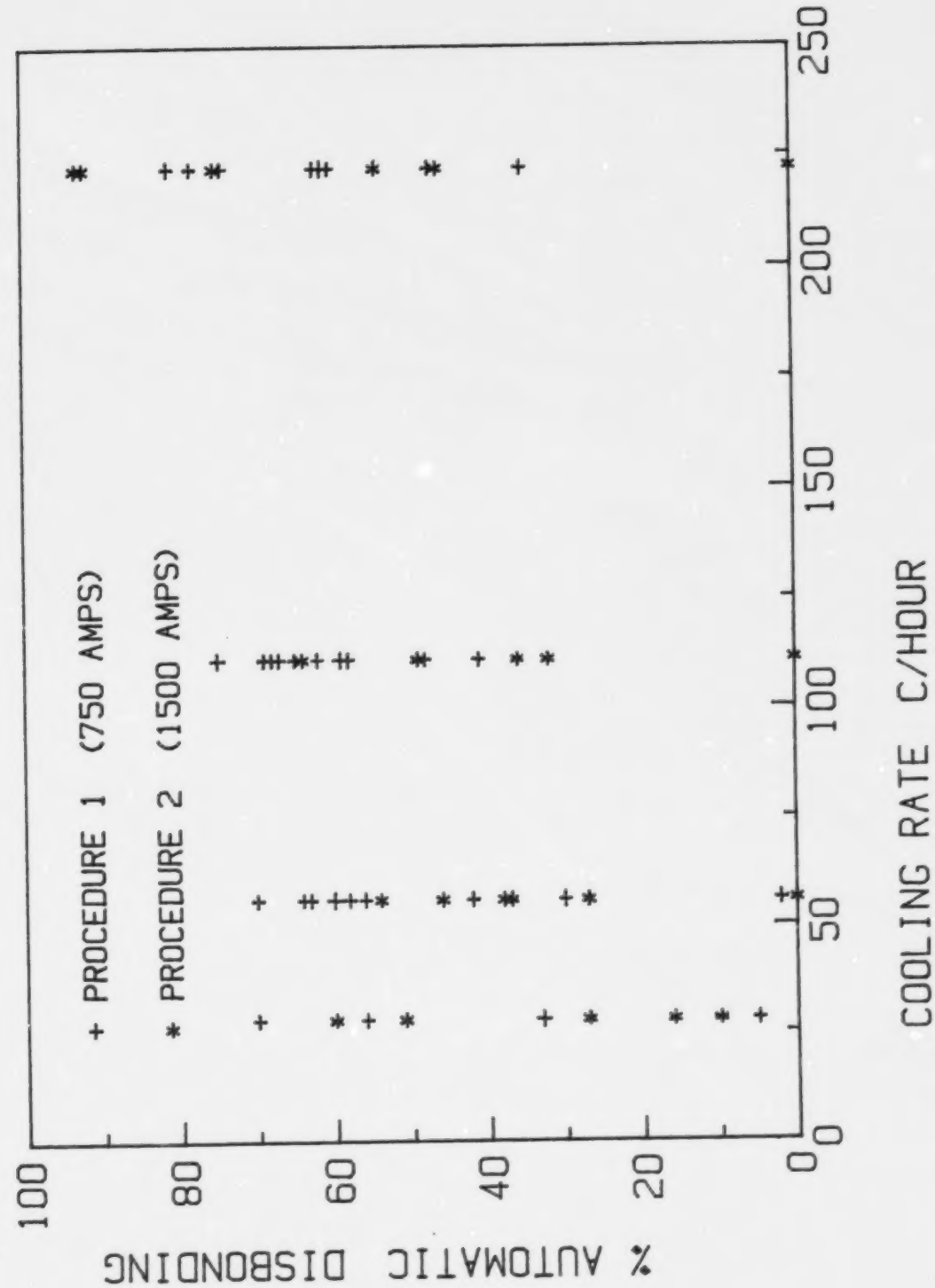

Figure 39. Disbonding percentage versus cooling rate for autoclave specimens.

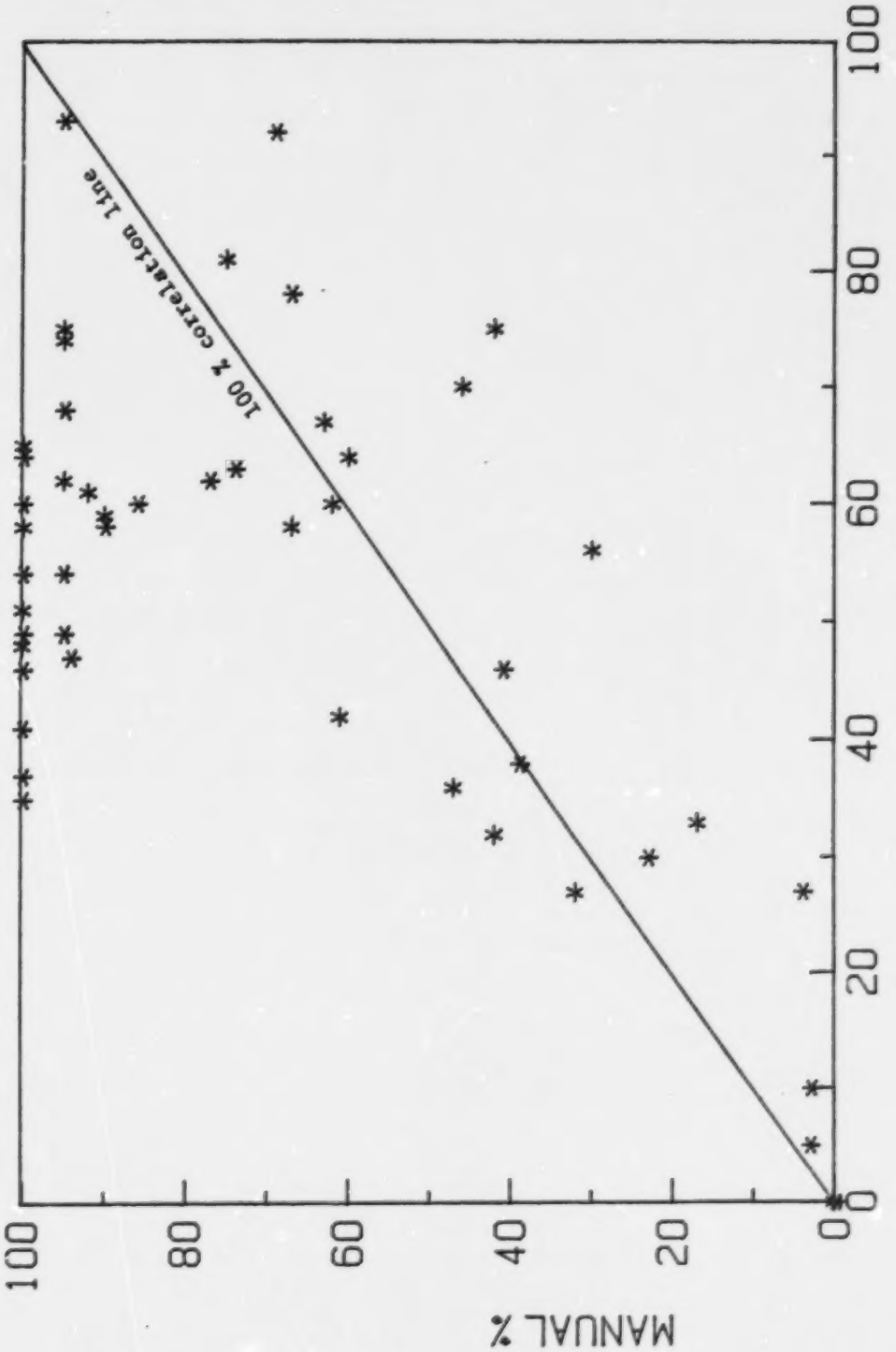

Figure 40. Manual ultrasonic versus automated ultrasonic C-scan inspection results from autoclave test specimens.

APPENDIX A

Autoclave Test Procedures

Autoclave Test Specimen Indentification

Autoclave Batch Number	Cooling Rate °C/h	Specimen Number
1	222	A2-1A1, C1A5, C2A1
2	222	D1A5, D2A1, E2A1
3	111	A1-2A5, A2-1A2, B1A5
4	111	C1A6, C2A2, D1A6
5	111	D2A2, E1A5, E2A2
6	56	A1-2A6, A2-1A3, B1A6
7	56	C2A3, D2A3, E2A3
8	28	A2-2A4, C2A4, D2A4
9	28	E1A6, E2A4
10	222	C1A7, E2A6
11	111	C1A8, E2A7
12	56	C1A9, E2A8
13	222	F1A1
14	111	F1A2
15	56	F1A3
16	56	A1-1A3, D1A3, E1A3
17	111	A1-1A2, D1A2, E1A2
18	28	A1-2A4, D1A4, E1A4
19	222	A1-1A1, D1A1, E1A1
20	28/56	B1A3, C1A3, D2A5
21	56	B1A4, C1A4, E2A5
22	111	A2-2A5, B1A2, C1A2
23	222	B1A1, C1A1, C2A5

TEST GAS H2: BATCHES 1, 2, 13.

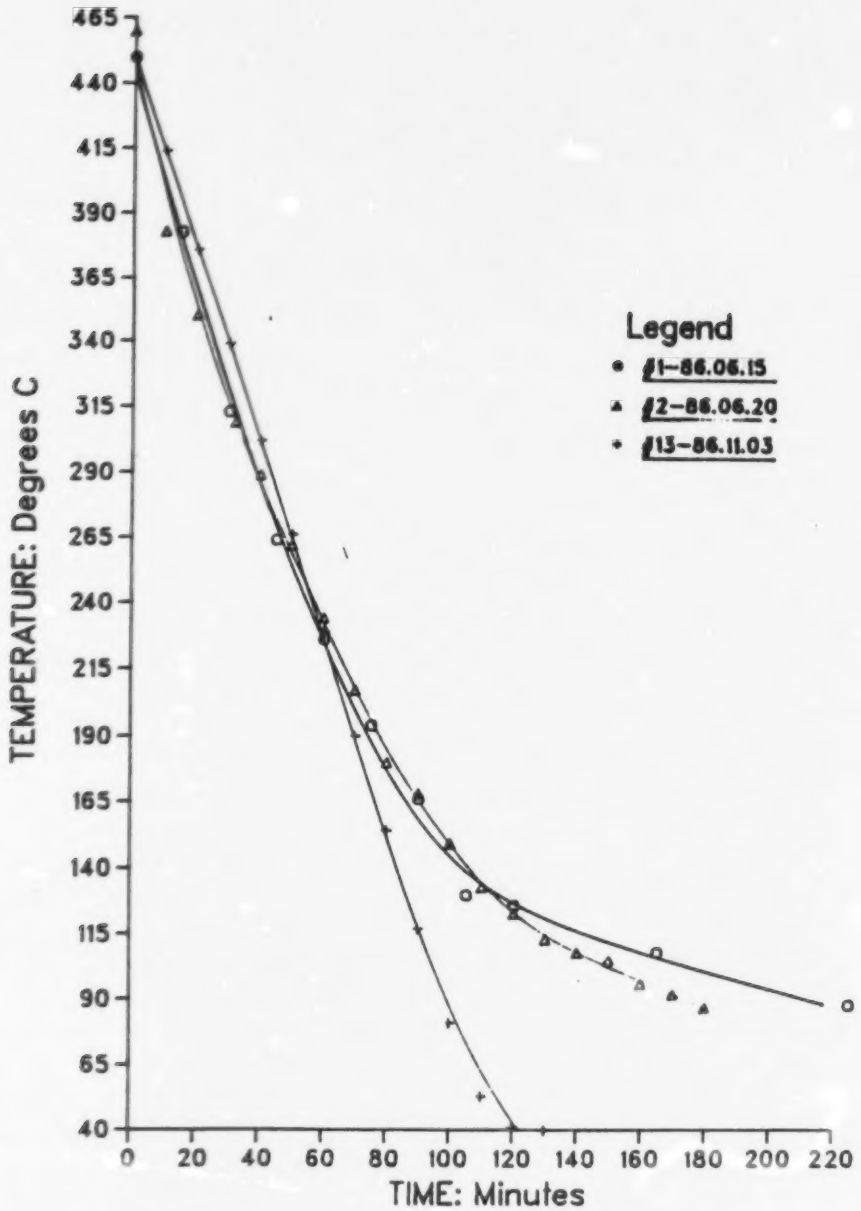

TEST GAS H2: BATCHES 3, 4, 5, 14.

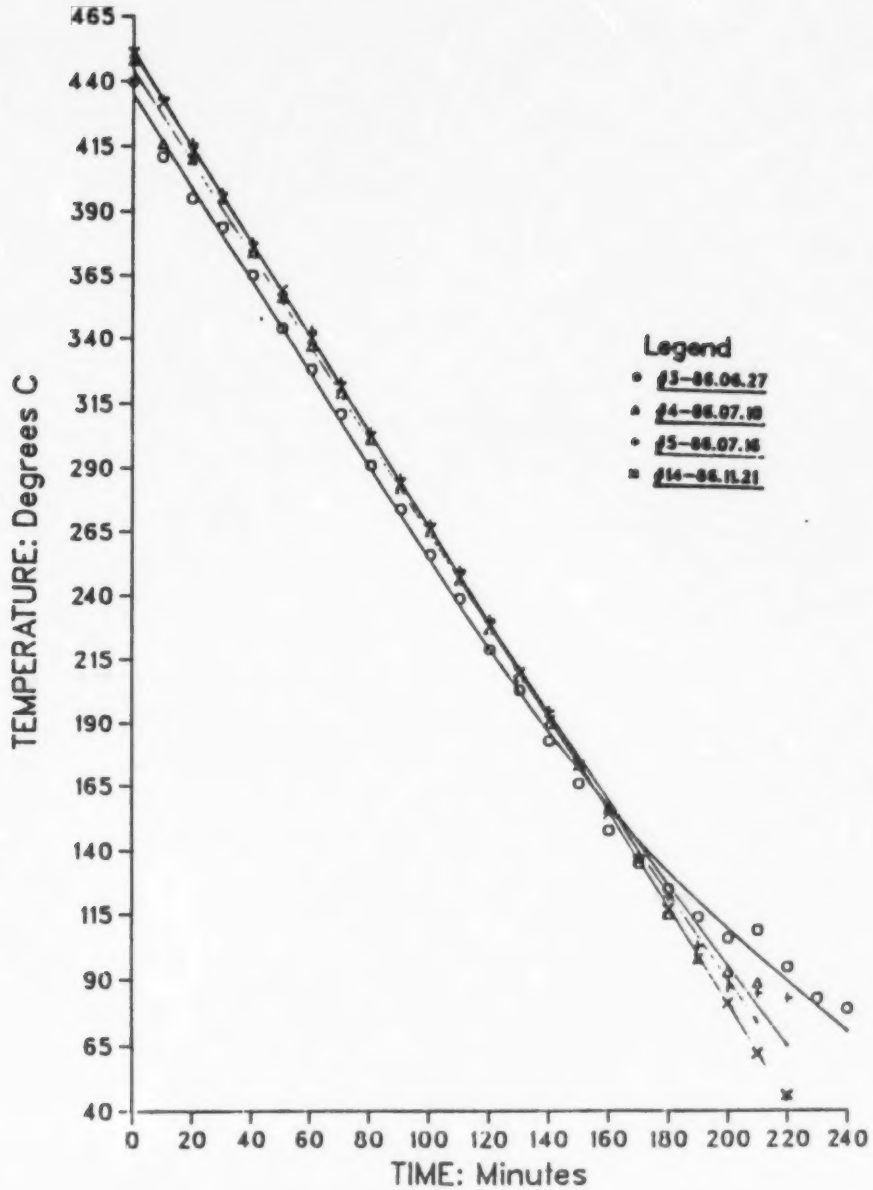

TEST GAS H2: BATCHES 6, 7, 15.

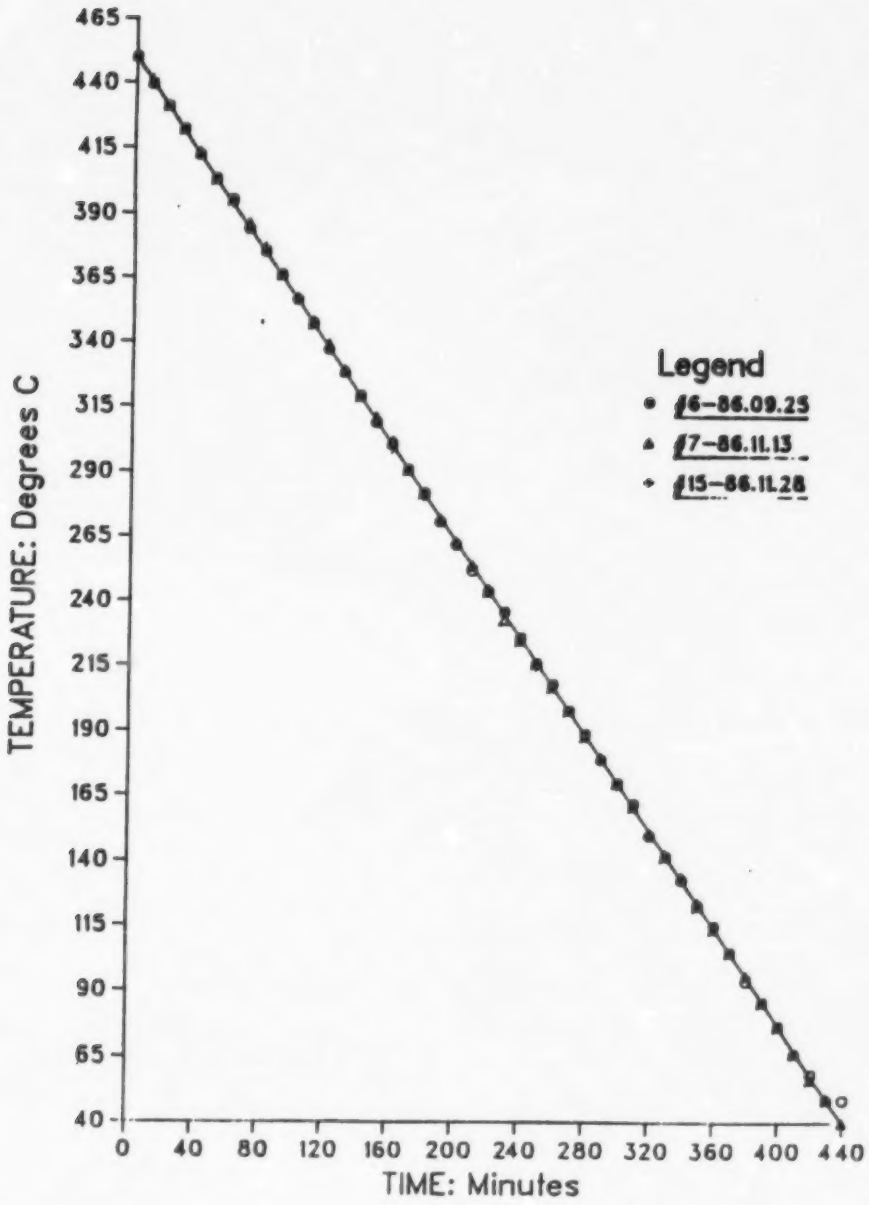

TEST GAS H2: BATCHES 8, 9.

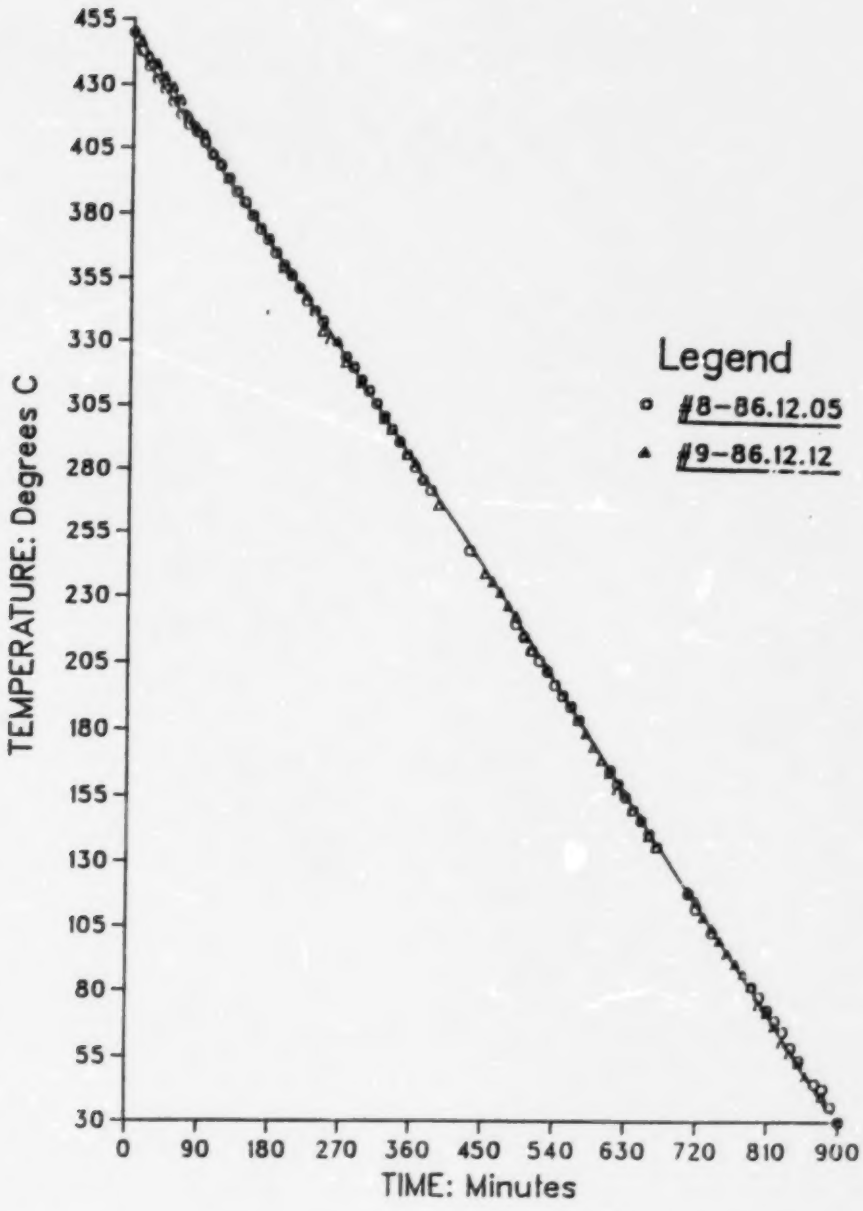

TEST GAS N2: BATCHES 10, 11, 12.

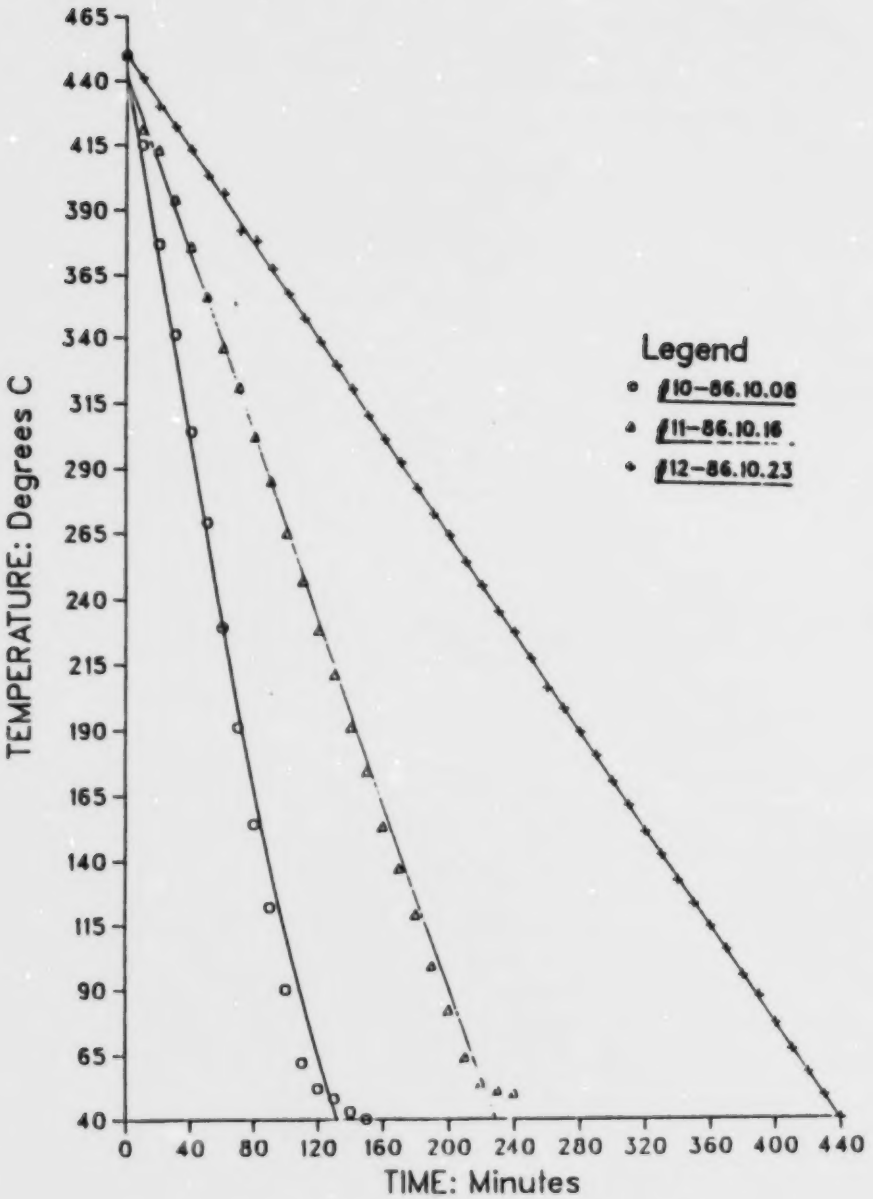

APPENDIX B

Summary of Manual UT Results

Weld Procedure A1

A1.1A1
E

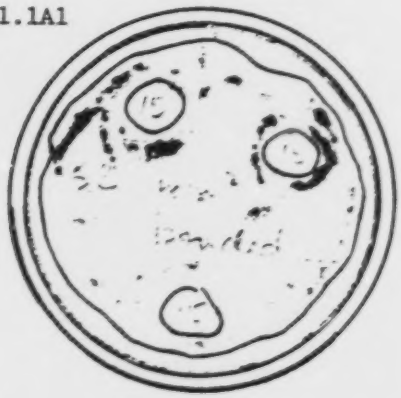

A1.1A2
E

A1.1A3
E

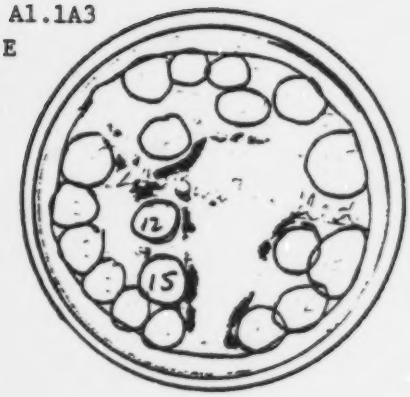

A1.2A4
E

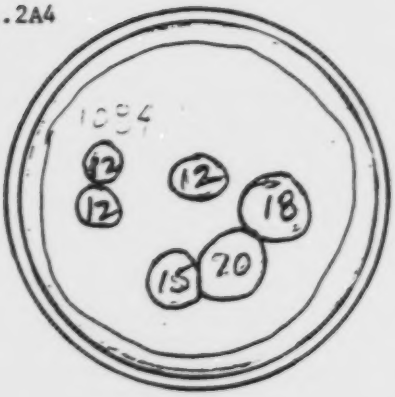

A1.2A5
A

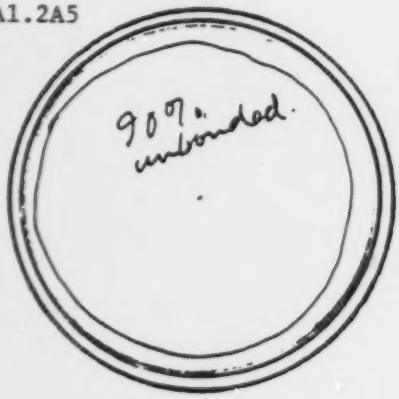

A1.2A6
A

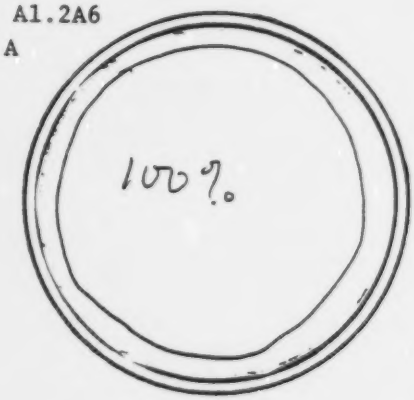

Specimen	Cooling Rate C/hr	Percentage Disbonded
A1.1A1	222	92
A1.1A2	111	95
A1.1A3	56	62
A1.2A4	28	17
A1.2A5	111	90
A1.2A6	56	100

Weld Procedure B1

B1A1
E

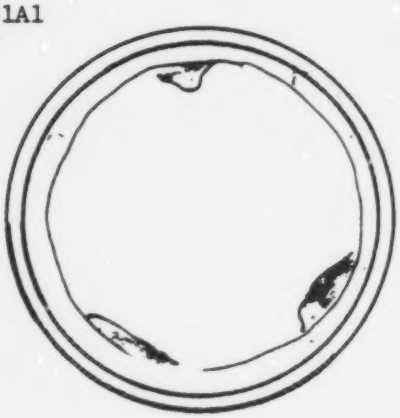

B1A2
E

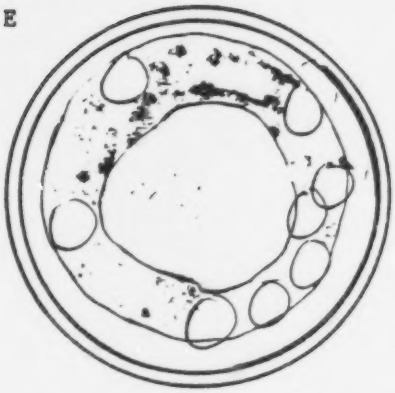

B1A3
E

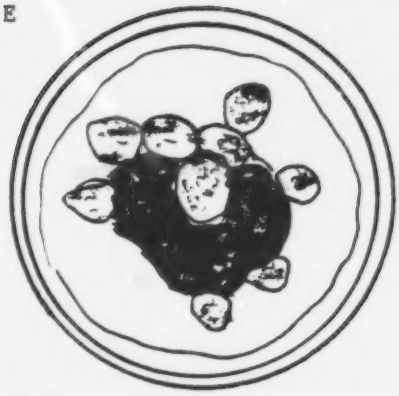

B1A4
E

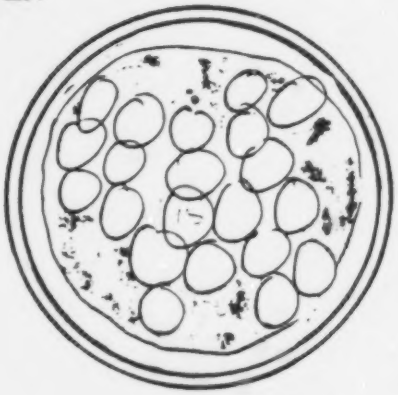

B1A5
A

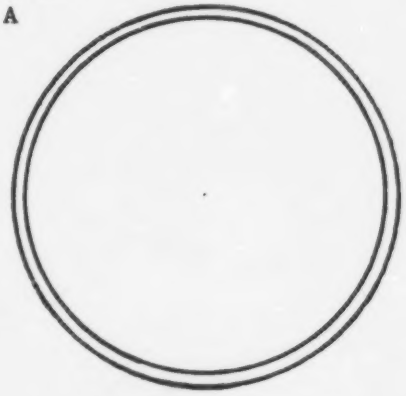

B1A6
A

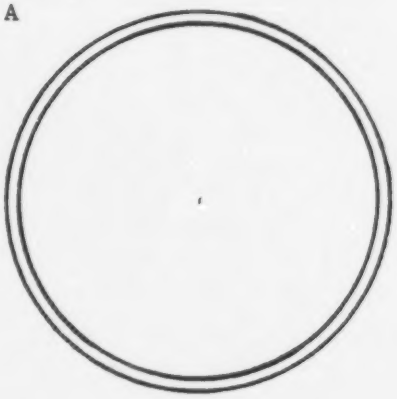

Specimen	Cooling Rate C/hr	Percentage Disbonding
B1A1	222	95
B1A2	111	67
B1A3		30
B1A4	56	61
B1A5	111	100
B1A6	56	100

Weld Procedure C1

C1A1
E

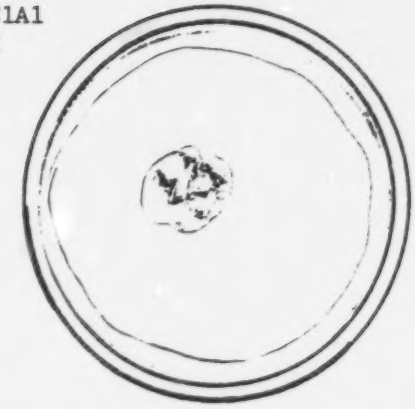

C1A2
E

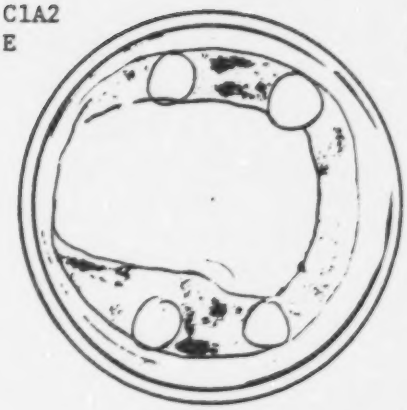

C1A3
E

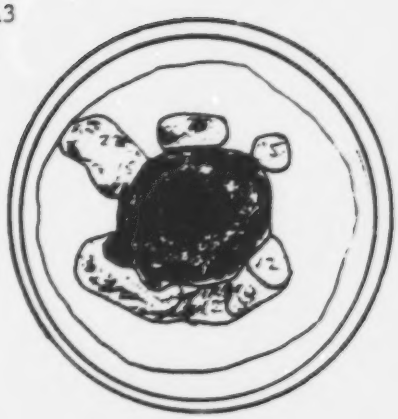

C1A4
E

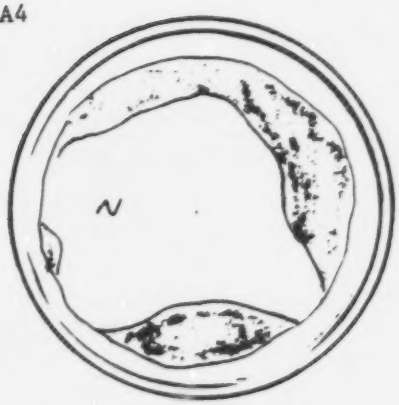

C1A5
A

C1A6
A

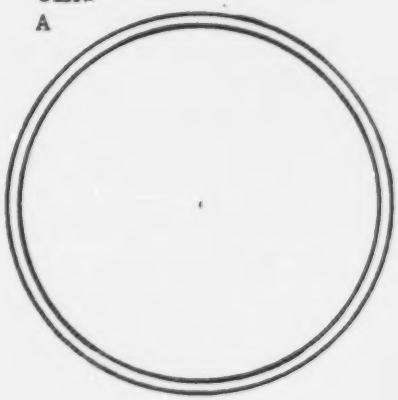

Specimen	Cooling Rate C/hr	Percentage Disbonded
C1A1	222	95
C1A2	111	63
C1A3		46
C1A4	56	60
C1A5	222	75
C1A6	111	100

Weld Procedure D1

D1A1
E

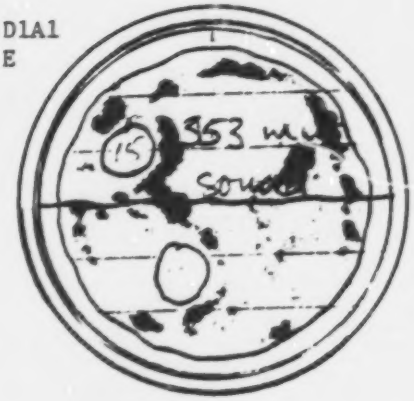

D1A2
E

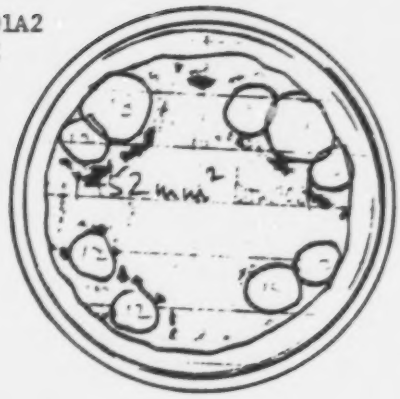

D1A3
E

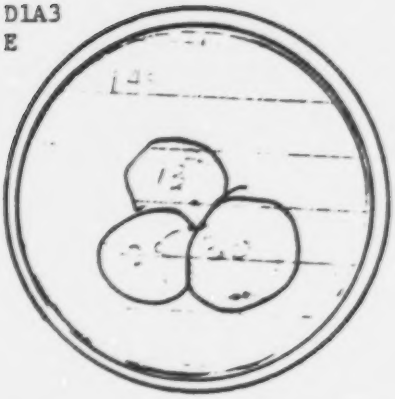

D1A4
E

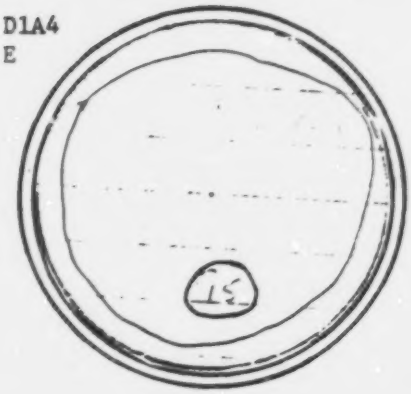

D1A5
A

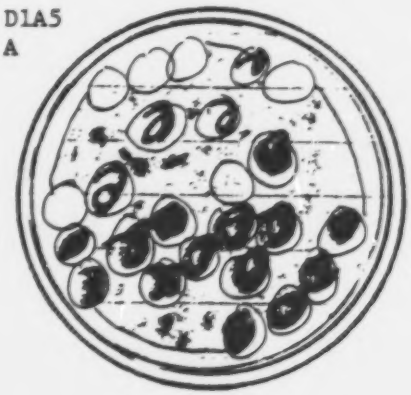

D1A6
A

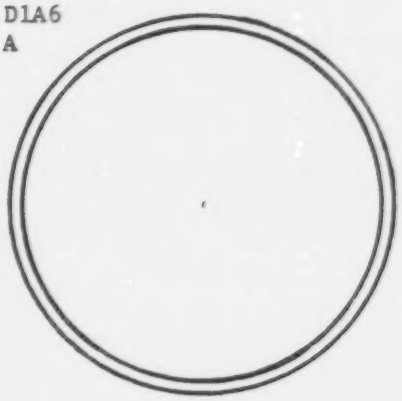

Specimen	Cooling Rate C/hr	Percentage Disbonded
D1A1	222	94
D1A2	111	77
D1A3	56	23
D1A4	28	3
D1A5	222	67
D1A6	111	100

Weld Procedure E1

E1A1
E

E1A2
E

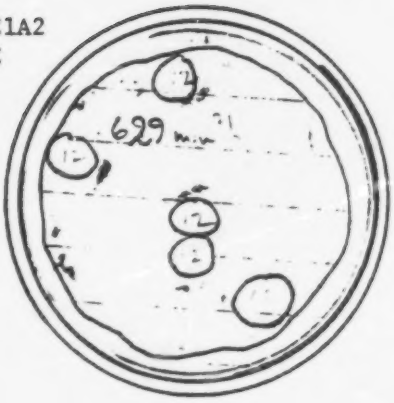

E1A3
E

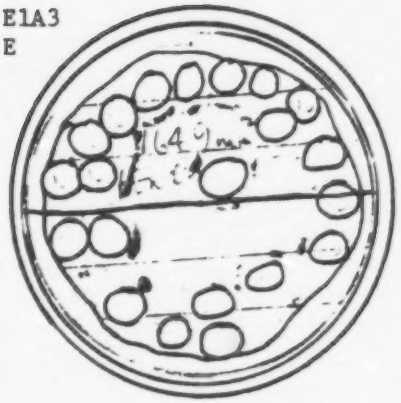

E1A4
E

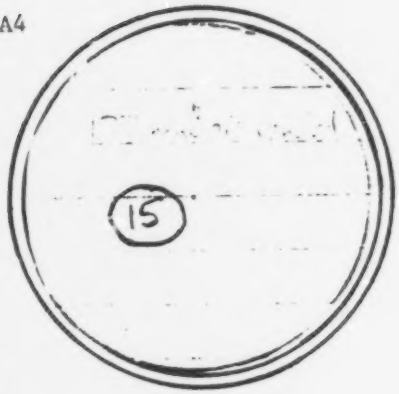

E1A5
A

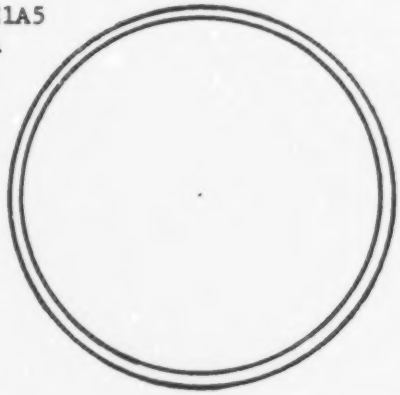

E1A6
A

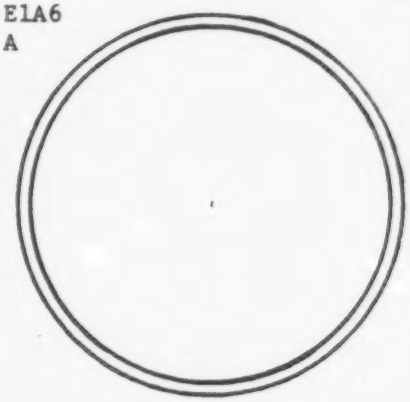

Specimen	Cooling Rate C/hr	Percentage Disbonded
E1A1	222	86
E1A2	111	90
E1A3	56	74
E1A4	28	3
E1A5	111	95

Weld Procedure A2

A2.1A1
A

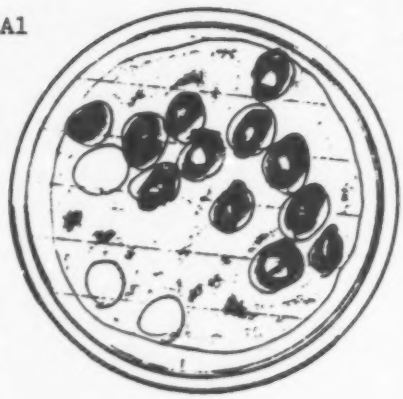

A2.1A2
A

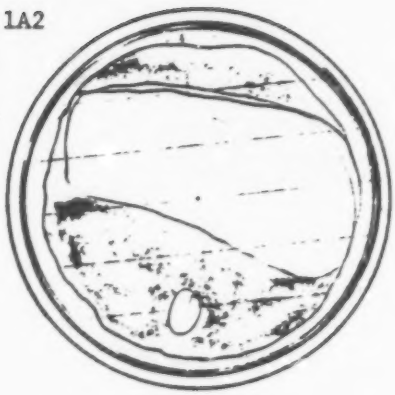

A2.1A3
A

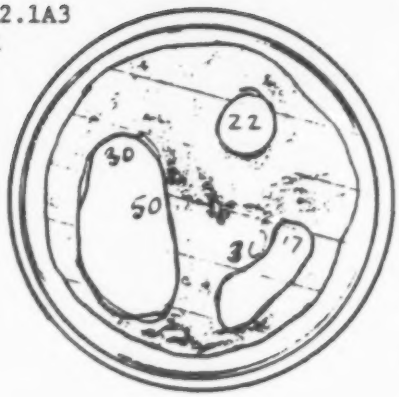

A2.2A4
A

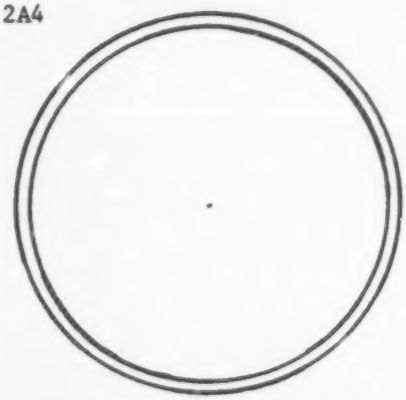

A2.2A5
E

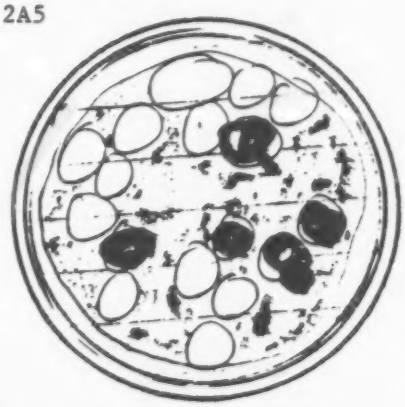

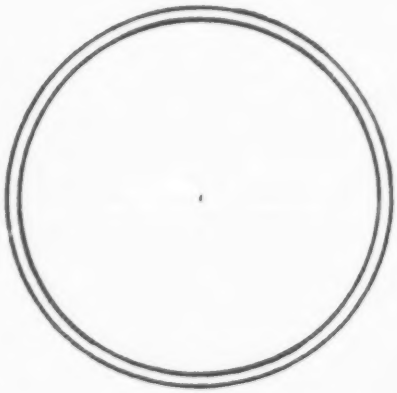

Specimen	Cooling Rate C/hr	Percentage Disbonded
A2.1A1	222	42
A2.1A2	111	42
A2.1A3	56	32
A2.2A5	111	47

Weld Procedure C2

C2A1
A

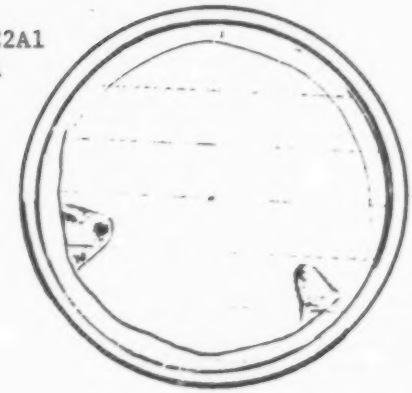

C2A2
A

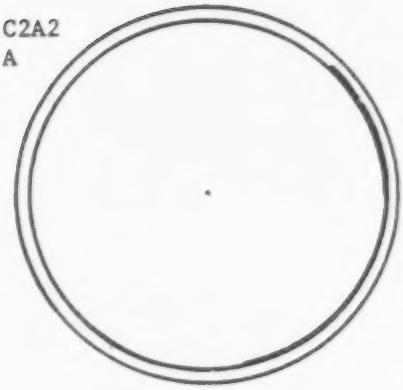

C2A3
A

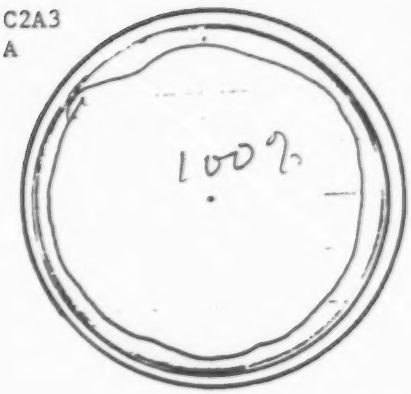

C2A4
A

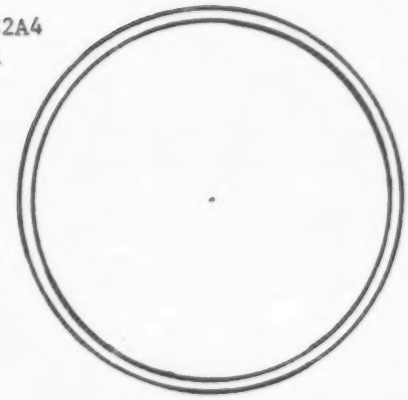

C2A5
E

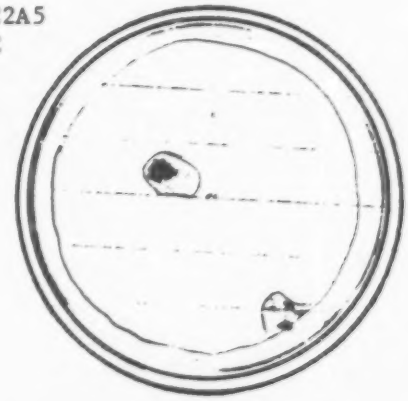

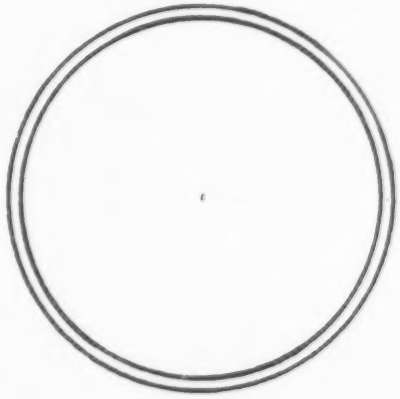

Specimen	Cooling Rate C/hr	Percentage Disbonded
C2A1	222	95
C2A2	111	100
C2A3	56	100
C2A5	222	95

Weld Procedure D2

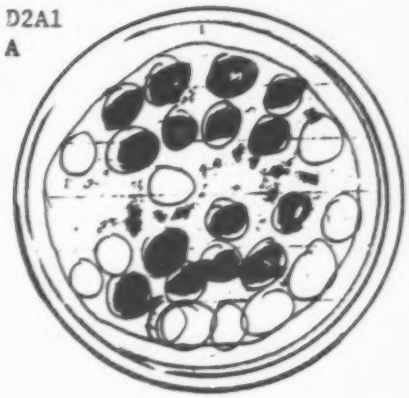

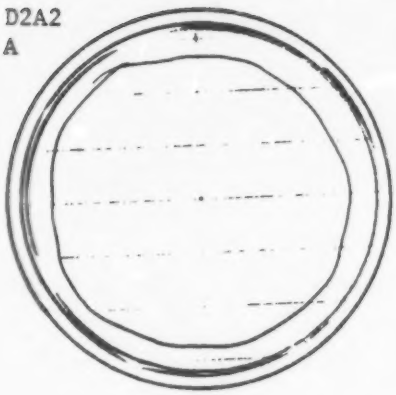

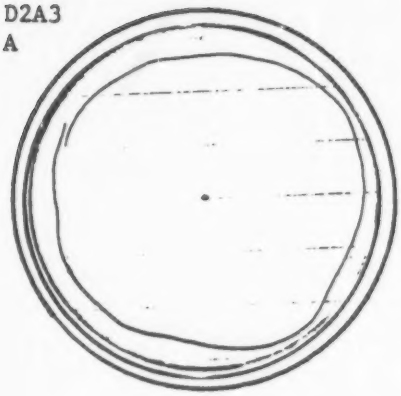

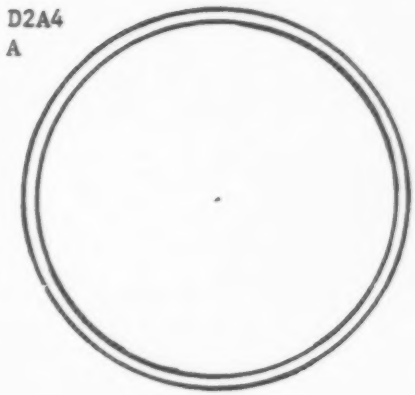

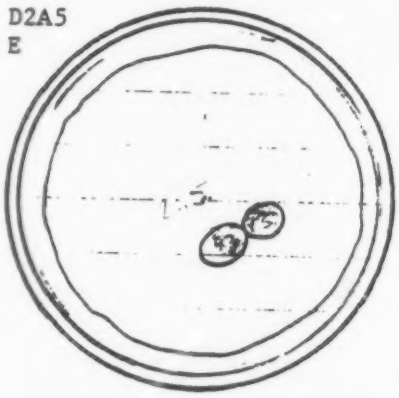

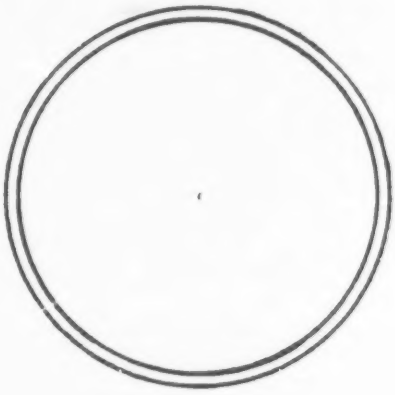

Specimen	Cooling Rate C/hr	Percentage Disbonded
D2A1	222	69
D2A2	111	100
D2A3	56	100
D2A5	28/56	4

Weld Procedure E2

E2A1A
A

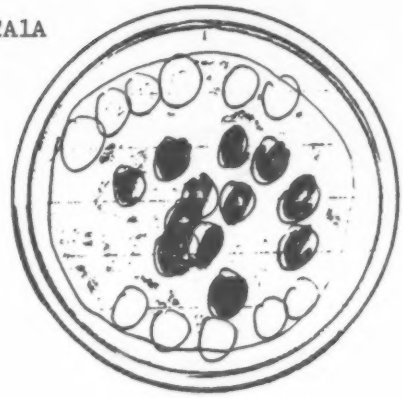

E2A2A
A

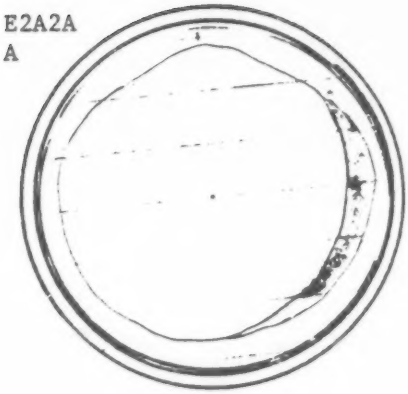

E2A3
A

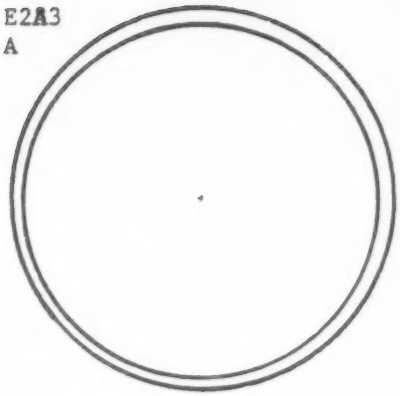

E2A4
A

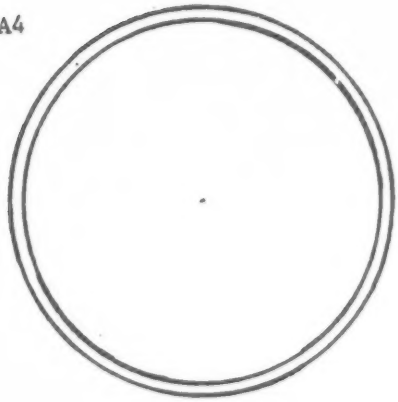

E2A5
E

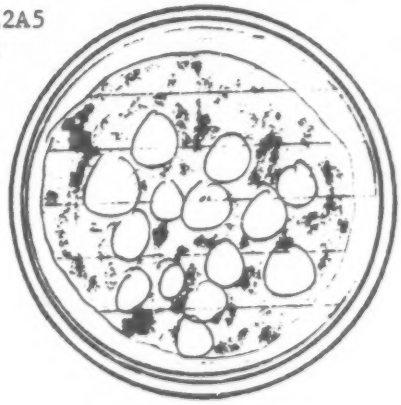

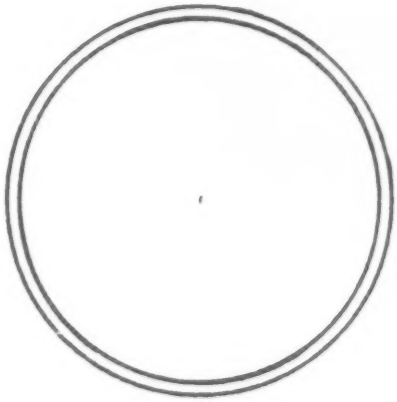

Specimen	Cooling Rate C/hr	Percentage Disbonded
E2A1	222	41
E2A2	111	95
E2A3	56	100
E2A5	56	39

APPENDIX C

Summary of Automated UT Results

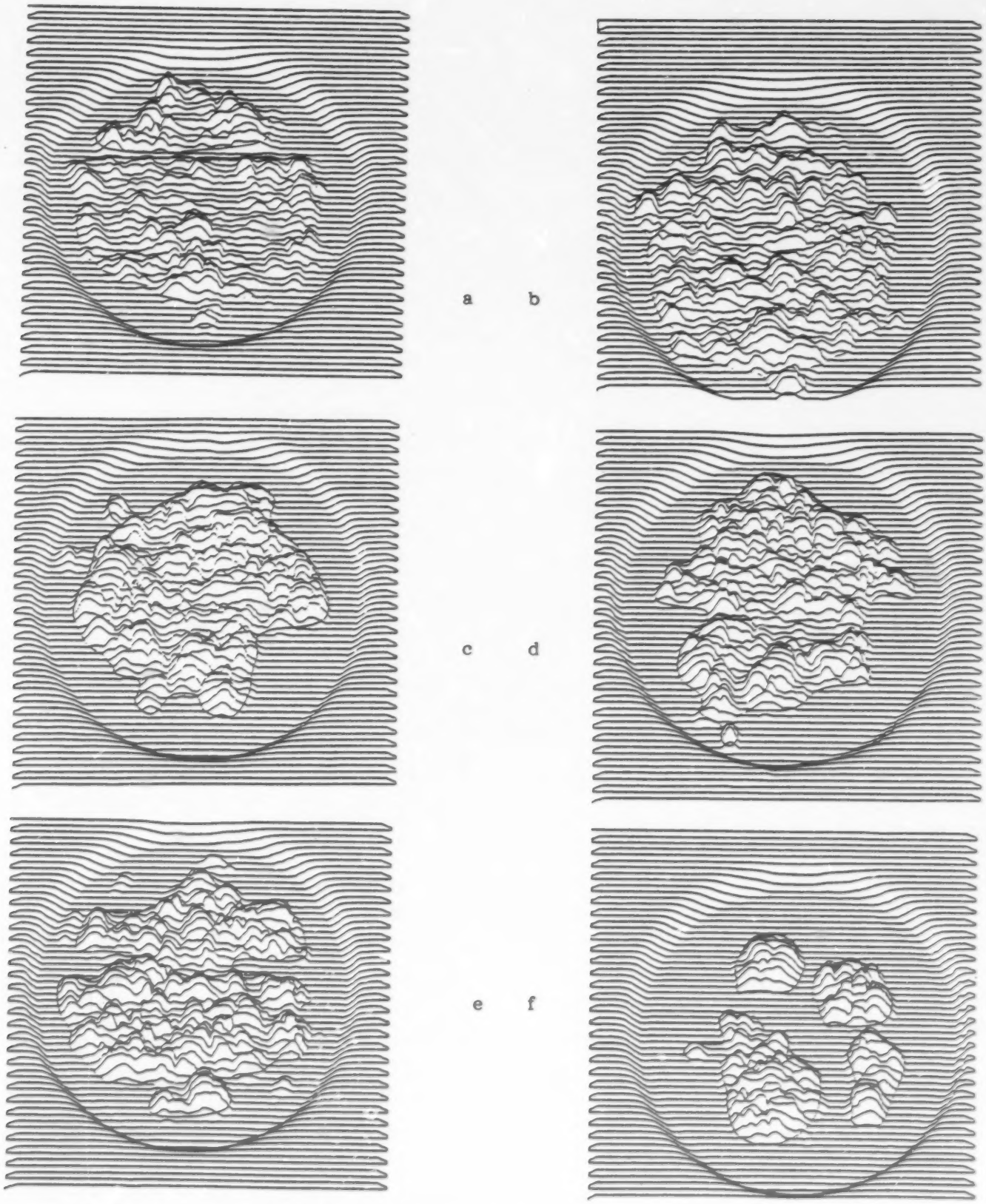

Figure C1. Pseudo-C-scan plots of autoclave samples (a) A1.1A1 (222°C/h), (b) A1.1A2 (111°C/h), (c) A1.2A5 (111°C/h), (d) A1.1A3 (56°C/h), (e) A1.2A6 (56°C/H), and (f) A1.2A4 (28°C/h).

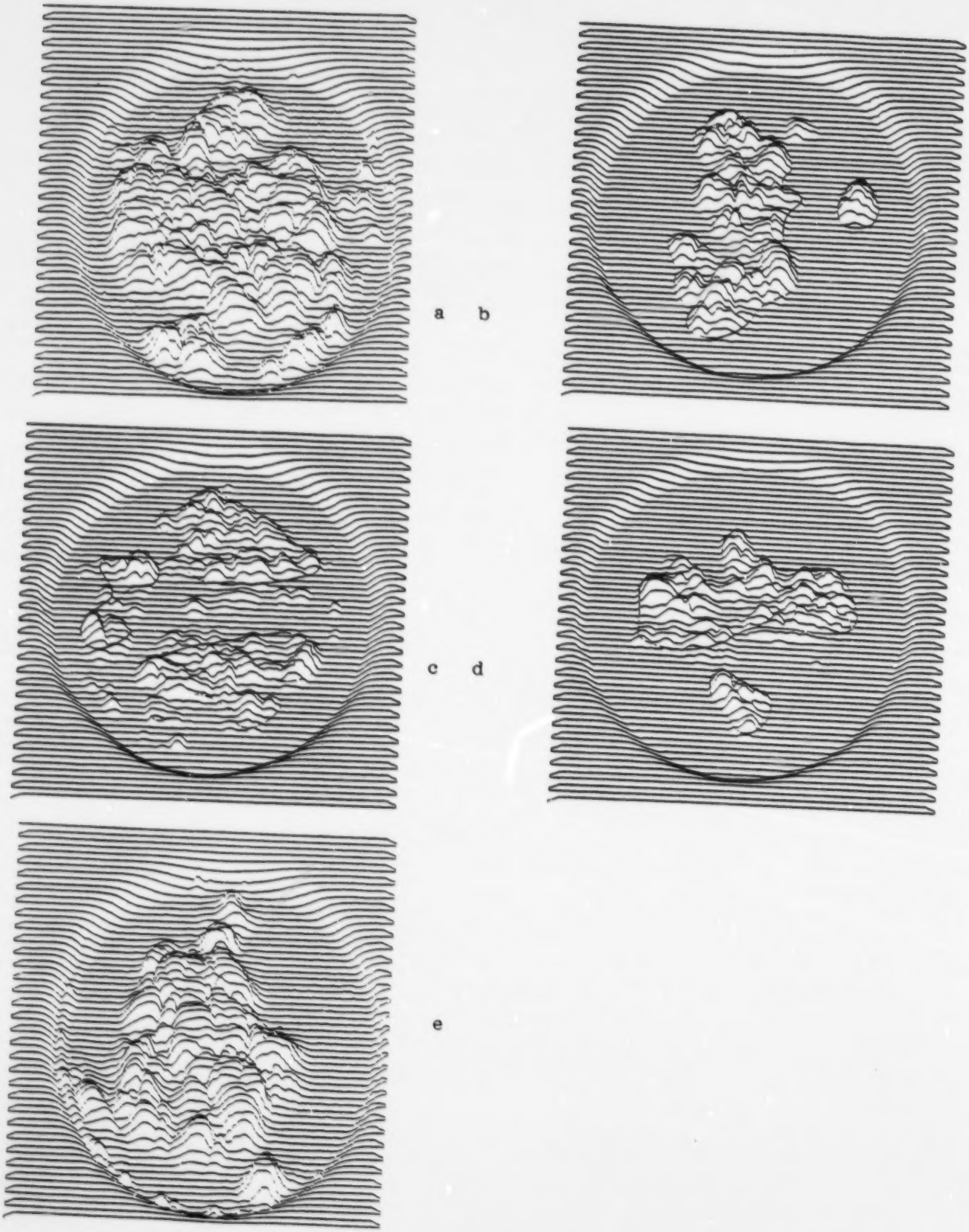

Figure C2. Pseudo-C-scan plots of autoclave samples (a) A2.1A1 (222°C/h), (b) A2.1A2 (111°C/h), (c) A2.1A5 (111°C/h), (d) A2.1A3 (56°C/h), and (e) A2.2A4 (56°C/h).

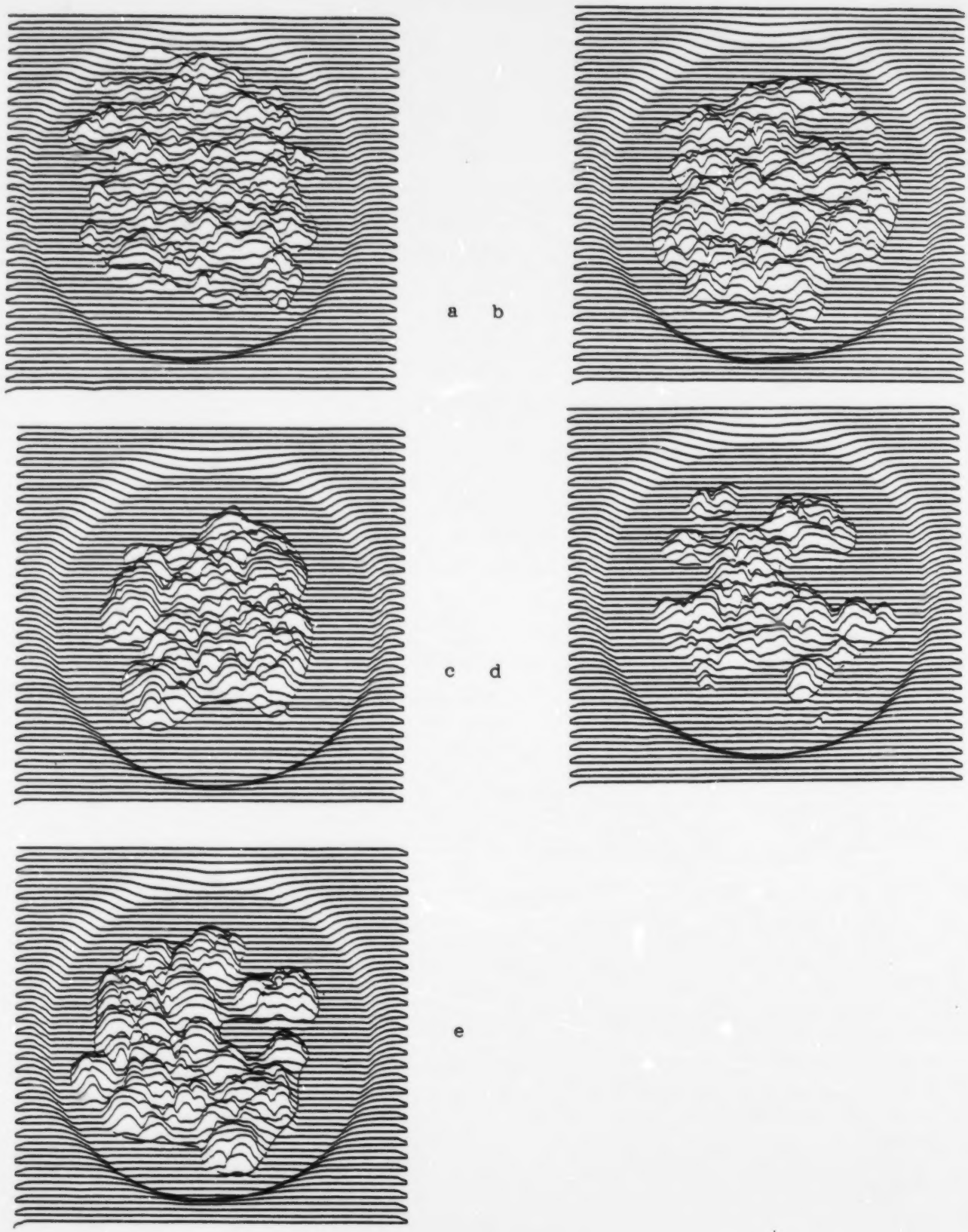

Figure C3. Pseudo-C-scan plots of autoclave samples (a) B1A1 (222°C/h), (b) B1A2 (111°C/h), (c) B1A5 (111°C/h), (d) B1A4 (56°C/h), and (e) B1A6 (56°C/h).

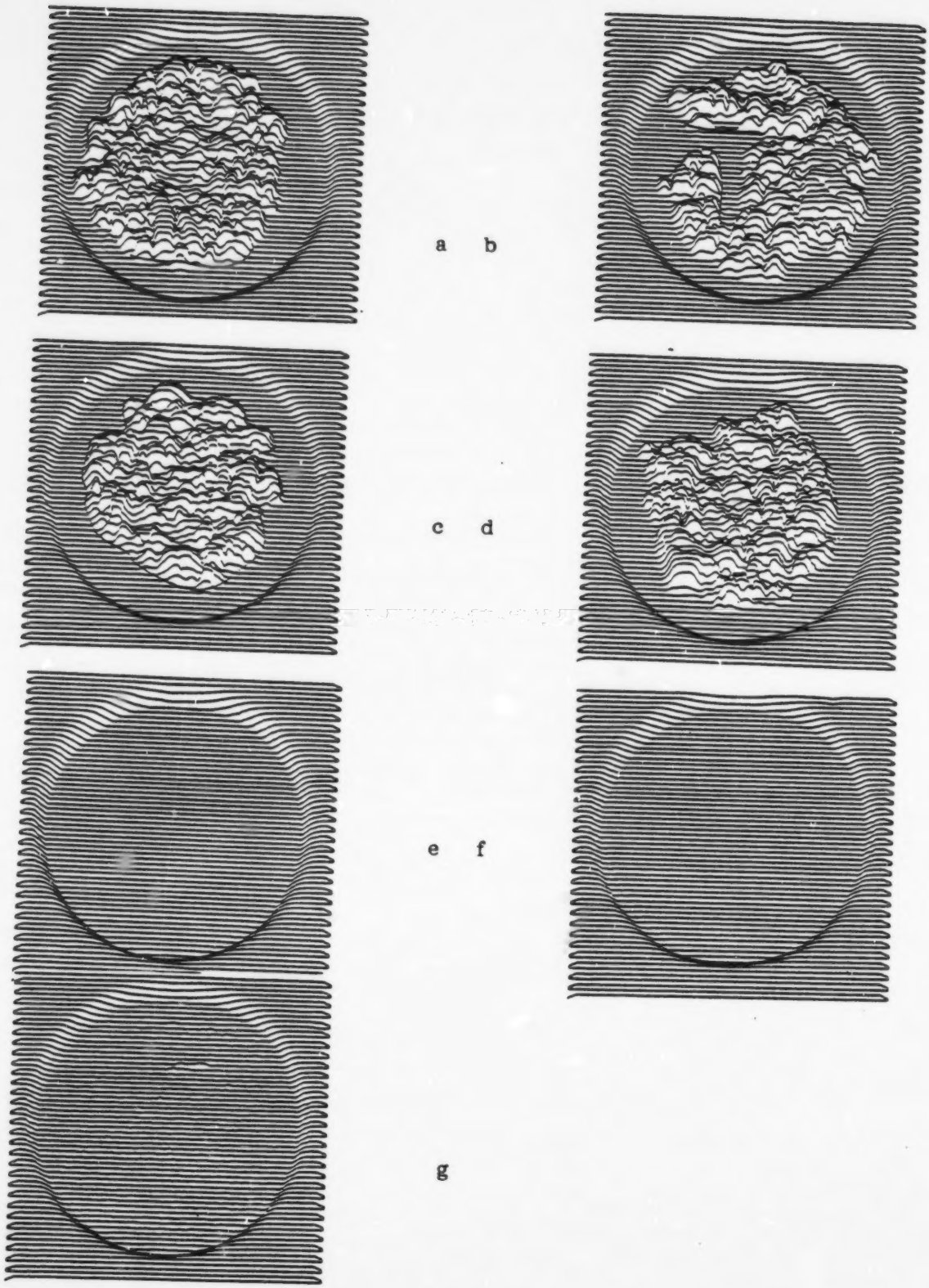

Figure C4. Pseudo-C-scan plots of autoclave samples (a) C1A1 (222°C/h), (b) C1A2 (111°C/h), (c) C1A6 (111°C/h), (d) C1A4 (56°C/h), (e) C1A7N2 (222°C/h), (f) C1A8N2 (111°C/h), and (g) C1A9N2 (56°C/h).

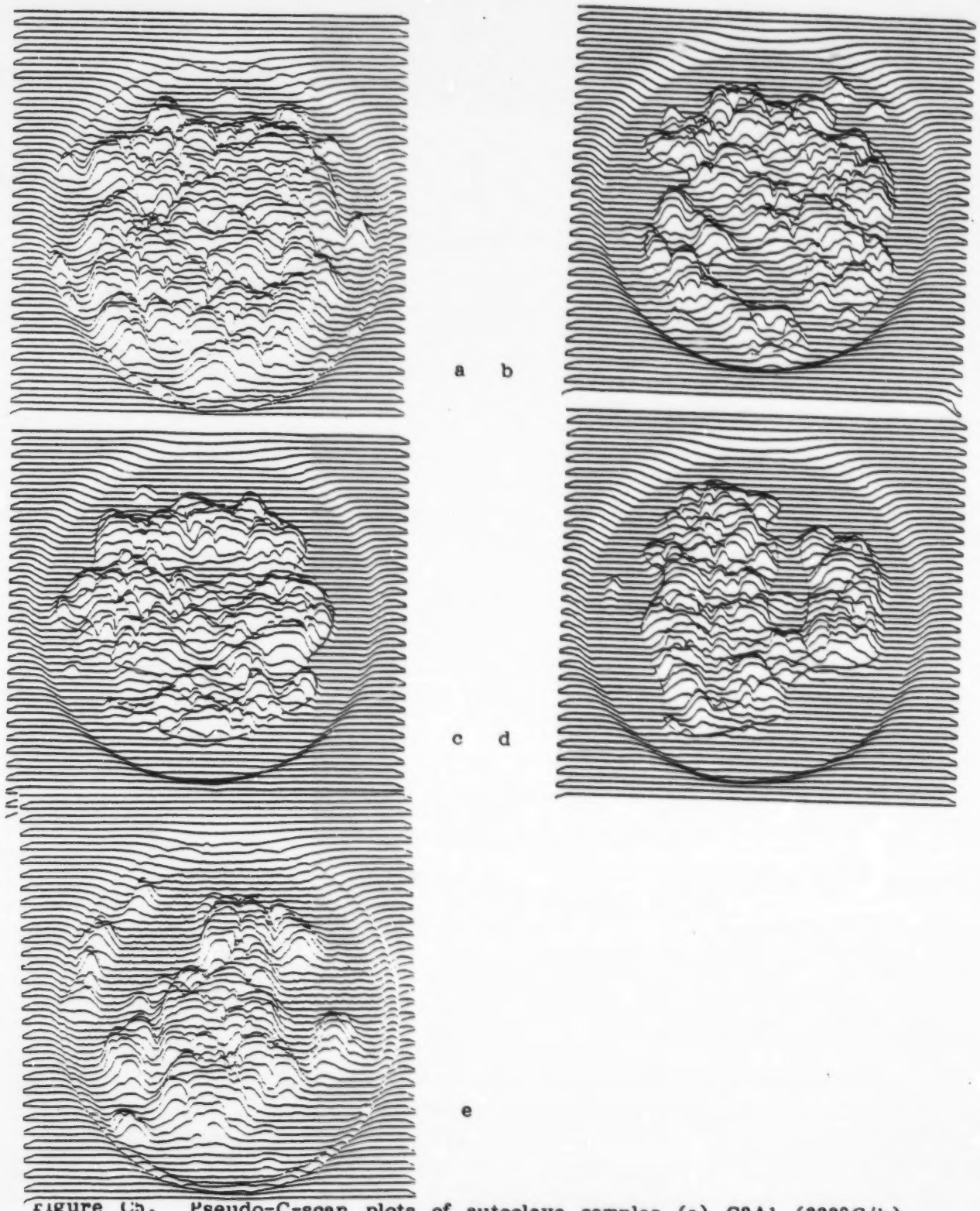

Figure C5. Pseudo-C-scan plots of autoclave samples (a) C2A1 (222°C/h), (b) C2A5 (222°C/h), (c) C2A2 (111°C/h), (d) C2A3 (56°C/h), and (e) C2A4 (28°C/h).

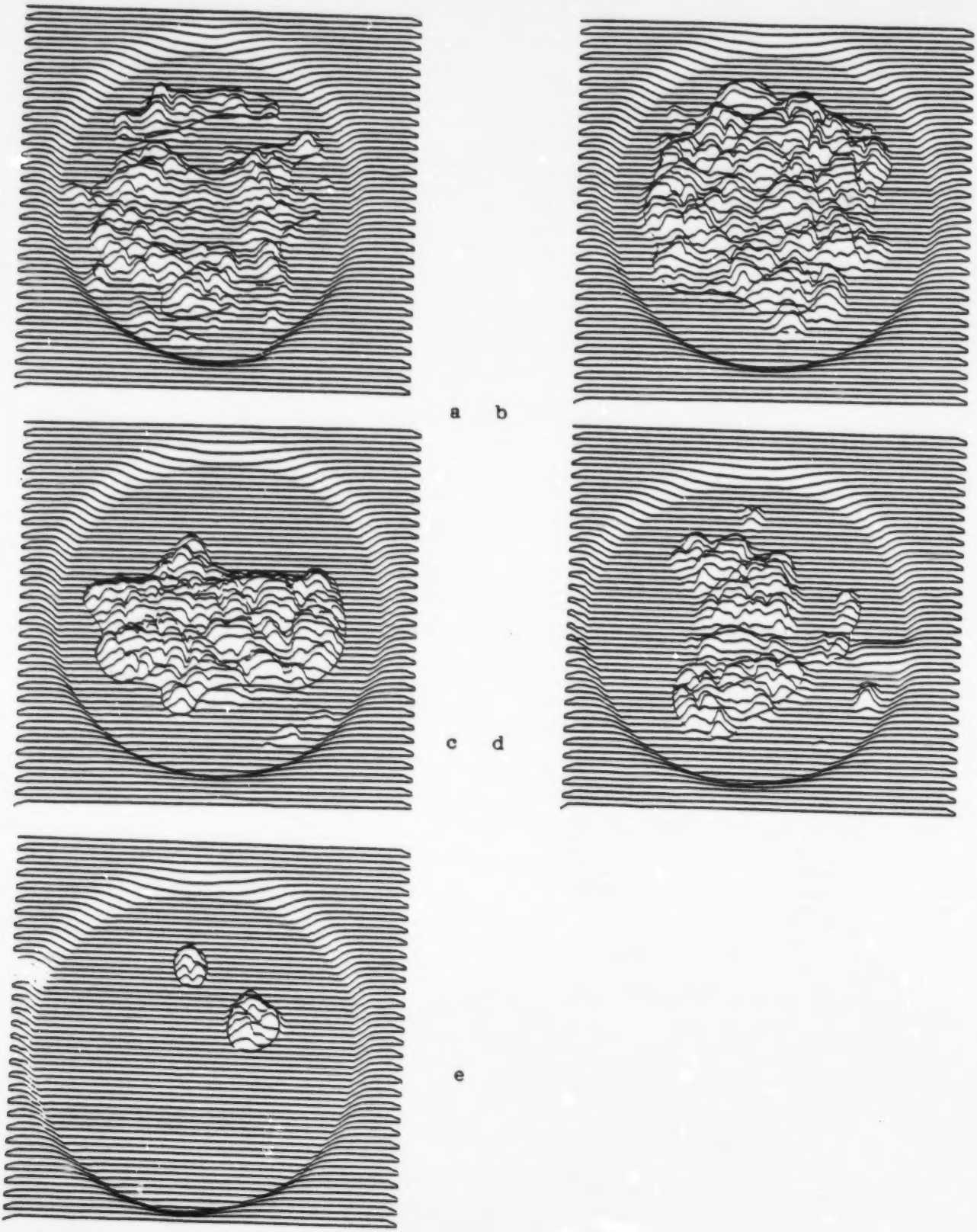

Figure C6. Pseudo-C-scan plots of autoclave samples (a) D1A1 (222°C/h), (b) D1A2 (111°C/h), (c) D1A6 (111°C/h), (d) D1A3 (56°C/h), and (e) D1A4 (28°C/h).

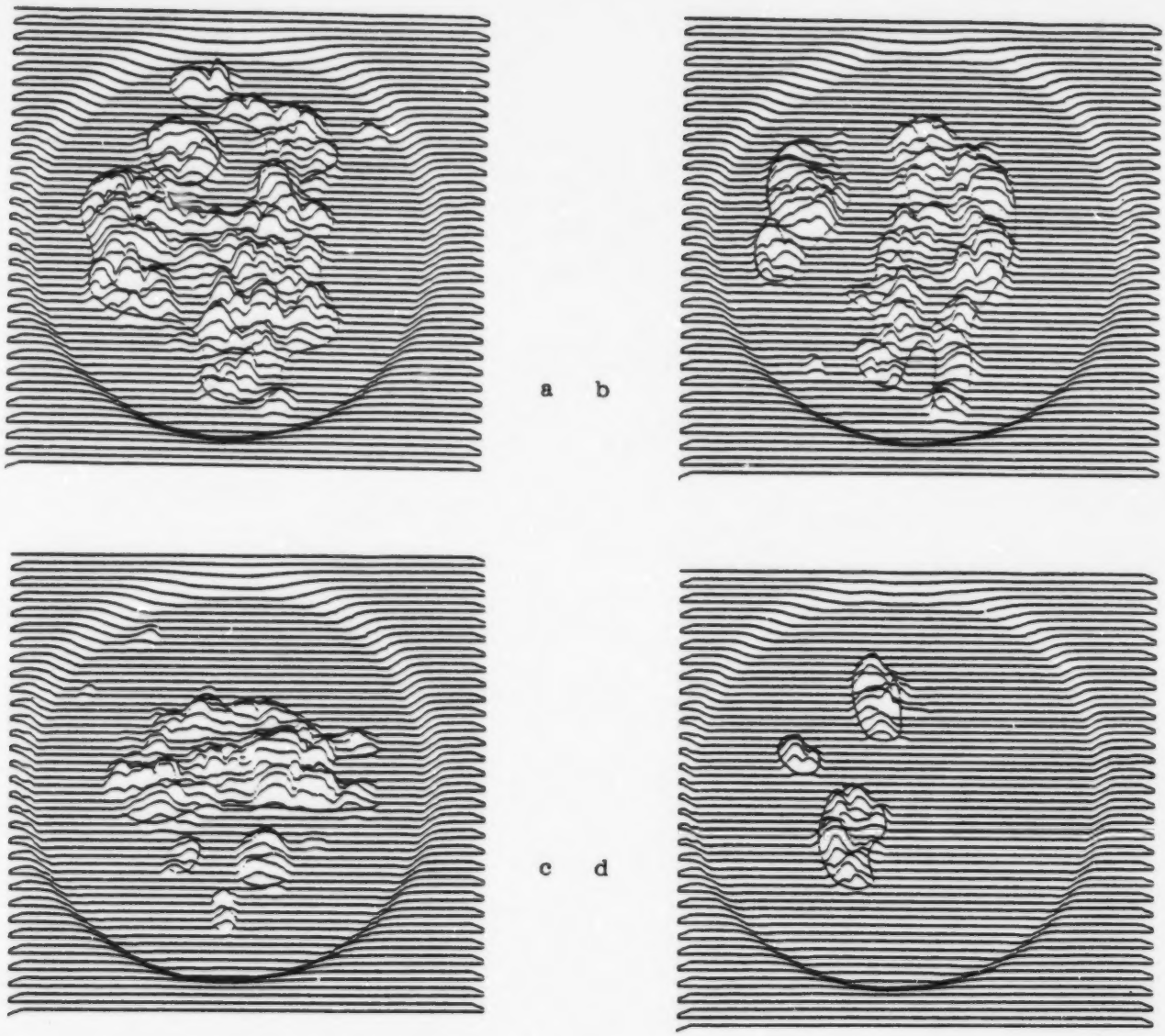

Figure C7. Pseudo-C-scan plot of autoclave samples (a) D2A2 (111°C/h), (b) D2A3 (56°C/h), (c) D2A5 (28/56°C/h), and (d) D2A4 (28°C/h).

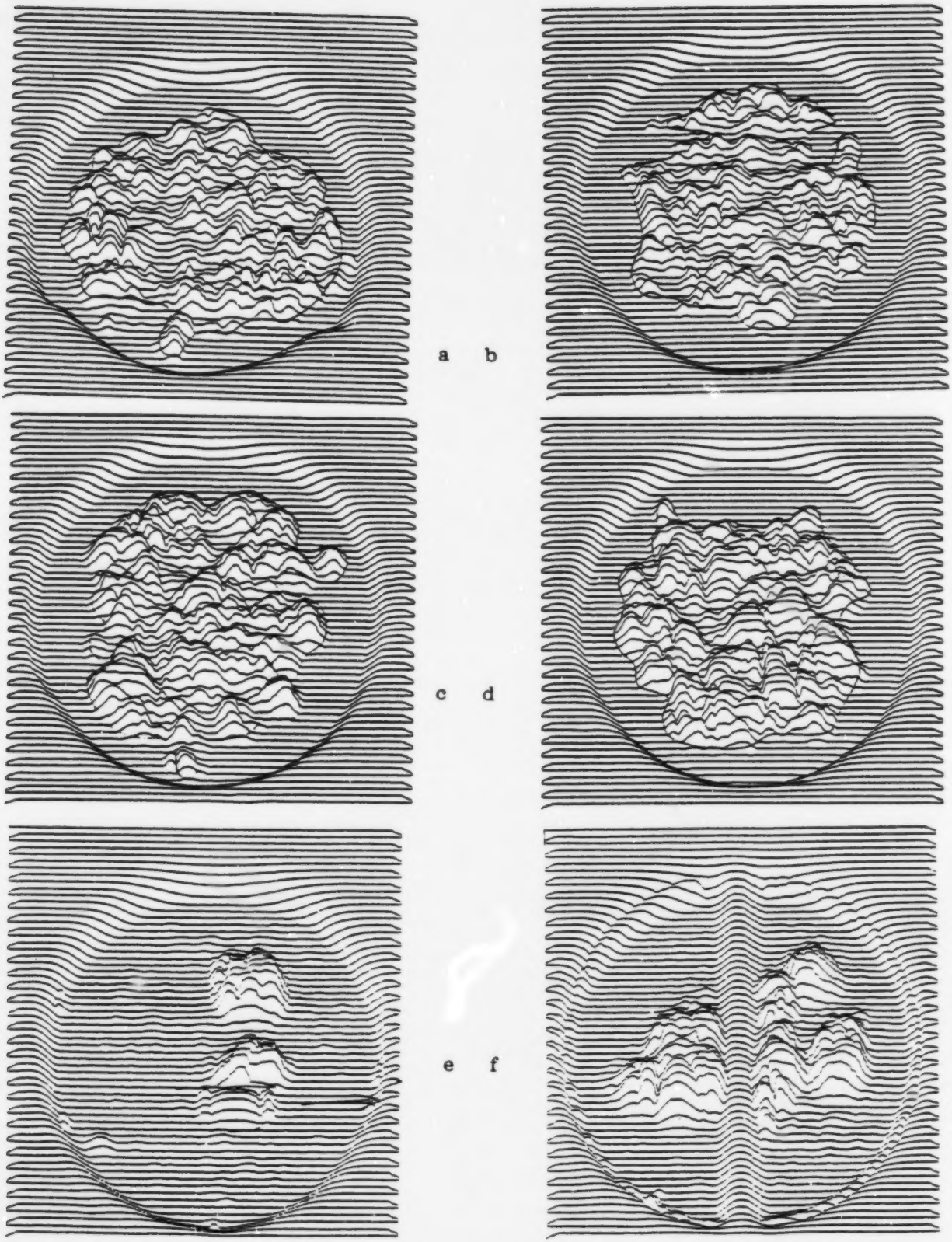

Figure C8. Pseudo-C-scan plots of autoclave samples (a) E1A1 (222°C/h), (b) E1A2 (111°C/h), (c) E1A5 (111°C/h), (d) E1A3 (56°C/h), (e) E1A4 (28°C/h), and (f) E1A6 (28°C/h).

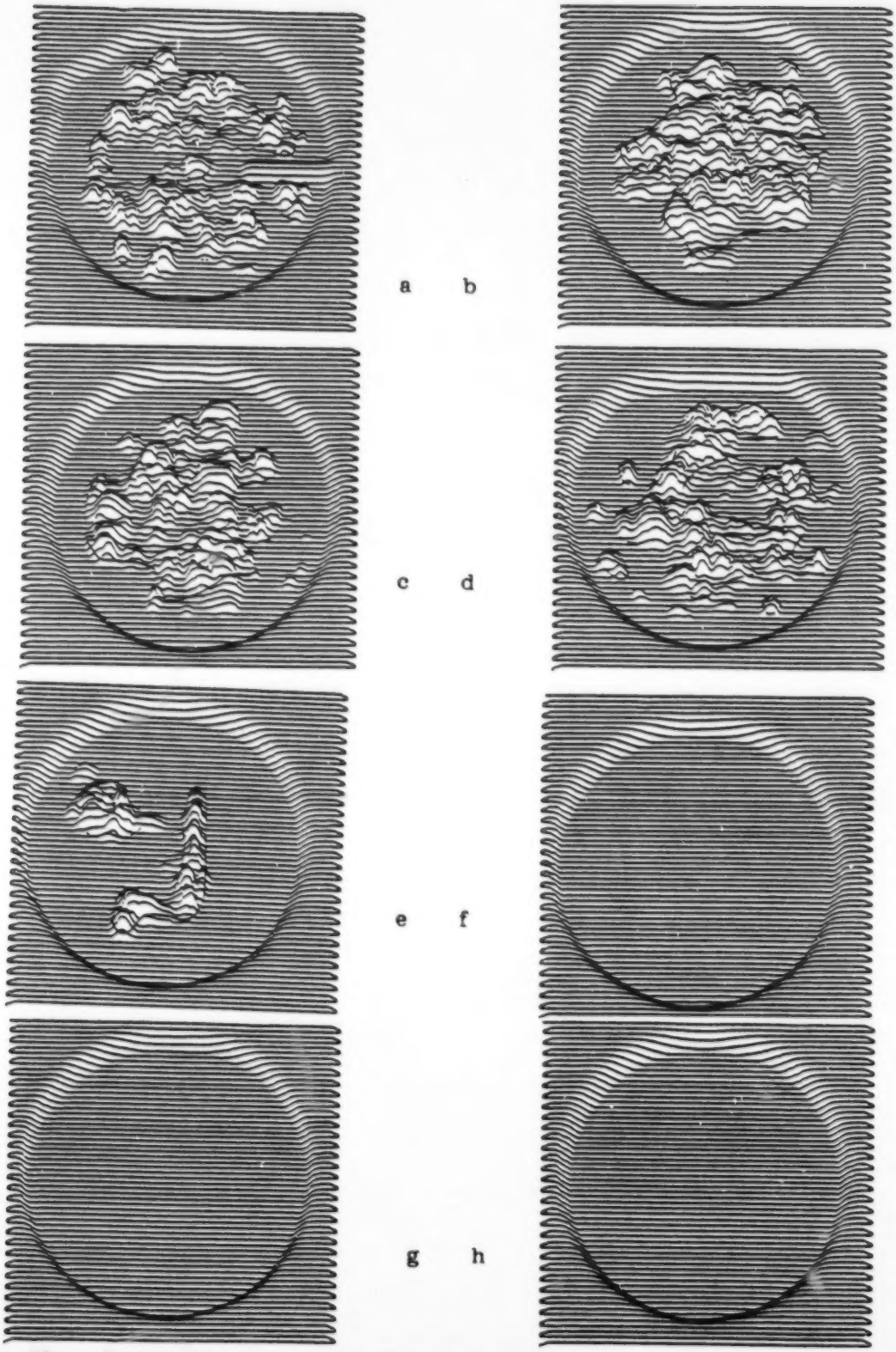

Figure C9. Pseudo-C-scan plots of autoclave samples (a) E2A1 (222°C/h), (b) E2A2 (111°C/h), (c) E2A3 (56°C/h), (d) E2A5 (56°C/h), (e) E2A4 (28°C/h), (f) E2A6N2 (222°C/h), (g) E2A7N2 (111°C/h), and (h) E2A8N2 (56°C/h).

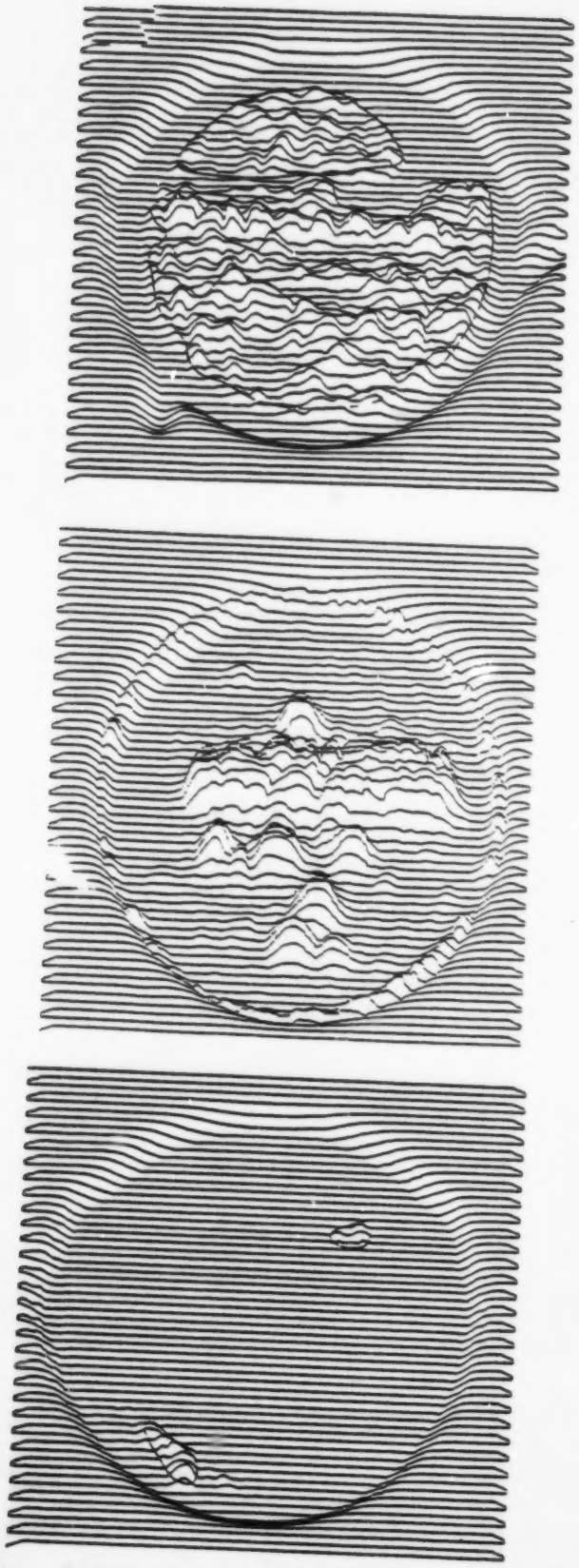

Figure C10. Psuedo-C-scan plots of autoclave samples (a) F1A1 (222°C/h), (b) F1A2 (111°C/h), and (c) F1A3 (56°C/h).